University of Miami
Scholarly Repository

2016-05-06

Novel Acoustic Wave Microsystems for Biophysical Studies of Cells

Sukru U. Senveli

University of Miami, usenveli@gmail.com

www.manaraa.com

UNIVERSITY OF MIAMI

NOVEL ACOUSTIC WAVE MICROSYSTEMS FOR
BIOPHYSICAL STUDIES OF CELLS

BY

Sukru Ufuk Senveli

A DISSERTATION

Submitted to the Faculty
of the University of Miami
in partial fulfillment of the requirements for
the degree of Doctor of Philosophy

Coral Gables, Florida

May 2016

المنارة للاستشارات

UNIVERSITY OF MIAMI

A dissertation submitted in partial fulfillment of
the requirements for the degree of
Doctor of Philosophy

NOVEL ACOUSTIC WAVE MICROSYSTEMS FOR
BIOPHYSICAL STUDIES OF CELLS

Sukru Ufuk Senveli

Approved:

_____   _____
Onur Tigli, D.Sc.   Sung Jin Kim, Ph.D.
Assistant Professor of   Assistant Professor of
Electrical and Computer Engineering Electrical and Computer Engineering

_____   _____
Michael R. Wang, Ph.D.   Mei-Ling Shyu, Ph.D.
Professor of   Professor of
Electrical and Computer Engineering Electrical and Computer Engineering

_____   _____
Tan A. Ince, M.D., Ph.D.   Ram H. Datar, Ph.D.
Associate Professor of Pathology   Associate Professor of Pathology

                                     _____
.   Guillermo Prado, Ph.D.
                                     Dean of the Graduate School

SENVELI, SUKRU UFUK   (Ph.D., Electrical and Computer Engineering)

<u>Novel Acoustic Wave Microsystems</u>   (May 2016)

<u>for Biophysical Studies of Cells</u>

Abstract of a dissertation at the University of Miami

Dissertation supervised by Dr. Onur Tigli
No. of pages in text: (155)

Single cell analysis is an important topic for understanding of diseases. In this understanding, biomechanics approach serves as an important tool as it relates and connects the mechanical properties of biological cells with diseases such as cancer. In this context, analysis methods based on ultrasonics are promising owing to their non-invasive nature and ease of use. However, there is a lack of miniature systems that provide accurate ultrasonic measurements on single cancer cells for diagnostic purposes.

The platform presented in this study exploits high frequency acoustic interaction and uses direct coupling of Rayleigh type SAWs with various samples placed inside microcavities to analyze their structural properties. The samples used are aqueous glycerin solutions and polystyrene microbeads for demonstrating proper system operation, and lead up to biological cells. The microcavity is instrumental in trapping a predetermined volume of sample inside and facilitating the interaction of the surface waves with the sample in question via a resonance condition. Ultimately, the resultant SAW reaching the output transducer incurs a phase delay due to its interaction with the sample in the microcavity. The system operates in a different manner compared to similar systems as a result of multiple wave reflections in the small volume and coupling back to the piezoelectric substrate.

The proposed microsystem was first analyzed using finite element methods. Liquid and solid media were modeled by considering frequency dependent characteristics. Similarly, mechanical behavior of cells with respect to different conditions is considered, and biological cells are modeled accordingly. Prototype devices were fabricated on quartz and lithium niobate in a cleanroom environment. Process steps were optimized separately for devices with microcavities. Precise fabrication, alignment, and bonding of PDMS microchannels were carried out. Soft microprobes were fabricated out of SU-8, a biocompatible polymer, for dispensing cells into microcavities. A high frequency PCB including a matching circuit was designed for the SAW devices. 3D printed housing was also prepared for demonstrating the integration capability.

Experimental results were collected first for analysis of high glycerin content in deionized water. Furthermore, polystyrene microbeads were counted with the system, and their sizes were differentiated experimentally to demonstrate the operation with solid media. Ultimately, biological cells were sensed and characterized. After tumor cells in media were transported to and trapped in microcavities, the proposed platform used SAW interaction between the substrate and the cells to extract their mechanical stiffness based on the ultrasound velocity. Measurements showed that output phase information is an indicator of the stiffness modulus of the trapped cells. Small populations of various types of cells such as MCF7, MDA-MB-231, SKBR3, and JJ012 were characterized and characteristic moduli were estimated for each cell population.

In conclusion, the results indicate that high frequency stiffness modulus is a possible biomarker for aggressiveness of the tumor and that microcavity coupled SAW devices are a good candidate for non-invasive interrogation and high frequency biophysical studies of single cells. The proposed system is a successfully miniaturized ultrasonic biosensor and can be integrated with microchannels to obtain higher throughput upon refinement of the design as evidenced by the initial results with microfluidics. Improvement in performance and signal strength is also shown to be possible through matching circuits as demonstrated.

It is with my deepest gratitude that I dedicate this dissertation to

my mother, Ozden,

my father, Safak,

and my sister, Zeynep.

None of this would have been possible without their love and support.

Acknowledgments

First and foremost, I would like to take this opportunity to thank my advisor Onur Tigli for guiding me through this arduous yet rewarding journey. Years of mentoring and support from him are what made this possible.

Ram Datar and Tan Ince have both had great impact on this study by sharing their vast knowledge on its biological aspects and through collaboration with our lab. It is imperative to extend my thanks to committee members, Sung Jin Kim, Michael Wang, and Mei-Ling Shyu for providing invaluable input that helped shape this study into its final state.

Randil Gajasinghe has shouldered a lot of responsibilities with me and helped out with cells, microfluidics, and experiments while we learned a great deal of these things together. I only wish he drank some coffee every now and then. I would like to thank Alperen Toprak with whom I spent a decade working together. I couldn't have asked for a better companion in my long adventure in academia. I cannot go without mentioning my friend and labmate Jorge Gomez for his help, support, and kindness. Our research team alumni Daniel Gonzalez, Andy Mok, and Marcos Feddersen are also acknowledged for helping me get started here in the lab.

My friends (and collaborators) Zheng Ao, Sid Rawal, and Anthony Williams have always been there to teach me about biological processes and give me great ideas. We could not have done tissue cultures by ourselves without the training of Michelle Williams. I would also like to acknowledge Giovanni Lenguito, Jorge

TABLE OF CONTENTS

LIST OF TABLES

LIST OF FIGURES

xiii

xiv

CHAPTER 1: INTRODUCTION AND MOTIVATION

Biomedicine has been a field of great interest in the scientific community. Among the goals of this field are fascinating feats such as early diagnosis and treatment of diseases and understanding the inner workings of various biological entities. The devices utilized for diagnostic purposes are called biosensors. Despite the great variety of proposed biosensors, a concise definition of biosensor can be given as: a platform consisting of a biological recognition system, a transducer, and a read out, which transforms certain information from a biological entity into an analytically useful signal. Although biosensors have predominantly been used for sensing biomolecules and similar entities, the definition can also be extended with analysis of biological cells which results is also closely related with lab-on-a-chip systems.

This chapter provides an introduction to the platform that was developed for tumor cell analysis as well the motivation behind it. A brief history of biosensors is given and tied to the use of ultrasonics. Surface waves and the importance of analysis of single cells are discussed. Finally, the definition and impact of the research contained in this dissertation is given along with the thesis organization.

1.1. Biosensors and Ultrasonics

Micro Electro Mechanical Systems (MEMS) made remarkable progress in the last two decades. This progress, followed and coincided by the advent of nanotechnology, has forced engineers and scientists from many disciplines to

collaborate on a diversity of interdisciplinary projects. One of the most promising fields that emerged is biosensors that employ these advanced technologies in the small scale. Major breakthroughs have been made in the field especially in the past decade. The associated devices, with some shown in Figure 1.1, range from nanowire field effect transistors (FETs) [1-3] to microcantilevers [4-7] and whispering gallery mode (WGM) optical sensors [1, 8], and from optical micro ring resonators (OMRRs) [9] to surface plasmon resonance (SPR) [8, 10, 11] type detectors and among others.

(a)   (b)
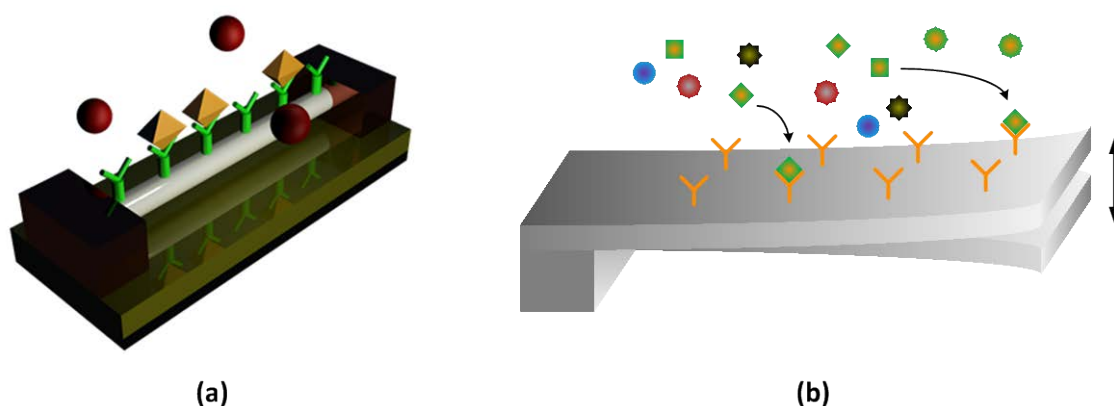
Figure 1.1. (a) Nanowire FET and (b) microcantilever type biosensors. The captured biomarkers are sensed as a result of the change in the electrical and mechanical properties of the respective biosensors.

Although the utilization of micro and nano scale technologies for biosensors is relatively new and still in progress, the history of the field of biosensors, in a general sense, spans half a century. Specifically, the amperometric enzyme electrode developed by Clark and Lyons in 1962 marks the initiation of the field. It operated as a glucose sensor and can be regarded the first ancestor of the modern biosensors [12]. It is widely accepted as a milestone on the way to all biosensing platforms that followed. Another important

breakthrough came about a decade later from Bergveld with the invention of ion sensitive FETs (ISFETs) for neurophysiological measurement purposes [13]. This innovation is considered to have paved the way for the modern nanowire FETs, as well as many chemical sensors and pH sensors. As a consequence of these developments, a big step was taken towards modern optical biosensing platforms with the application of surface plasmon resonance in a detector for the first time in 1983 by Liedberg, et al. [14]. From a physical standpoint, SPR was a well understood phenomenon at the time, yet its application to biosensing was a milestone for contemporary optical biosensors. On the other hand, mechanical biosensors, by and large, took after their MEMS counterparts which flourished with the growing popularity of MEMS in 1990s and 2000s.

Application of these methods to biomedicine and related fields is more recent but it has nonetheless spawned very interesting studies. These methods in the micron scale generally have the advantages of throughput, precision, cost efficiency, smaller overall system size, practicality, and small sample volumes. The small volume samples in question have usually been liquids due to their potential uses with microfluidics that have become ubiquitous in biomedical micro technology applications.

One important branch of modern biomedicine that proved its versatility many times over is ultrasonics used in a variety of fields. Ultrasound is the name given to sound pressure emitted at frequencies higher than the hearing capability of humans. Although they travel at the same speed as sound waves in a given medium, they have frequencies higher than 20 kHz which translate to

wavelengths smaller than regular sound waves. This brings about many possibilities due to their effective interaction with a variety of media.

Probably the most commonly recognized application of ultrasonics in healthcare is acoustic microscopy imaging. Also called ultrasonography (or even more briefly, ultrasound), this imaging technique uses periodically actuated piezoelectric crystals to propagate ultrasound pressure waves into human body and analyze the time of flight data to obtain an image of tissues and bones in a non-destructive manner [15].

A very specific type of ultrasound waves is the surface acoustic wave (SAW). A SAW is basically a high frequency (30-500 MHz) acoustic wave that travels along the free surface of an elastic substrate and decreases in intensity dramatically as the depth is increased with the most common type being Rayleigh waves [16]. The most common method to generate and sense SAWs is the use of piezoelectric materials as first demonstrated by White and Voltmer in 1965 [17]. Such SAW devices rely on reverse piezoelectric effect to convert electric charge to surface acoustic waves and direct piezoelectric effect to convert incoming waves to electric charge. Despite their utilization of acoustic waves, both the input and output are controlled electrically as shown in Figure 1.2(a). SAW devices are most commonly used as radio frequency (RF) and intermediate frequency (IF) bandpass filters in the industry with output characteristics similar to those shown in Figure 1.2(b).
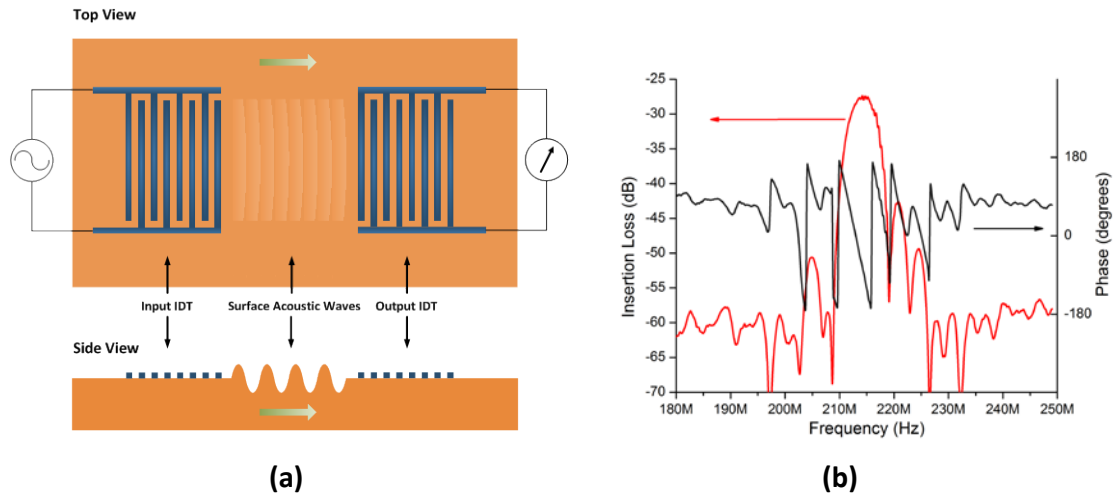
Figure 1.2. (a) The operation principle of a two port Rayleigh wave SAW device. (b) The bandpass filter characteristic behavior.

During fabrication, interdigitated transducers (IDTs) made of a certain metal (usually aluminum) are patterned on top of a specifically oriented face of a piezoelectric crystal substrate. Periodic electrical signals applied to the IDT structures are converted to mechanical deformations which propagate as waves on the substrate surface. Resonator-type SAW devices contain a single set of IDTs and are characterized by their return loss parameters. On the other hand, another widely used configuration consists of two sets of IDTs, in which one launches the SAW while the other one converts it back to an electrical signal. This configuration is usually called a delay line. A delay line is characterized by its transmission parameters, prominently by its insertion loss, as it behaves as a bandpass filter along a range of frequencies determined by the SAW properties as illustrated in Figure 1.2(b). Currently, acoustic wave based devices are the dominant technology in the market owing to their tiny form factor, excellent performance, easy integration with packaging, versatility, and robustness. Some

images from recent SAW research are shown in Figure 1.3. Today, commercial products that use acoustic wave filter technology range from cell phones, tablets, and TVs to RFID tags and radars [18].

(a)   **(b)**
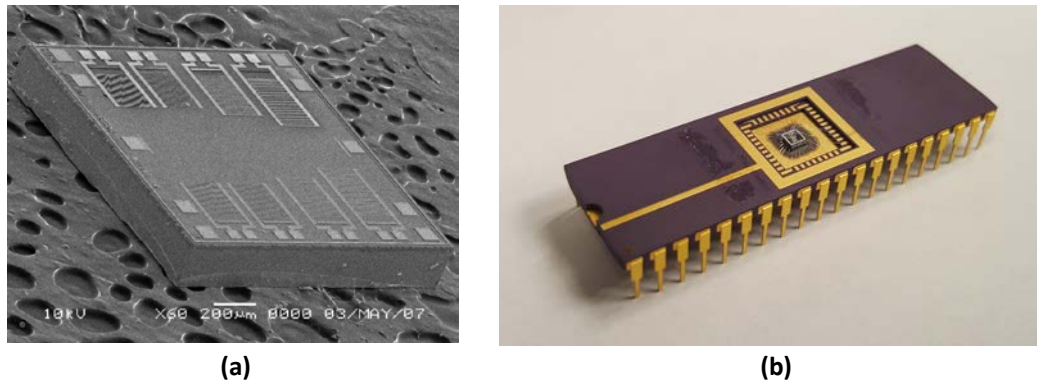
Figure 1.3. (a) A SAW biosensor chip fabricated with CMOS processes [19]. The figure is reprinted with permission. (b) The same SAW biosensor placed in and wire bonded to a 40-pin dual in-line package.

SAW properties are determined by the design as well as the type and specific surface (or cut) of the piezoelectric crystal being used. Waves that travel in the sagittal plane such as Rayleigh waves as well as horizontally polarized variants such as Love wave modes are possible [20, 21]. A common property of these waves is the concentration of energy close to the surface which renders them sensitive to perturbations on the surface. These disturbances are reflected to the output signal as shifts in different quantities. In biosensors or gas sensors, the sensitive surface is usually coated with a binding layer that immobilizes the analyte of interest to create these disturbances [22]. SAW technologies are evolving towards advancements in new sensing modalities, inclusion of non-piezoelectric substrates, and better integration with microfluidics to form complete systems [23-26].

SAW biosensors are known to be very sensitive and provide real time measurement capability with the right setup. A commonly used type of surface waves is Rayleigh waves that are a combination of longitudinal and shear waves with amplitudes decaying exponentially beneath the surface. These waves are vertically polarized and cause no displacement in the lateral direction. They are very sensitive to surface perturbations due to their high frequency resonance and polarization [27]. For the same reason, such SAW devices are very sensitive to presence of liquids. When the Rayleigh wave is traveling along the interface with a liquid, it releases compressional waves into the liquid due to its transverse component. This causes the surface wave to lose its energy drastically in a matter of a couple of wavelengths of propagation distance [28] as conceptually shown in Figure 1.4.
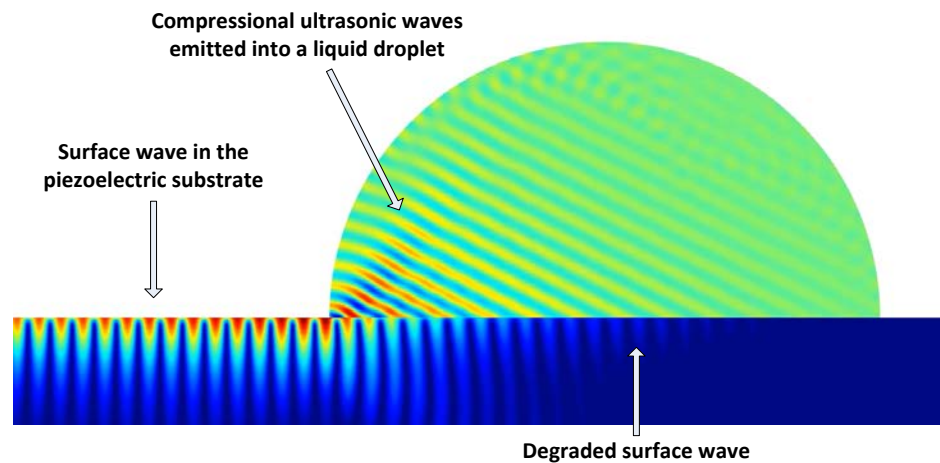
Figure 1.4. Representative cross sectional view of compressional wave emission into a large liquid droplet.

As a result of this efficient coupling, research trends moved in the direction where Rayleigh mode SAW sensors did not find much use for integration with

liquid environments for sensing purposes. Conversely, Lamb wave, Love and other SH-wave based devices have recently been used for liquid based measurements and specific measurements such as viscosity measurements [29-31]. Still, some attempts have been made in the past where large masses of liquids were used with bounce and waveguide modes for coupling with Rayleigh waves [32] but have not been followed through. On the other hand, there have been plenty of studies towards acoustic streaming of liquids with or without particles and acoustic processors [33] as opposed to sensors. Two things are common in most of these studies. Firstly, amounts of liquid being used are quite large, causing complete conversion of SAWs to acoustic compressional waves in liquid thereby eliminating the response due to SAWs on the receiving end. Secondly, such wave interactions have generally been considered as manipulation or actuation tools as opposed to sensing tools. However, there is great potential in analysis of small amounts of samples with biosensors.

1.2. Analysis of Single Cells

There has been increasing interest in the study of single cells as opposed to a population of cells. Traditionally, biological cell analysis has been carried out in large cell populations due to lack of tools and means to reach smaller dimensions. This caused researchers to interpret results mainly in terms of averages, and events occurring at cell level were not observable. Although cells of a given type behave in a similar way, cell populations are inherently heterogeneous and investigating a bulk of cells might even be misleading in some cases [34, 35] as shown in Figure 1.5. Such heterogeneities exist even for

homogeneously grown bacteria as shown in and differentiated from the changes that occur due to differences in cell cycles [36].

The case is very similar for eukaryotic cells as well, and single cell analysis is seen as the key to biological reductionism [37]. Cancer cells, which form the focus of this study, are known to be heterogeneous both in their pathology and molecular profiles [38]. Heterogeneities of various cancer cells are reported in many studies with respect to expression of a variety of surface markers and gene expressions [39, 40]. There have also been reports claiming that heterogeneity is correlated to cancer stem cell contents [41], clonal evolution model, or a combination of both [42]. The capability of analyzing single cells becomes extremely important for stem cells where the unlocking properties of even a single cell can mean a great deal. Such applications can pave the way especially for understanding the inner workings of cells [38, 43].
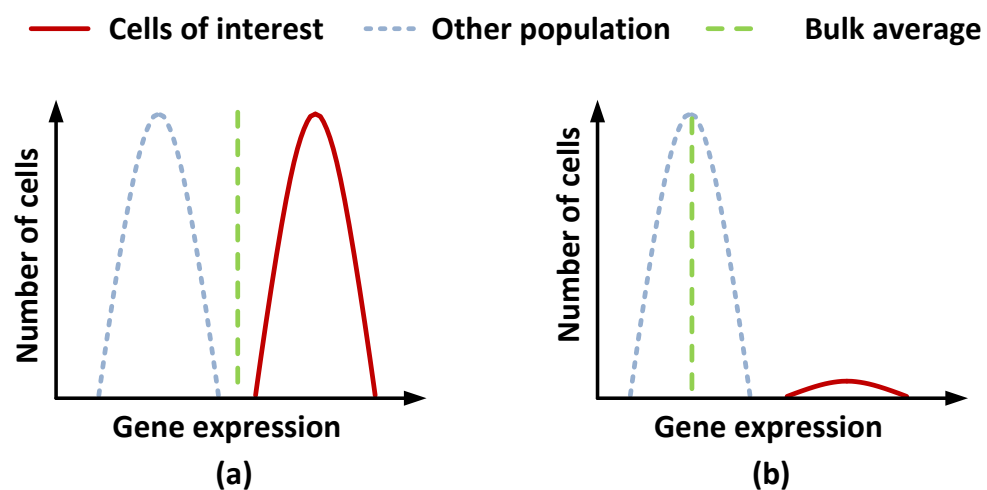
Figure 1.5. Two example cases where heterogeneities might mask individual cell properties based on an example of gene expression. The figure is adapted from [34].

Single cell analysis can be done in a variety of different domains. These are primarily, electrical, optical, and mechanical. A frontrunner among the analysis technologies is biomechanics approaches to study the mechanics of cells and their connections to diseases [44]. Recent pathophysiological studies of various diseases suggest that their etiologies might stem from changes in mechanical properties of cells. Most important examples with important correlations include malaria [45] and cancer [46]. The latter forms the focus of this study.

Cancer is the rapid proliferation of abnormal cells as shown in Figure 1.6. It starts with a single regular cell transforming to a tumor cell. These cells then spread to neighboring sites and metastasize in the body to destroy healthy tissue. Today, cancer is recognized as one of the leading causes of death in the world accounting for 8.2 million deaths in 2012 [47]. Early diagnosis of cancer usually gives the patient a higher chance of survival [48].
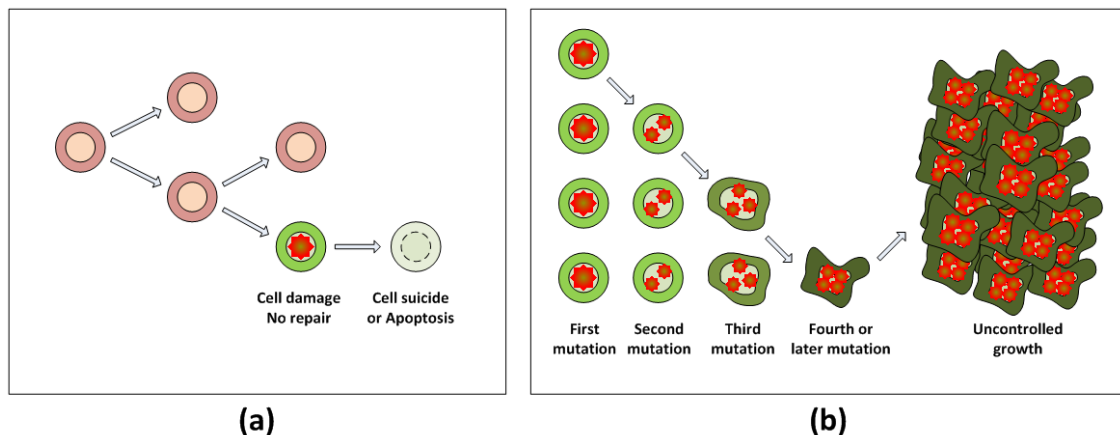
Figure 1.6. Loss of normal growth control in cells. (a) Normal cell division and (b) cancer cell division. The figure is adapted from [49].

Studies on cancer show that basis for cancer in general, is likely the changes in cell mechanics, tissue structure, or both [50], meaning that mechanical changes govern the growth of cancer. Mechanobiology research shows that epithelial and fibroblast cells decrease in deformability with cancerous growth [48]. Most studies yield 100% or more increase in deformation of cancerous cells for the same mechanical input and even more deformation for metastasized cells at low frequencies. The important implication that arises from many studies is that a good correlation exists between cancer and structural properties of the cell. Of course, the structural properties are heavily dependent on measurement method and the cell model being used. There are various ways of conducting mechanical measurements on cells to extract biophysical properties with some common methods illustrated in Figure 1.7(a-c).
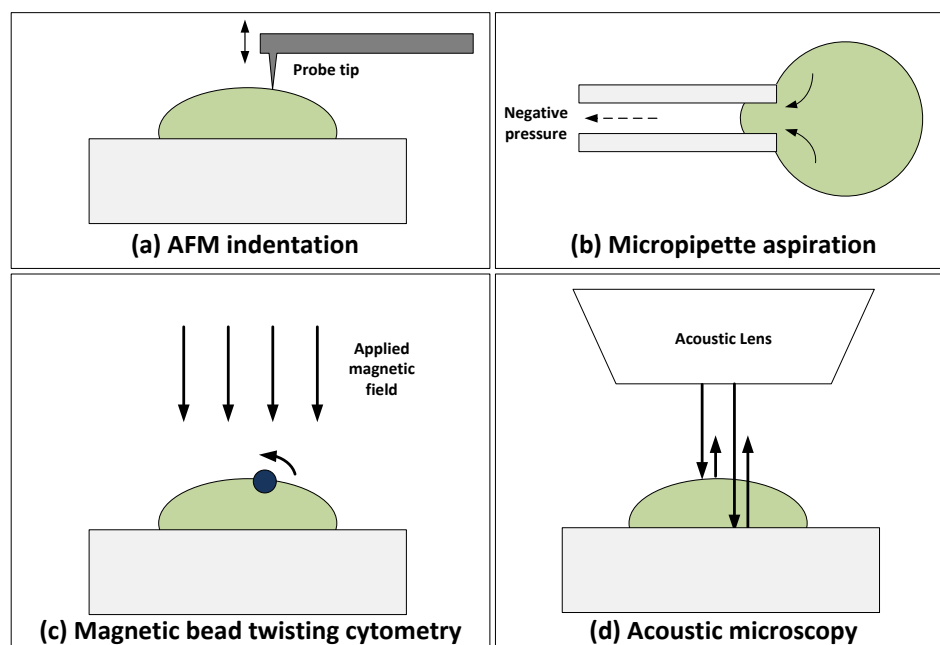
Figure 1.7. Popular mechanical experimentation methods on single cells: (a) AFM indentation, (b) micropipette aspiration, and (c) magnetic twisting cytometry. (d) An emerging analysis method, acoustic microscopy.

Some of the most widely used methods of mechanically analyzing cells are atomic force microscopy, micropipette aspiration, and magnetic bead twisting [51]. An atomic force microscope is a tabletop device where either a very fine tipped needle or a round blunt tip comes in contact with a sample, and the deflection of this needle is read out by a laser to obtain thickness and deformability of a sample under test [52]. Micropipette aspiration technique involves aspirating a relatively large part of the cell into a micropipette and observing the cell's recovery behavior [53, 54]. In magnetic bead twisting, beads that can be controlled with magnetic fields are placed on the cells and actuated, after which the resistance and recovery behavior of the cell is used to model it [55, 56]. Table 1.1 gives a list of mechanobiology results from the literature. Only AFM studies are cited in this table for coherence, due to the variety of different models and parameters used for representing mechanical behavior of cells.

Table 1.1. Results from literature obtained for AFM studies showing the difference in elasticities of healthy cells and tumor cells.

Study	Cancer Cell / Elasticity	Healthy Cell / Elasticity	Frequency
[57]	MCF7 / ~0.6 kPa	MCF10A / ~1.1 kPa	1 Hz
[58]	Hu-456 / ~0.4 kPa	Hu-609 / ~12.9 kPa	static
[59]	Non-small cell carcinoma of the lung from patient / ~0.52 kPa	Healthy counterpart / ~2.05 kPa	static
[60]	MMTV-PyMT (Mouse mammary) cells with cancer growth / ~0.45 kPa	Healthy counterpart / ~1.02 kPa	static
[61]	Pleural effusion cells from patient / 0.38 kPa	Healthy counterpart / 2.53 kPa	static

Ultrasound technology is another available tool for investigation of tumors that is not as common and goes underutilized. Ultrasound has been used to study the differences between cancerous and healthy tissues as far back as 1976 and 1986 where different attenuation levels were demonstrated and reported [62, 63]. More recently, acoustic microscopy has been targeting biological specimen at a single cell level.

In this method, single cells are placed under an acoustic microscope submerged in a coupling medium on a material with known propagation properties (such as a glass slide). The acoustic lens then focuses high frequency ultrasound onto the cell and onto the medium alone. The difference in the amplitude and delay of the reflected acoustic wave due to the cell is proportional to its properties [64]. Through comparison with the absence of the cell in the medium, cell properties are found relative to those of the medium [65]. This process is conceptually shown in Figure 1.7(d). Studies of MCF7 human breast cancer cells with high frequency acoustic microscopy were shown to be capable of distinguishing between apoptotic and un-apoptotic cells [66].

1.3. Research Definition and Impact

Important correlations between cancer and mechanical properties of cells have been well documented at both high and low frequencies. There currently exist many different methods for studying mechanobiology, and all widespread methods of biomechanical investigation discussed so far include systems for laboratory use as opposed to clinical use.

AFMs are usually quite expensive and require large spaces for operation. They take localized readings from adherent cells that can vary from location to location. The sharp probe tip directly pokes and dents the cells and therefore performs invasive analysis. It is also seemingly not possible to increase the throughput of an AFM through integration with other technologies or add further functionalities to it. Magnetic bead twisting, by very definition, is an invasive technique as it tags the cells with microbeads and renders them unusable for further studies. This method shears the cells in large amounts and while it gives direction dependent information about the cell deformability, its twisting nature is detrimental to cell structure in the long run. A similar argument is made for micropipette aspiration, where the large displacements put the cell under a great deal of stress which can compromise cell integrity. Some microfluidic studies loosely related to micropipette aspiration studies were adapted to work by stopping and stretching the cells [67]. Using advanced microfluidics, cell viscosity detection and enrichment was carried out in flow as well [68, 69].

The acoustic microscopy studies detailed in the previous section form a promising basis for non-invasive analysis of cells. Their high frequency nature is beneficial for this purpose whereas they can readily be integrated with microfluidics. It should be possible to excite similar acoustic waves in cell samples using versatile systems more suitable for miniaturization and microfluidic integration. These acoustic waves, through interaction with a cell sample, can help estimate high frequency mechanical properties of cells. Finally, these biophysical properties can be correlated to cell line in question with regards

to the type of tumor. This assertion forms the focus and motivation of this study. Consequently, a novel microsystem based on SAW device architecture is proposed as shown in Figure 1.9.
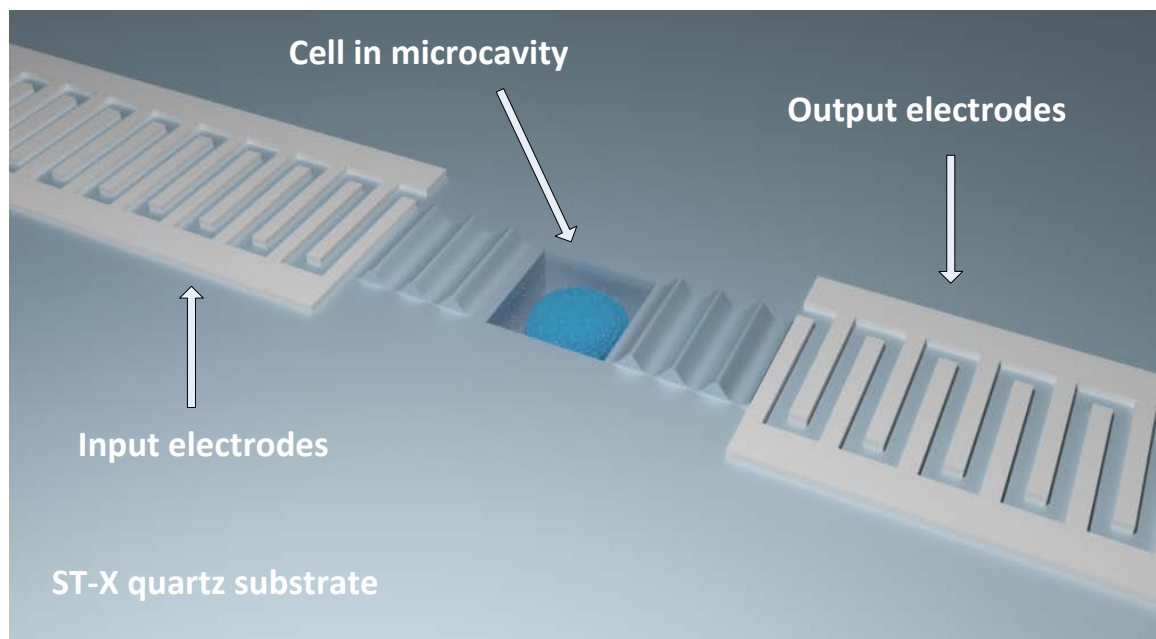
Figure 1.8. Conceptual image of the proposed system showing a cell trapped in a microcavity between two ports of the SAW sensor.

It is proposed that the use of piezoelectric-to-liquid coupling characteristics of Rayleigh waves can be used for interacting pico-liter volumes of samples. The structure discussed in this study is a two-IDT configuration with a microcavity of a certain depth etched in the middle of the delay line. This microcavity structure helps capture a minute amount of the sample of interest and facilitates direct interaction of the SAW with the sample. It also causes dispersion and loss of a portion of SAW to bulk waves depending on the geometry but the resultant output transfer characteristics are dependent on the way the surface wave interacts with the sample trapped in the microcavity.

The SAW device with embedded microcavity is a low cost system capable of analyzing samples at high frequencies similar to acoustic microscopy techniques. Furthermore, it can analyze sample volumes smaller than 10 pL which is orders of magnitude smaller than any other study reported to the best of the author's knowledge. Therefore the system is capable of analyzing single cells in ultra-small sample volumes. The approach outlined in this study differs from the previous studies outlined in the previous sections and uses SAW-liquid interactions as a sensing and differentiation mechanism for minute amounts of material. In the past, the only similar research on a similar topic with embedded microcavities has been a theoretical study about insertion of rectangular prism shaped polystyrene plugs into the delay line of SH-wave sensors with the purpose of not sensing but improving transmission characteristics and loading sensitivity [70]. *No other research exists on SAW interactions for interrogation of minute amounts of matter in a way similar to the presented approach to the best of the author's knowledge.*

SAW devices have been used for proteins and other biomarkers in the past but this is the first time that cells are analyzed within this context. At low power levels, the system is non-invasive and can be used to analyze samples. The system can be integrated with microfluidics to improve throughput. Furthermore, if applied to thin film piezoelectric devices, the concept can be integrated with readout electronics as well.

In order to quantify system behavior and verify the viability of the system, operation should be demonstrated with samples that are conceptually simpler

than biological cells. Therefore, the system is first demonstrated to operate with liquids, specifically with aqueous solutions of glycerin. This is an important milestone for validation. Afterwards, solid polystyrene microbeads are utilized to obtain its behavior with solids. Ultimately, operation with biological cells is demonstrated and conclusions are drawn.

1.4. Thesis Organization

Microcavity coupled SAW devices have been shown to be successful with measurements of all samples described above to varying degrees of success. As such, this dissertation is laid out to describe and illustrate the steps of this dissertation study as given below.

Chapter 2 discusses the technical background for piezoelectricity and all types of waves relevant to the study: waves in liquids and solids including surface waves. Coupling of these waves to one another is discussed and the effect of operation frequency is explained. Modeling of biological cells is outlined and the most viable option for modeling them is presented considering the experimental conditions. Also a system model is presented. Unfortunately, unless the system is over-simplified, it is very difficult to obtain a simple analytical expression for system behavior. Therefore, finite element modeling is required.

Chapter 3 details the efforts in analysis of the system, particularly the finite element studies. The physical phenomena and waves explained in Chapter 2 are validated. Microcavity resonance is explained and system operation with liquids,

solids, and cells is detailed with simulation results. Matching circuits and selection of devices are also discussed.

Chapter 4 elaborates on microfabrication of the SAW devices, sensing microcavities, microchannels, and dispensation tools. It includes metrology study results as well as optical and scanning electron microscope images of successfully fabricated devices.

Chapter 5 presents the experimental results as well as the conditions and equipment used. Major challenges that were faced and overcome during dispensation of such small amounts of samples are demonstrated. Validation of SAW device operation, sensing of glycerin concentration as well as microbeads are discussed. Comprehensive results from different cancer cell lines are presented. Finally, initial measurements from devices with microchannel integration and with PCB integration are given.

Chapter 6 discusses the results obtained from the work contained in this dissertation, compares them to other studies, and draws conclusions. This chapter also lays out the future work envisioned for continued development of the outlined platform.

CHAPTER 2: THEORETICAL BACKGROUND

There are various different ways of modeling SAW device operation with varying degrees of accuracy. Delta function model is the simplest and possibly the crudest form of modeling [18]. Coupling of modes and 3-port models are others with higher accuracy for modeling the behavior SAW delay lines usually used as electronic filters [18, 71]. For even higher accuracy, finite element analysis (FEA) is the most viable and versatile tool for SAW devices.

The proposed system operates based on the back and forth coupling between surface waves and waves inside a sample. Basically, surface waves generated in the piezoelectric substrate interact with the sample to generate waves which in turn couple back to the substrate; however, this coupling is hard to model analytically. An understanding of the mechanics and the equations behind these other domains and how they interact together must be established to express the system correctly in FEA. For this reason, this chapter discusses waves in liquid and solid media and their behavior given the conditions.

Firstly, elementary waves are discussed in simple liquids and solids as these waves will be traveling inside the observed sample in the microcavity. Waves in simple liquids and solids are the gateway to understanding the wave behavior in materials much harder to model, such as cells. Then, piezoelectricity and surface waves are explained to provide a better picture of the system. Finally, various models of biological cells are presented along with the expected behavior at high frequencies.

19

2.1. Waves in Liquids and Solids

Waves are usually classified as either transverse or longitudinal waves as shown in Figure 2.1. Analogous to electromagnetic waves, transverse (or shear) waves have variations that are perpendicular to the direction of propagation. Consequently, they can exist in different polarizations in a single propagation direction. Longitudinal (or compressional) waves are analogous to sound waves (which are pressure waves) and have displacements along the direction of propagation. Longitudinal waves are not associated with polarizations as displacement is always in the direction of propagation. Other types can usually be expressed as a combination of these basic types of waves.

Transverse (Shear) Wave Propagation

Longitudinal (Compressional) Wave Propagation
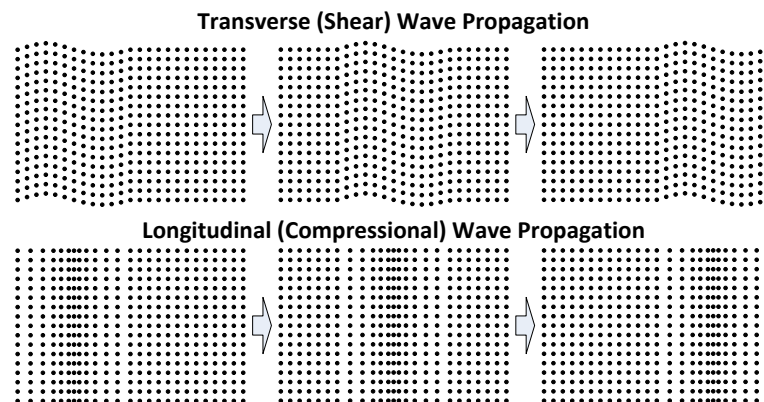
Figure 2.1. Transverse and longitudinal waves.

The velocity field for describing wave motion follows directly from Newton's 2nd law of motion and is given by Cauchy's equation

$$\rho \frac{\partial v}{\partial t} + \rho(v \cdot \nabla)v = f \tag{1}$$

where ρ is the density, v is the velocity field, and f is the contribution of external forces. This equation, along with the conversation of mass defines the behavior

of flow in all media, solid, liquid, and gaseous [72]. What makes the difference between these materials is the force density term on the right side. In general terms, force density is given as

$$f = g + f_{in} = g + \nabla \cdot \sigma_{ij} \qquad (2)$$

where g denotes the gravity and other external forces and f_{in} stands for the internal forces of the medium, and σ is the second rank stress tensor with elements σ_{ij}. It is the different qualities of the second part on the right hand side in solids and liquids that causes them to behave differently.

Barring special cases, liquids are homogeneous and experience stress that is equal in all directions. Liquids do not bear shear stresses under regular conditions; however, friction exists in liquids even in steady flows and the most ideal of liquids. These frictions are quantified as viscosity (sometimes called shear viscosity or dynamic viscosity) and can be visualized as opposing shear forces applied to the layers of liquid passing by at different velocities as shown in Figure 2.2. These stresses applying to unit infinitesimal areas are given by

$$\sigma_{ij} = \eta \frac{\partial v_i}{\partial x_j} \qquad (3)$$

where η acts as a constant of proportionality and denotes viscosity. It is important to note that this is a shearing effect although it has repercussions on longitudinal effects as well. If a fluid is compressible, then

$$\nabla \cdot v \neq 0 \qquad (4)$$

since the velocity field changes in the vicinity of the observed point [73].
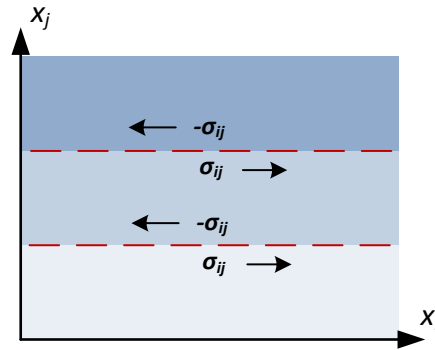
Figure 2.2. Effect of viscosity during flow. The darker colors higher flow velocities. Viscosity results in stress between adjacent layers of fluid at different velocities.

A Newtonian fluid is a type of fluid where this viscosity is independent of the shear rate or frequency. That is, the frequency or interaction rate with the fluid does not change its viscosity. Most simple liquids including water and glycerin which are to be used later in the finite element analysis and experimental sections are Newtonian fluids under the right conditions.

For compressible liquids, a component can be added to the stress tensor, along the diagonal to represent the direction of the stress, η_B, as a term accounting for a "longitudinal" viscosity effect, usually named bulk viscosity, second viscosity or volume viscosity. Considering the effects from both viscosity and bulk viscosity, and plugging into Cauchy's equation

$$\rho\frac{\partial v}{\partial t} + \rho(v \cdot \nabla)v = g - \nabla p + \eta\nabla^2 v + (\eta_B + \frac{\eta}{3})\nabla(\nabla \cdot v) \tag{5}$$

which can be considered the most general form of the Navier-Stokes equations describing the continuum behavior of a fluid [73].

The advective term, $\rho(v \cdot \nabla)v$, on the left hand side defines spatially governed changes in the velocity field of the fluid flow such as the decreasing flow rate of a fluid when the flow in a pipe proceeds to a larger diameter pipe. The geometry of the microcavity in this study as shown in Figure 1.9 is quite small with simplistic shapes and should not affect the liquid in this way. Assuming a simple liquid and assuming harmonic time dependence, the ratio of the advective term to local acceleration term in (5) is given approximately by

$$\left| \frac{(v \cdot \nabla)v}{\frac{\partial v}{\partial t}} \right| \approx \frac{\omega \, d}{v_0} \tag{6}$$

where d is the total displacement causing the velocity change [73]. In the case of the coupling of displacement in the piezoelectric domain (10^{-12}m) at frequencies around hundreds of MHz to the sample in the microcavity, the ratio comes out to be in the order of $0.01/1500 \ll 1$, so the advective term can be readily omitted to obtain the wave equation. Furthermore, in the small amplitude model that is used, the expansion for velocity field, v, is selected as $v = v_0 + \delta v = 0 + \delta v$ to imply that there is no general mass flow observed apart from the small variations.

Combining the complete form of Navier-Stokes equation in (5) along with the continuity equation, a wave equation

$$\frac{\partial^2 \delta \rho}{\partial t^2} = v_0^2 \nabla^2 \delta \rho + \frac{\eta_B + \frac{4}{3}\eta}{\rho_0} \nabla^2 \frac{\partial \delta \rho}{\partial t} \tag{7}$$

is obtained where the second term on the right hand side causes attenuation due to viscosities. Now a time harmonic solution is assumed with along with an attenuation term, α, such as:

$$\delta\rho = \rho_A \exp(-\alpha x)\exp[j(kx - \omega t)] \tag{8}$$

and:

$$\alpha = \frac{\omega^2}{2\,\rho_0 v_0^3}(\eta_B + \frac{4}{3}\eta) \tag{9}$$

Therefore it can be seen that the attenuation of the wave in a liquid is governed by shear viscosity as well as the bulk viscosity [74]. Another important point here is that the attenuation is strongly related to the operation frequency. This is the principal mechanism for attenuation of ultrasound at high frequencies. At lower frequencies, other factors such as dust or environmental conditions might be effective whereas at ultra-high frequencies nearing the molecular relaxation time of a liquid (for instance, 1 THz for water), different atomic level effects come into play. For harmonic solutions of (7), the loss factor arising from viscosities in (8) can be integrated directly into the velocity and density parameters so that a modified velocity parameter, v_m, and modified density, ρ_m, would read

$$v_m = v_0\sqrt{1 + j\omega\frac{(\eta_B + \frac{4}{3}\eta)}{\rho_0\,v_0^2}} \tag{10}$$

$$\rho_m = \frac{\rho_0}{1 + j\omega \dfrac{(\eta_B + \dfrac{4}{3}\eta)}{\rho_0 \, v_0^2}} \tag{11}$$

in frequency domain. This is the most direct way to solve for losses in frequency domain by harmonic analysis suitable for finite element solutions [75]. This equation has been used by substitution into (7) and converting to pressure and density variables by linearization in the FEA simulations provided in the next chapter.

As stated before, solid matter behaves pretty much the same way according to equation (1) but with two major differences against liquids. Firstly, the advection term on the left hand side disappears for all solids. Secondly, solids can support shear stresses as part of their stiffness matrix. For a solid isotropic material, the stress tensor elements can be expressed in two tensors corresponding to shear and diagonal elements associated with the two Lamé parameters, μ and λ. For solids, Navier's equation of motion as

$$\rho_0 \frac{\partial^2 u}{\partial t^2} = \mu \, \nabla^2 u + (\mu + \lambda)\nabla\nabla \cdot u \tag{12}$$

which resembles that of the liquids and defines the displacement vectors inside a solid [76]. The solutions for u can be broken down into two different types of waves. This is where the solids differ from liquids as the wave equation of the form given by

$$\frac{\partial^2 u}{\partial t^2} = v_0^2 \, \nabla^2 u \tag{13}$$

which has two main distinctive solutions depending on v. For longitudinal waves,

$$\nabla \times u_L = 0 \quad and \quad v_{0,L} = \sqrt{\frac{2\mu + \lambda}{\rho_0}} \qquad (14)$$

whereas for transverse waves,

$$\nabla \cdot u_T = 0 \quad and \quad v_{0,T} = \sqrt{\frac{\mu}{\rho_0}} \qquad (15)$$

Both Lamé parameters are always positive. As a result of this, the velocity of the longitudinal wave is always larger than transverse waves in any given solid [76]. Other waves also exist in solids such as Rayleigh waves, Love waves, Lamb waves, or surface skimming bulk waves (SSBW). These waves occur under specific conditions but they can be expressed mathematically and intuitively using properties of these two main types of waves. The specific type of surface waves used in this study, Rayleigh waves, will be summarized in the next section.

2.2. Piezoelectricity and Rayleigh Waves

Piezoelectric effect is the electromechanical interaction that causes some crystals to accumulate electrical charge in response to mechanical deformation. Inverse piezoelectric effect is defined as deformation in response to electrical charge. Hooke's law and the equation for capacitance are then modified by a piezoelectric coefficient tensor as

$$[\sigma] = [c][S] - [e^t]E \qquad (16)$$

$$D = [e][S] + [\varepsilon]E$$

where σ is the stress, c is elasticity or Young's Modulus, S is the strain, E is the electric field, D is the charge density, ε is the dielectric permittivity, and the added terms e and e^t denote the piezoelectricity coefficient tensor and its transpose, respectively [18]. Piezoelectric crystals are anisotropic solid crystals, and this anisotropy causes bulk and surface waves to be specific to certain surfaces and directions of the crystal.

Rayleigh wave is a special type of wave that was first discovered by and named after Lord Rayleigh in 1878. These waves can only be excited on the traction free surface of an elastic solid, i.e. $\sigma_{13} = \sigma_{23} = \sigma_{33} = 0$. Mathematically, Rayleigh waves can be shown to be the sum of the distinct longitudinal and shear components near the surface of the solid combined with the fact that they decay in amplitude in the direction into the substrate. The long version of the derivation is not given here but the most general harmonic solution of the Rayleigh wave in an isotropic medium is given as [77]:

$$u_L = A\,(B\exp(-\alpha kz))\exp[j(kx - \omega t)]$$

$$u_T = A\,(C\exp(-\beta kz))\exp[j\left(kx - \omega t + \frac{\pi}{2}\right)] \tag{17}$$

One of the most important implications of this result is that the two components of the Rayleigh wave are out of phase by 90º and thus contribute to an elliptical motion of each point around its steady state position. It should be noted that the velocity of the wave indirectly present in the above equation, v_R, is always less than that of the bulk waves, both longitudinal and transverse [18]. The complete expression for obtaining the Rayleigh wave velocity is as follows [76]:

$$\left(\frac{v_R}{v_T}\right)^6 - 8\left(\frac{v_R}{v_T}\right)^4 + 8\left(\frac{v_R}{v_T}\right)^2\left\{3 - 2\left(\frac{v_R}{v_L}\right)^2\right\} - 16\left\{1 - \left(\frac{v_R}{v_L}\right)^2\right\} = 0 \qquad (18)$$

Rayleigh wave solution for an anisotropic solid is also similar. The true Rayleigh wave motion reverses at a depth of about 0.2λ whereas displacement due to Rayleigh waves in the -z coordinate decays with $\exp(-z/\lambda)$. Majority of the wave energy is constrained to a depth of λ from the surface. Rayleigh wave amplitude generally decreases with $r^{-1/2}$ for practical applications.

Rayleigh waves at the micron scale are usually excited on piezoelectric substrates. The derivation of the exact form of Rayleigh waves for anisotropic follows from the fact that the stress tensor σ is not symmetric. This prohibits the simplification of the expression (2) and makes the solution more complicated. This condition limits the existence of Rayleigh waves only to some specific orientations for a given anisotropic crystal. For this reason, only specific and precisely cut surfaces of piezoelectric crystals can be used for the excitation of a specific type of surface wave. An important factor is the electromechanical coupling coefficient which defines the amount of electrical energy being converted into mechanical energy. While this coefficient is a function of piezoelectric properties it is also experimentally shown that it is dependent on the change of wave velocities between regular and short circuited surfaces as

$$K^2 = \frac{e^2}{c\varepsilon} \approx -2\frac{\Delta v_R}{v_R} = 2\frac{v_{free} - v_{metallized}}{v_R} \qquad (19)$$

where e is the piezoelectric constant, c is the modulus of elasticity, ε is the relative dielectric constant, and Δv_R represents the Rayleigh wave velocity

change that occurs when the piezoelectric material surface is short circuited with a very thin metal layer so that the electric field component along the direction of propagation vanishes. This expression is good for approximations up to 10% error [71]. Table 2.1 shows the Rayleigh wave related properties of the crystals considered in this study, quartz and lithium niobate. Due to magnitudes of their coupling coefficients, quartz is inherently a good substrate for narrow-band filter applications whereas lithium niobate is inherently better for wide-band applications.

Table 2.1 Rayleigh wave properties on quartz and lithium niobate.

Substrate / Cut / Axis	Density (kg/m3)	v_R (m/s)	K^2 (%)	Temperature delay coefficient (ppm/K)
Quartz / ST / X	2651	3158	0.11	~0
LiNbO$_3$ / Y / Z	4700	3488	4.5	4.6

2.3. Coupling of Waves Between Media and Mode Conversion

An important parameter when defining wave propagation in materials is the acoustic impedance. Usually pertaining to longitudinal waves but usable for all waves in theory, acoustic impedance, Z, for a specific frequency is given by

$$Z = \frac{p}{vA} \tag{20}$$

where is the surface area and it varies with geometry. On the contrary, characteristic acoustic impedance is a property of a medium, analogous to characteristic impedance used in transmission lines in electromagnetics,

$$Z_0 = \rho_0 v_0 \qquad\qquad (21)$$

where the subscripts denote the rest state. As a result, Z_0 does not vary for a given material [74].

Two defining characteristic of all waves are refraction and reflection as waves travel from one medium to another. While the angle of reflection always stays the same for specular reflections, the angle of refraction is given by the ratio of the speed of the waves in respective media according to Snell's Law. During investigation of the transmission of waves from one medium to another, Snell's Law needs to be expanded to include different types of waves [15, 73, 78]. That is because of the phenomenon known as mode conversion where waves transmitted to solids can take the form of shear and/or longitudinal waves. Consequently, the angle of refraction is simply given by Snell's law as

$$\frac{\sin \theta_u}{v_u} = \frac{\sin \theta_L}{v_L} = \frac{\sin \theta_T}{v_T} = \frac{\sin \theta_R}{v_R} \qquad\qquad (22)$$

where the subscripts u, L, T, and R denote ultrasound (the wave in liquid), longitudinal, transverse, and Rayleigh, respectively. Normally v_L and v_T are the wave velocities as found from (14) and (15) for isotropic solid media. Since the main interest in this study is transmission from liquid to solid (and vice versa), the two media as shown in Figure 2.3 can be considered to illustrate the expanded version of Snell's Law which takes into account the mode conversion of the waves as they propagate from one medium to another.
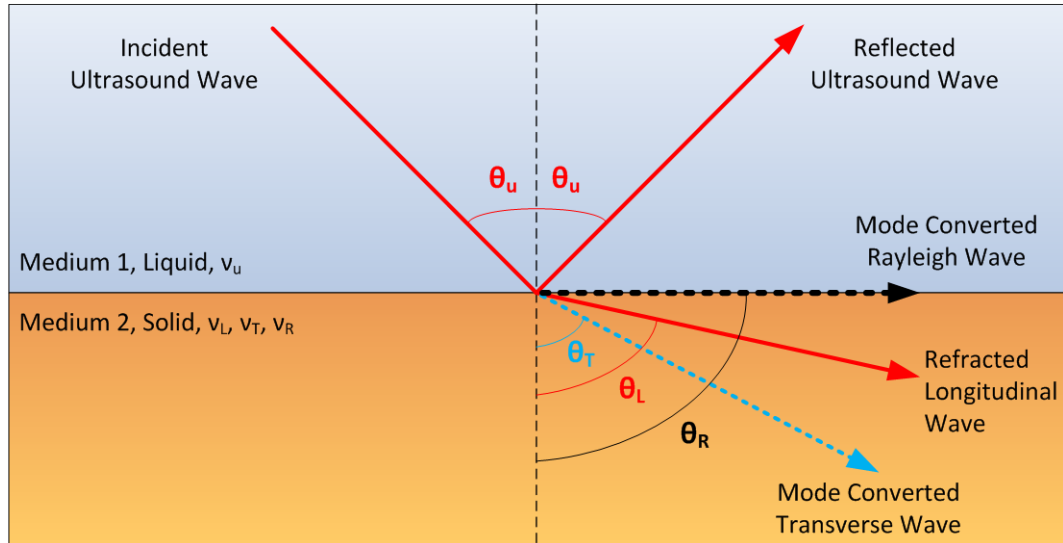
Figure 2.3. Refraction of waves according to Snell's law.

Based on the magnitude of θ_u the wave transmitted to the other medium can be a longitudinal wave, a transverse wave, or a combination of these, a Rayleigh wave. As θ_u is increased, the angle of the transmitted longitudinal wave, θ_L, will increase accordingly. After the first critical angle where $\theta_u = \theta_{C1} = arc\sin(v_u/v_L)$, the longitudinal wave will disappear but since the velocity of the shear wave is smaller, there will still be a mode converted shear wave. The incident longitudinal wave starts propagating as a longitudinal surface wave. As θ_u is further increased beyond the second critical angle, $\theta_u = \theta_{C2} = arc\sin(v_u/v_T)$, the only transmitted type of wave will be the surface wave: the Rayleigh wave. This is because the shear wave is also propagating on the surface now. Following from the figure and properties of Rayleigh waves, θ_R always has to be 90°. The converse of the case where the surface waves generate longitudinal waves in liquids works the same way as in Figure 2.3 but from medium 2 to medium 1. The transverse component generates

compressional waves at the angle, θ_u [26]. In ST-X quartz, the longitudinal wave velocity is 6140 m/s and Rayleigh wave speed is 3158 m/s. There are two transverse waves with horizontal and vertical polarities, the velocities of which are given by 5050 m/s and 3840 m/s [79, 80].

As mentioned before in the section reviewing Rayleigh waves, an interesting fact is that the Rayleigh wave velocity is smaller than transverse and shear waves for any solid material, such as quartz. Most liquids such as water, glycerin, acetone, alcohols, and oils have ultrasound velocities between roughly 1000-2000 m/s at room temperature. More specifically, the liquids that are utilized in this study, i.e., glycerin and water mixtures, as well as cellular medium have ultrasound velocities between roughly 1500-1800 m/s. As a result, the angles associated with ultrasound emitted into the liquid sample range between $\theta_u = 28° - 37°$. For a velocity of 1500 m/s, $\theta_u = 28°$, and the critical angles are given as $\theta_{C1} = 14°$, and $\theta_{C2} = 23°$. Similarly for every given velocity, the angle between the surface normal and the generated ultrasound, θ_u, will be larger than both θ_{C1} and θ_{C2}. When ultrasound in the microcavity gets reflected, from either the bottom of the microcavity or the boundary with air, its incidence angle will again be $90° - \theta_u° > \theta_{C2} > \theta_{C1}$. This holds in all cases considered here as $v_u < v_R < v_T < v_L$ for all samples. The direct consequence of this result is that all waves that couple back to the substrate are going to be Rayleigh waves.

Liquids in contact with solid surfaces have boundary conditions that impose some limitations on them. For viscous liquids, a no slip boundary condition exists barring for very hydrophobic surfaces as shown in [81]. The

liquid velocity field along the boundary must be zero with respect to the displacement of the solid such that

$$v_{liquid} \times \hat{n} = v_{solid} \times \hat{n} \qquad (23)$$

where $\hat{n}$ is the surface normal of the boundary. This is called the no slip condition or conservation of tangential velocity. This is the reason why the longitudinal component of a Rayleigh wave does not generate waves in a liquid the same way the transverse component does. On the other hand for regular fluids,

$$\sigma_{solid} \cdot \hat{n} = \delta p \, \hat{n} \qquad (24)$$

since the stress in the solid at the interface is generated by the pressure inside the liquid due to continuity requirements. This is how the Rayleigh waves are generated from the longitudinal ultrasound waves.

There is a second type of interface in the system, the one between the liquid and the air in the environment. Air has a characteristic acoustic impedance, Z_0, as given in (21), much smaller than that of most liquids due to its much lower density and sound velocity ($Z_{0,air} \ll Z_{0,liquid}$). This causes air to act as soft boundary where the waves get reflected without changing their phase, thus

$$\delta p = 0 \qquad (25)$$

at the boundary between the liquid and the air. Therefore, air can be ignored and disregarded in the simulations by applying this boundary condition.

2.4. High Frequency Considerations

The basic solid and liquid material models discussed so far are simplified. For instance, especially the viscous liquids can exhibit the behavior of solids at very high rates and frequencies. In order to quantify the behavior of such materials, the Maxwell and Kelvin-Voight models of viscoelasticity are usually employed [82]. The conceptual schematics of these reports are given in Figure 2.4.

Out of these two models, the Maxwell model is usually used to define viscoelastic liquids since it can sustain creep indefinitely, thus shows the characteristics of a fluid rather than a solid [82]. The model consists of a spring to model the elasticity and a damper to represent the viscosity. The behavior of a Maxwell material can then be expressed in one dimension differential form as

$$\frac{dS}{dt} = \frac{1}{k}\frac{d\sigma}{dt} + \frac{\sigma}{\eta} \tag{26}$$

where S is the strain, k is the spring constant which serves as the modulus of elasticity, σ is the stress, and η is viscosity as defined before. If σ is a symmetric tensor and S tensor is represented in Cauchy's terms, then

$$2\eta S = \frac{\eta}{k}\frac{dT}{dt} + T \tag{27}$$

where T is the extra stress tensor and k is the shear modulus. This is the general form of equation (26).
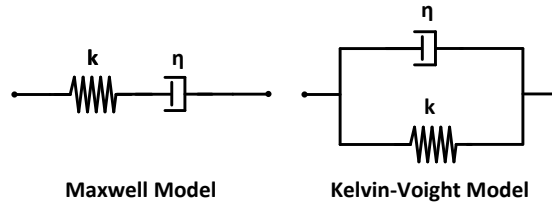
Figure 2.4. Maxwell and Kelvin models of viscoelasticity.

The $\frac{\eta}{k}$ term is called the shear relaxation time and characterizes the behavior of the fluid with operation frequency [83]. In order to see this effect more clearly, a harmonic time dependence can be assumed for the solution of T and plugged in (27) to obtain

$$T = \frac{2\eta}{1 + j\omega\tau} S \tag{28}$$

where $\tau = \frac{\eta}{k}$ and denotes the relaxation time. Going back to the definition of Newtonian liquids with shear viscosities it can be seen that if the transformation of

$$\eta_{effective} = \frac{\eta}{\eta_0} = \frac{1}{1 + \omega^2 \left(\frac{\eta}{k}\right)^2} \tag{29}$$

is made, the frequency dependent viscosity can be obtained. This is the link between a Maxwell material and a Newtonian liquid. Therefore the relation among operation frequency, viscosity, and shear modulus provides the limits for when the material behaves like a Newtonian liquid or a solid or somewhere in between [84]. The liquid material that is used in both the FEA studies and the experimental section is glycerin (or rather, its aqueous solutions). Figure 2.5

gives the Newtonian properties of glycerin in steady state: density, velocity of sound (or pressure wave speed), and viscosity.
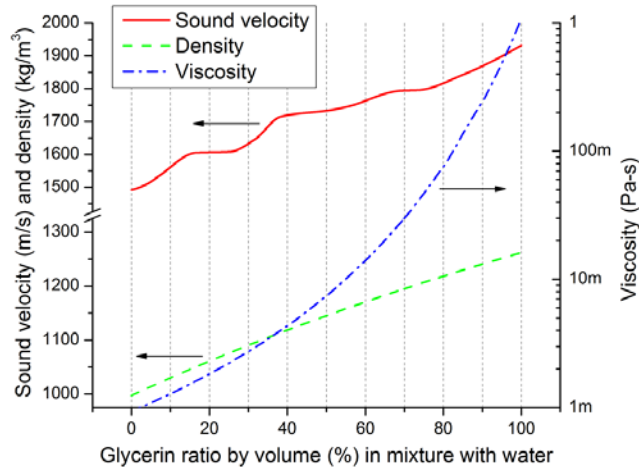
Figure 2.5. Properties of glycerin with respect to concentration in steady state.

These values are widely used data, and are obtained from the formulae derived from actual measurement results [85, 86]. Note that bulk or volume viscosity of glycerin varies according to concentration as well, although not linearly. For this case, the carefully collected data from [87] has been used. On the other hand, shear modulus parameter, k, is related to concentration as well. Articles written by Litovitz and colleagues decades ago are still regarded as very reliable sources of shear parameters of glycerin [87, 88]. Figure 2.6 gives the relaxation time of glycerin that is plotted by associating it with its viscosity given in Figure 2.5. Finally the effective viscosity in (29) has been derived for different glycerin concentrations as a function of operation frequency. For Newtonian fluid approximation, it should hold that $\omega\tau \ll 1$ to preserve viscosity. Figure 2.7 shows

a couple of different selections of ω and τ depending on glycerin concentration in the surface acoustic wave frequency ranges.

For lower ultrasound frequencies around 10 MHz, the liquid is completely Newtonian. For very high frequencies nearing GHz, the Newtonian approximation fails for high concentrations. Around 200 MHz, high concentrations of glycerin can easily be assumed to be Newtonian with small corrections according to (29). Figure 2.8 gives the real part of the viscosity correction factor for six different glycerin concentrations ranging from pure glycerin to pure water.
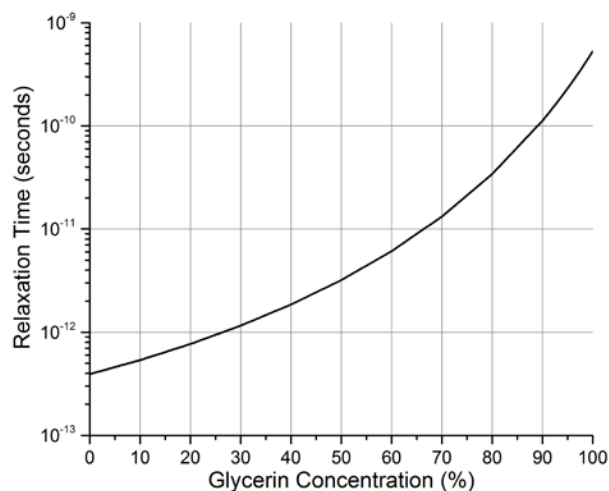
Figure 2.6. Relaxation time of aqueous solutions of glycerin, according to glycerin concentrations.

Taking into account the sizes of biological cells as the ultimate goal of detection, sizes of microcavities and IDT electrodes that are feasible with the current microfabrication capabilities, substrates that are usable, and for comparison with ultrasonic acoustic microscopy the operation frequency has been selected around 200 MHz to excite surface waves with wavelengths of 16 μm on ST-cut quartz. At this frequency range, only a small viscosity correction of

around 0.97 in the real part is required for 90% glycerin. Higher percentage of glycerin begins to show lower effective viscosities and start to exhibit solid properties that conform to the Maxwell model described.
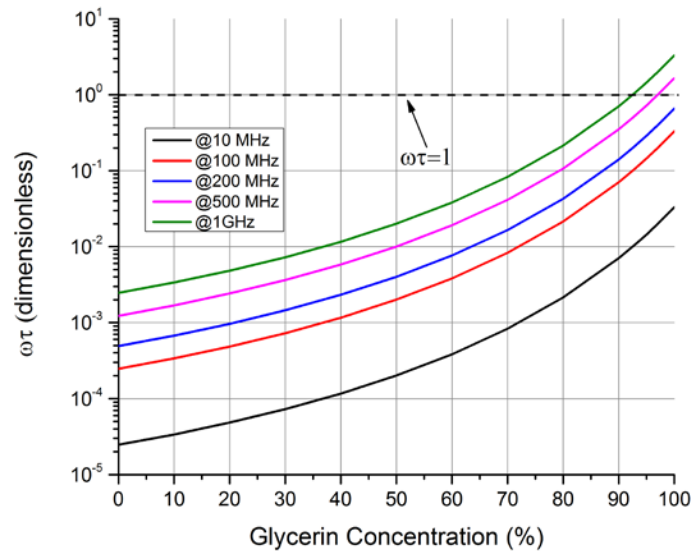
Figure 2.7. $\omega\tau$ parameter vs glycerin concentrations for aqueous solutions of glycerin.
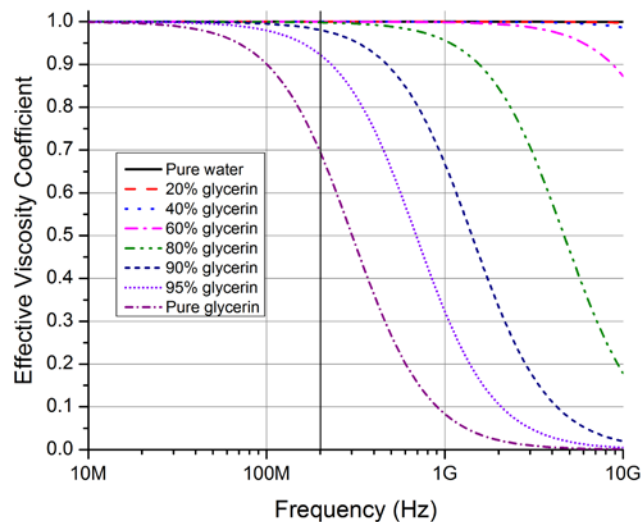
Figure 2.8. Effective viscosity coefficient defined in equation (29) with respect to glycerin concentration and operation frequency.

As a conclusion, the liquid can be considered Newtonian as the rates are not high enough for the behavior to resemble that of a solid. In essence, the spring in Figure 2.4 had been omitted whereas the viscosity has been corrected for use in a Newtonian fluid model. Solid microparticles are still considered standard elastic solids as a valid assumption.

2.5. Operation Principle

In order to couple the surface wave in the piezoelectric domain to that in the sample, boundary conditions (23) and (24) are used. One interesting aspect that arises from (23) is that it does not prohibit the generation of shear waves inside a liquid entirely, and there still exists a solution that satisfies wave equations with a dampening factor. This solution dictates that shear wave decays within a depth of

$$d_{shear} = \sqrt{\frac{2\eta}{\omega \rho_0}} \tag{30}$$

where the viscous contribution comes only from the viscosity (not bulk viscosity) and is proportional to it [89]. The penetration of longitudinal or compressional pressure waves, on the other hand, is negatively affected by viscosity effects as the ultrasound pressure wave penetration depth obtained from (9) will be inversely proportional to viscosity as:

$$d_{compressional} \approx 4 \frac{1}{\alpha} \tag{31}$$

A comparison of the penetration depths is given in Figure 2.9 as a function of glycerin concentration in water. It is seen that longitudinal wave penetration

dominates if the microcavity size is in the order of tens of microns. Therefore, the reflections inside the microcavity are going to be predominantly pressure waves.
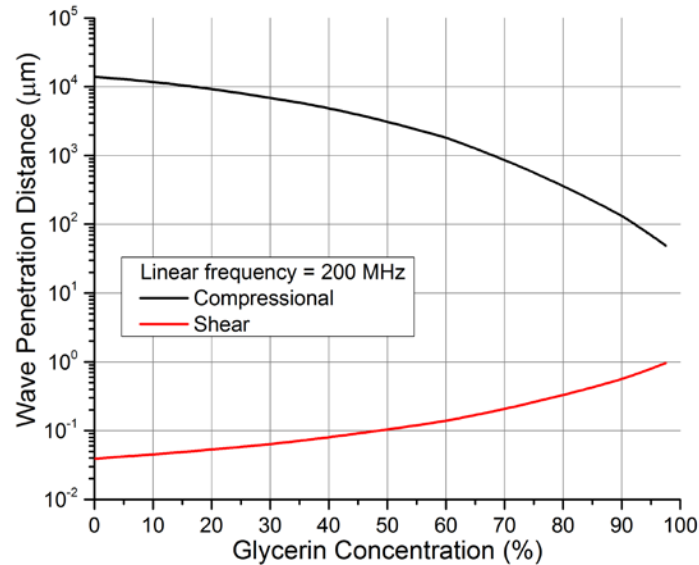
Figure 2.9. Shear and longitudinal wave penetration depths comparison as a function of glycerin content in water.

In the past, there have been studies in the literature to measure viscosity [90, 91]. These studies used plate waves to measure low or high viscosity with devices fabricated specifically depending on membrane thickness. Other more recent studies used shear waves and displacements [83, 92-94] and their coupling. On the other hand, Lamb waves [95] and Rayleigh waves have been used in [96-99].

The modeling used in this study differs from the studies given in the literature in a couple of ways. Primarily, the difference is in types of liquid coupling and frequencies. The wave modes as well as dimensions are different from those of the plate wave mode sensors causing different properties of the liquid to be utilized. Lamb wave-mode sensors operate at very low frequencies

compared to the others and were shown to be accurate for low concentrations of glycerin. Shear wave modes incur displacements along horizontal directions and couple only in shear mode to the liquids. Second important point is that the nature of the system and operation frequencies used allow for use of a modified Newtonian liquid model as opposed to Maxwell models. Finally, the amount of sample captured is orders of magnitude smaller than other studies. For this reason, although the current study uses similar frequencies and the same wave mode as in studies by McHale and Newton, et al., the reflections from the top surface of the sample cannot be safely ignored.

The system operation can be seen in Figure 2.10. When the Rayleigh wave generated from the source side encounters the microcavity it continues propagation along the sidewalls and the bottom of the microcavity towards the output IDT. Some part of the surface wave might be mode converted to bulk waves and lost to the substrate due to the angle of the sidewalls. If a sample is placed inside this microcavity, it starts generating waves inside it which get partially transmitted back to the piezoelectric substrate and partially reflected back to the sample. This causes a resonant cavity condition to occur inside the microcavity defined by the properties of the sample. This is illustrated in Figure 2.10.

The system operation can be simplified and expressed in terms of only the longitudinal component as follows

$$u_{Resultant} = u_{Modified} + u_{Sample} \tag{32}$$

$$u_R = A_1(\rho_m, v_m) \ (C_1 \exp(-\alpha kz)) \ \exp[j(kx - \omega t)]$$

$$+ A_2(v_m) \ (C_2 \exp(-\alpha kz)) \ \exp[j(kx - \omega t - \phi(\rho_m, v_m))]$$

(33)

where the resultant wave acts a combination of the modified wave and the wave generated by sample as shown in Figure 2.10. Note that both ρ_m and v_m terms include the effect of viscosity implicitly as defined by (10) and (11). For smaller dimensions of microcavities, the first term on the right hand side of dominates and the system acts closer to a mass loaded system. This behavior will be shown in the next section. As microcavity dimensions get closer to that of the wavelength, the system relies more on the ultrasound waves coupling back from the sample. The results are observed as a phase difference in the output.
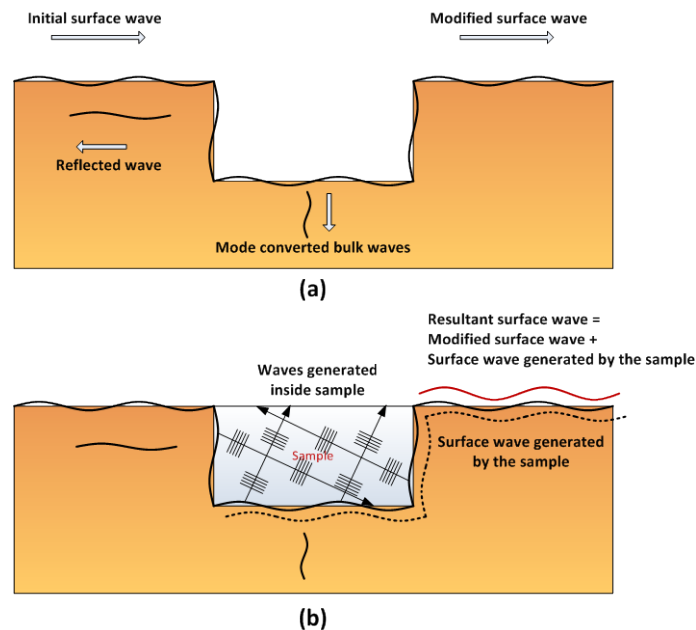
Figure 2.10. System operation.

In the proposed system, it is obviously only possible to inspect only the resultant wave that reaches the output but the primary interest lies in the perturbations introduced by the waves from the sample in the microcavity.

Rayleigh waves in simulations are not simple plane waves considering the interactions they undergo, and the coupling between the piezoelectric and liquid media works in both directions. Consequently, the model cannot be reduced to a simple 1D counterpart to obtain insight while keeping it functionally equivalent. Furthermore, the system needs to be solvable for arbitrary geometries. Since analytical modeling is very difficult because of these reasons, a fast and powerful alternative is required to solve the behavior of this intricate system.

2.6. Biological Cell Modeling

Liquid and solids as discussed in this chapter have behaviors defined down to very good approximations by the described models given the experimental conditions. Biological cells are much more complicated as their behaviors are more dependent environmental conditions, their internal dynamics, and most importantly, the method of measurement.

Continuum models stem from extension of mechanical properties throughout the cells and approximating the behavior by a continuum approach. Usually this family of models is better suited for computational purposes although they can be improved on by using nanostructural approaches once information is obtained [100]. Due to their versatility, different types of continuum models shown in are outlined and discussed below.

When cells are in suspension, it is reasonable to model them similar to liquids. The first modeling approach is a Newtonian liquid (see Figure 2.11(a)) where the cell acts like it has a constant viscosity throughout the entire frequency

spectrum. This model is usually employed to approximate the behavior for micropipette aspiration studies where the cell is halfway aspirated into a micropipette by applying a step change in suction pressure and measuring how long it takes the part of the cell aspirated into the micropipette reaches steady state [101]. Therefore, it is usually associated with relatively large deformations in the order of microns. The nucleus, encompassing about 20% of the total cell volume, is assumed to be denser and more viscous compared to the cytoplasm [102]. Corrections to this type of behavior can thus be made for even larger deformations by assuming the cytoplasm and nucleus are assigned two different viscosities as shown in Figure 2.11(b). Another type of correction is the shear thinning liquid model where the liquid is assumed to have a viscosity that decreases with increasing rate (or frequency) as shown in Figure 2.11(c) [103]. It should be noted that studies involving small deformations have been less successful with the shear thinning method [100]; therefore, it is not as relevant to the SAW microsystem study involving very small displacements.
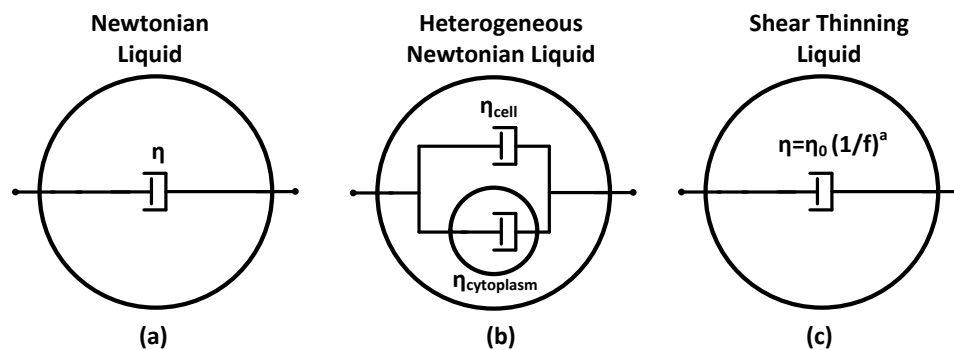
Figure 2.11. Liquid based approaches for modeling cells.

The simplest model among all models is the linear solid model where the cell assumed to be a spring with linear deformation as given in Figure 2.12(a).

Evidently, this model has major shortcomings as it does not contain any time or rate dependent information. Elasticity is the parameter of interest and is usually measured using an AFM [58].

The limitations of the simple elastic solid model are overcome by use of a dampening element to account for time dependent effects as shown in Figure 2.12(b). Usually, a single time constant is assumed to be associated with the cell, hence a single dampening element is incorporated into the model. This element is represented by a certain viscosity which implies a Maxwell model as defined before in this chapter. Consequently, there exists a creep response to instantaneous deformation and this response has a time constant or a relaxation time defined by the values of elasticity and viscosity. This is usually denoted as a viscoelastic or Maxwell model. The model can be extended with use of two elastic elements and one viscous element to fit the obtained behavior from results as shown in Figure 2.12(c). Tapping mode instead of static contact mode is the preferred way to add the effect of frequency and obtain the viscosity (or damping) effects of relaxation in AFM studies [57].
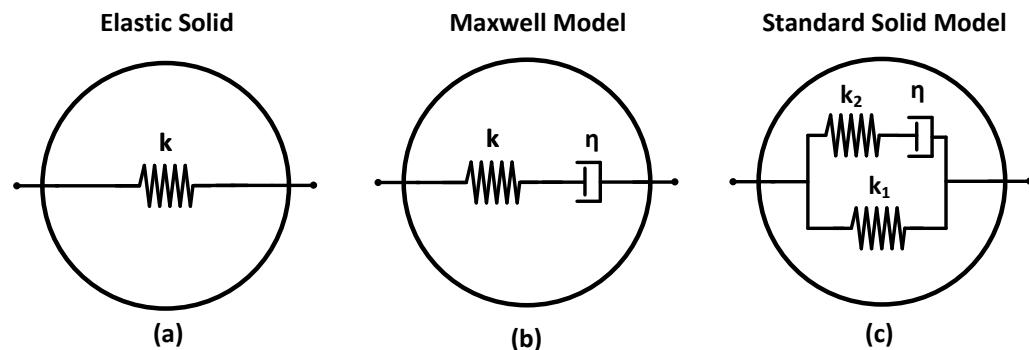
Figure 2.12. Solid models of cells.

In general, the mechanical behavior of cells is dependent on many factors. First one to be considered is frequency. Although cells are elastic in general, they have a pronounced recovery behavior. When external stimuli at frequencies lower than their relaxation time are applied, they deform and then recover accordingly. However, if the frequency of the stimulus is larger than the relaxation time, they act more like solids as they do not have time to react [104]. In this manner, they are similar to the high frequency characteristics of aqueous solutions of glycerin. The mechanical relaxation effect is evident in AFM, micropipette aspiration, and magnetic twisting studies alike. However, the time constants and elastic moduli obtained from these studies are in the order of ~1 second and ~1-10 kPa. This is a seemingly major issue for higher frequency studies as these properties suggest very soft elastic media and ultrasound waves can be sustained at these frequencies based on the solid models based on the wave velocity defined in (14). This means no waves would be transferred to the cell due to its low characteristic acoustic impedance, defined in equation (21). However, studies suggest ultrasound waves of at 375 MHz and 500 MHz can be sustained in biological tissues as well as single cells.

This brings up an important point. The cells most likely change their complex modulus according to a power law. Approximately two orders of magnitude of increase in complex modulus is documented up to frequencies of 1 kHz in [105] for HASM cells with magnetic cytometry. Acoustic microscopy studies also suggest that waves exist and can propagate inside cells as shown in [65, 106]. It is not really known why the complex modulus increases as frequency

does but it is hypothesized that high frequency behavior might be dominated by the rheological properties of actin filaments [107].

Another factor that defines the behavior of cells is the nature of the experiments. AFM measurements are taken via sharp probes and therefore represent the response of a very small area of the cell rather than the whole cell. Micropipette aspiration deals with large deformations which are comparable to the cell dimensions in magnitude. The proposed system has displacements in the order of picometers to generate ultrasound waves. Considering the size of the cells studied (~10-20 μm), deformations in question are expected to be many orders of magnitude smaller.

One other factor that changes cell behavior is their state, i.e. whether they are dead or alive or fixed, cancerous or healthy, in suspension or dried out, etc. In order to keep the cell intact and alive, and the system non-invasive, the cells should be suspended in their solution and they should not be fixed. At this point, under otherwise same conditions, different types of cells can be compared for their mechanical properties that are devoid of the effects of these external stimuli.

In the light of these data, the studies comparable to the proposed one are the acoustic microscopy studies considering the frequency range and experimental conditions. There are no other studies completed at such high frequency ranges to the best of the author's knowledge. Consequently, the parameters for cells were obtained from acoustic microscopy studies. If a

viscoelastic fluid model is considered as before, the velocity of ultrasound in the liquid can be written in terms of bulk and shear moduli, and density as

$$v_u^2 = \frac{K + \frac{4}{3}G}{\rho_0} \approx \frac{K}{\rho_0} \tag{34}$$

where v_u is the velocity of ultrasound, K is the bulk modulus, G is the shear modulus, and ρ_0 is the density. The shear modulus can be neglected in cells at these frequencies as $K \gg G$ [15]. This bulk modulus parameter can be converted to regular elasticity modulus or Young's modulus (denoted by c before) by the well-known relation

$$E = 3K(1 - 2v) \tag{35}$$

where v is the Poisson's ratio. The Poisson's ratio has been measured as ~0.33 before in some studies in the literature such as [108]. Therefore, it is assumed that bulk modulus is approximately equal to Young's modulus for biological cells. Therefore the model looks like that of Figure 2.13(a), a Maxwell material. Apparent viscosity of the cell can be obtained using expressions of (8) and (9) based on frequency dependent attenuation constant. The equation (9) as it applies to attenuation can be used to derive a loss factor related to viscosity for cells as

$$A(\mathrm{x}) = A_0 \exp(-\alpha \mathrm{x}) \tag{36}$$

and can be used to obtain the viscosity figures if the distance related with the attenuation is known. These equations are plugged into studies in [65, 109] to obtain the order of magnitude for the values shown in Figure 2.13(b).
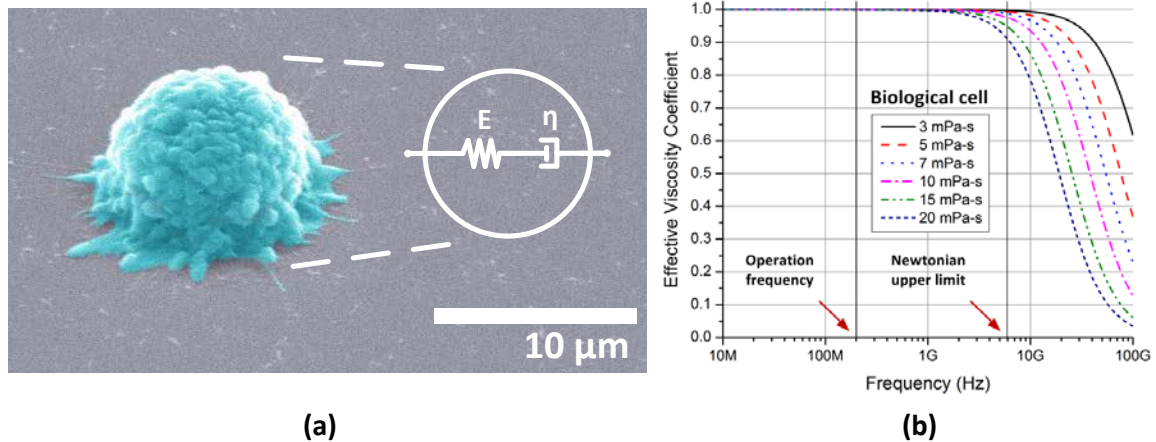
Figure 2.13. (a) The Maxwell model shown on an A-431 cell. (b) Effective viscosity coefficient for acoustic modeling of cells. For a wide range of viscosity values, the cells exhibit liquid-like characteristics around 200 MHz in the Newtonian region. The transition to a complex material or solid-like material models is made at much higher frequencies in the order of GHz's.

For the viscoelastic Maxwell model detailed in this study, a single time constant is assumed, and attenuations are mainly governed by viscosity with the values obtained as explained above. The low frequency region is described as the Newtonian region where the material acts as a liquid. At very high frequencies, the material acts as a solid as it cannot react fast enough to periodic changes in stress. Putting all these together, the cells at high frequencies are modeled as Maxwell materials in suspension with the exception that no shear waves are supported in the bulk of the cell. Regular values for density, ultrasound velocity, viscosity, and related elasticity are therefore around ~1000 kg/m^3, ~1500-1800 m/s, ~5-10 mPa·s, and ~2-3 GPa, respectively.

CHAPTER 3: MODELING AND DESIGN

The previous chapter dealt with the theory and mechanics of the proposed system. This chapter mainly discusses how finite element analyses were carried out to obtain the characteristics of the sensing platform. Firstly, the correct wave mode is identified, and 2-port SAW filters are modeled without microcavities. Then, elementary models are presented to show coupling between media and this discussion is extended to operation with microcavity and sensing. Finally, matching circuits and devices are discussed.

3.1. Introduction to FEA

Finite element analysis (FEA) is a powerful tool that models continuum problems well-defined by partial differential equations (PDEs) by discretizing the continuous behavior through the mutually interacting small elements in the form of a mesh. In simulations of waves, it is shown that elements smaller than 20% of the wavelength gives reliable results [75]. In order to obtain the transfer characteristics, the system can be solved in either one of two equivalent ways: direct frequency domain solution or time domain solution which is later converted to frequency domain using discrete Fourier transform [71]. For frequency domain analysis, all the PDEs are assumed to be harmonically varying with time according to the same $\exp(j\omega t)$ dependence.

First of all, the wave modes in the system need to be identified to obtain Rayleigh waves as proposed. Afterwards, transfer function of a regular SAW delay line will be obtained. Following this, addition of the microcavity will be

50

investigated. Finally, the effect of addition of the samples of interest into the microcavities will be discussed. Rayleigh wave modes in both ST-cut quartz and Y-cut lithium niobate are explored. Due to constraints imposed on the system by microfabrication capabilities, the emphasis was placed on quartz. The wavelength, λ, is taken as 16 μm taking into account both the cell and microcavity sizes for best interaction as well as the microfabrication capabilities.

3.2. Eigenfrequency Analysis

The wave modes were identified using harmonic analysis performed on a two-unit-cell (2λ long) structure. Periodicity conditions were applied to the two ends of the structure whereas a fixed boundary condition was applied to the bottom of the structure to ascertain that the wave decays as discussed in the previous chapter. Electrodes were assumed to be massless. Wave velocities were calculated as 3446 m/s and 3219 m/s, respectively on Y-Z lithium niobate and ST-X quartz. The tabulated phase velocities of these waves are 3488 m/s and 3158 m/s. The displacement color and arrow maps for quartz are shown in Figure 3.1.
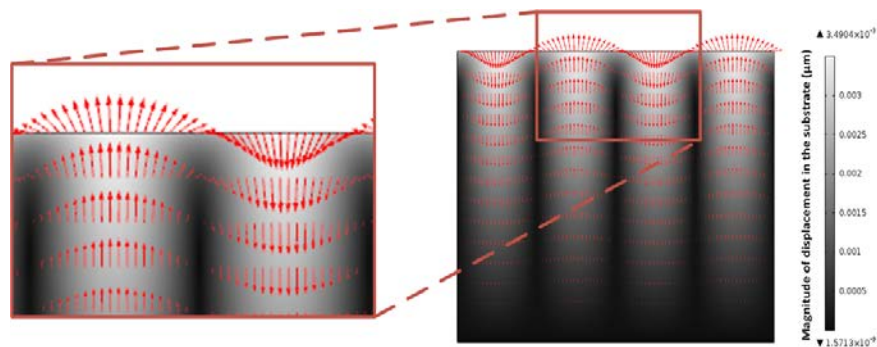
Figure 3.1. Displacement map in quartz shown with arrows indicating displacement as well as a color map.

Discrepancies can be attributed to small differences in piezoelectric coefficient matrices of coupling, elasticity, and relative permittivity. It should be mentioned that deviations due to the presence of real electrodes can be expected in experimental conditions as electrodes inherently cause mass loading.

It should be noted that a rotation matrix needs to be applied to material tensors. For ST-X quartz this corresponds to right handed Euler angles of (0, 132.75, 0) or equivalently (0, -47.25, 0). The same goes for lithium niobate where the right handed Euler angles are (0, 90, 90).

3.3. Device Level Surface Acoustic Wave Analysis

The transverse component of the Rayleigh wave is polarized in the vertical direction. This means that the system can be reduced to a 2D model without losing information as long as out-of-plane changes are negligible. Since quartz has a low electromechanical coupling coefficient of 0.11%, and the aperture needs to be kept small so that it is comparable to cell sizes, many electrode pairs are needed to obtain a reasonable insertion loss level at the passband. The delay line length is not a very important design parameter but is kept small to alleviate the attenuation of the Rayleigh during propagation in quartz. All parameters for the 2D model are given in Table 3.1.

A fixed constraint boundary condition was applied to the bottom of the substrate to set all displacements equal to zero. This is necessary to limit the simulation to surface waves and make them decay as they go into the substrate. A very important issue is the size of the model. If a finite sized substrate is

modeled, surface acoustic waves will reflect from the edges back into the area of interest to form standing waves. In experiments, however, the substrate is much larger than the device which allows the surface wave to leave the system. In order to model a smaller and more manageable system while keeping it functionally the same, perfectly matched layer (PML) boundaries were applied to the system in all directions. These boundary conditions are mathematically arranged to represent a very large area in a small area to model the waves leaving the system. The 2D model with PMLs along with the mesh quality histogram corresponding to the simulation model is shown in Figure 3.2. The frequency was swept around the center point of ~200 MHz which was obtained from the eigenfrequency analysis in the previous section. The output is obtained in the form of scattering parameters, specifically, the insertion loss or S21. These results are given in Figure 3.3.

Table 3.1. Finite element simulation 2D model parameters.

Substrate	Quartz (ST-X)	Wavelength (λ)	16 µm
Electrode pairs	64	Microcavity width	Varies (λ–1.5λ)
Electrode width/spacing	4 µm/4 µm	Microcavity depth	Varies (0.125λ–λ)
IDT separation	6λ	Mesh Elements	~25,000 (triangular)
Depth	2λ	Degrees of freedom	~300,000
Aperture	1.5λ	Shape Function Order	Quartic
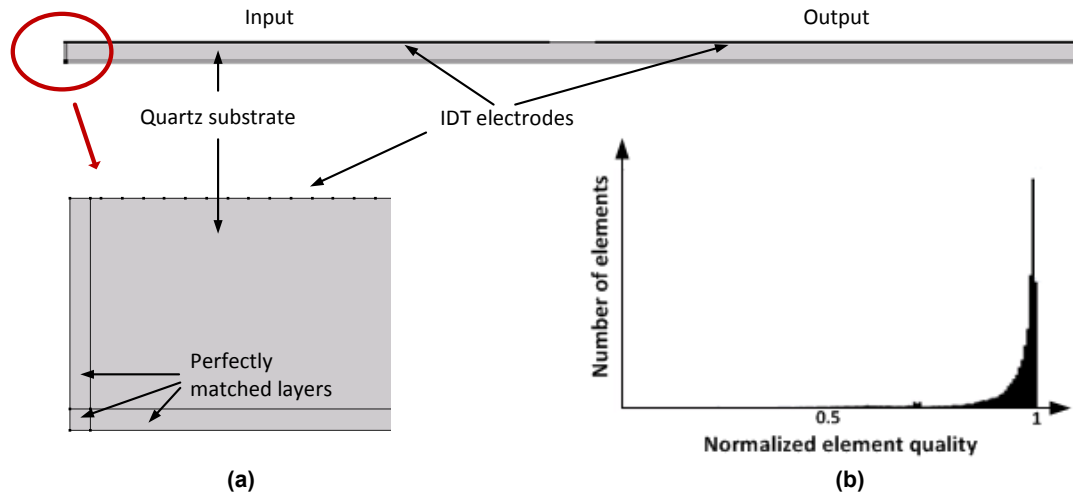
Figure 3.2. (a) The 2D FEA model up close and (b) the element quality histogram showing the normalized quality distribution of elements.

Introduction of microcavities disturbs the continuity of the delay line, and it is seen to increase the magnitude of insertion loss as shown in Figure 3.4. The Rayleigh wave is still observed to travel along the sidewalls and bottom of the microcavity. However, some portion of it is reflected back towards the input similar to the case with groove type absorber/reflector configurations used in SAW filters. Some portion of the Rayleigh wave is seen to be dispersed and converted into bulk waves. In geometries where this conversion is less efficient, comparatively better insertion loss characteristics are observed. For instance, in $\lambda/2$ deep microcavities with 1.5 λ width, conversion is stronger than in even deeper cavities, thus larger losses are observed. Since most of the surface wave energy is constrained to a depth of one operation wavelength from the surface, depths up to and including λ are considered.
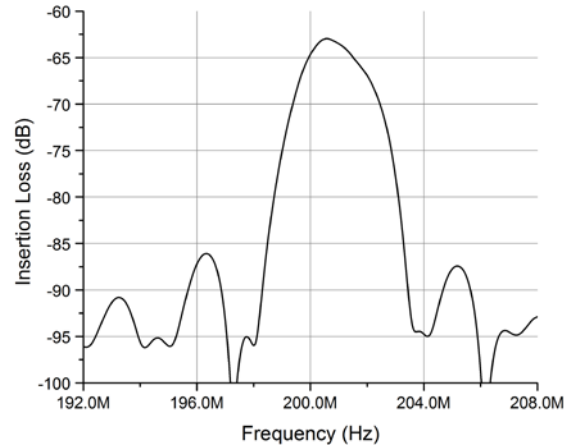
Figure 3.3. Simulation results from the 2D regular delay line.
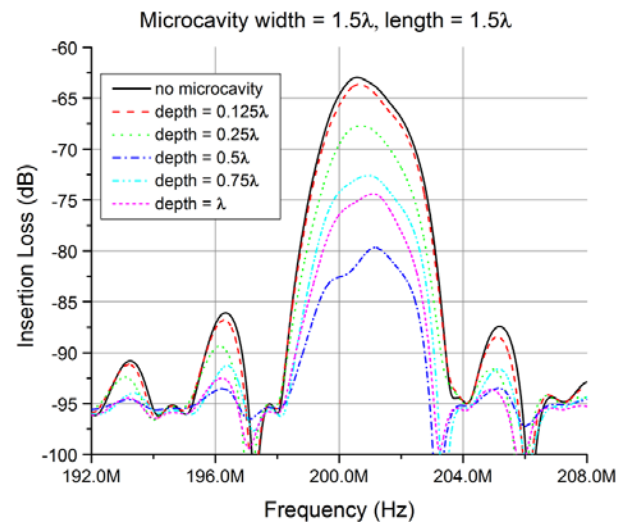
Figure 3.4. Simulation results with microcavity.

3.4. Coupling Between Domains

Coupling between domains occurs according to the boundary conditions defined in equations (23), (24), and (25). In order to separately identify the parameters, the microcavity was not included at this stage. As mentioned before, ultrasound waves are generated in liquids with the excitation from the transverse component of the Rayleigh waves. For the first model, both viscosity and bulk

viscosity were ignored and a liquid with density, ρ_0 of 1000 kg/m³ was used. The ultrasound velocity, v_u, of the liquid was changed between 1500 m/s and 1800 m/s in four steps. Note that since there is no viscosity applied, there is no attenuation in wave propagation. Also, note that PML conditions were applied again to prevent reflections from the liquid domain. The angle of ultrasound excitation changes as shown in Figure 3.5 as expected. It should be noted that ultrasound velocity also affects the wavelength in the liquid in a linear fashion for a given frequency as $v = \lambda \cdot f$.

(a) v_u=1500 m/s, θ_u=27.8°   **(b)** v_u=1600 m/s, θ_u=29.8°

(c) v_u=1700 m/s, θ_u=31.9°   **(d)** v_u=1800 m/s, θ_u=34.0°
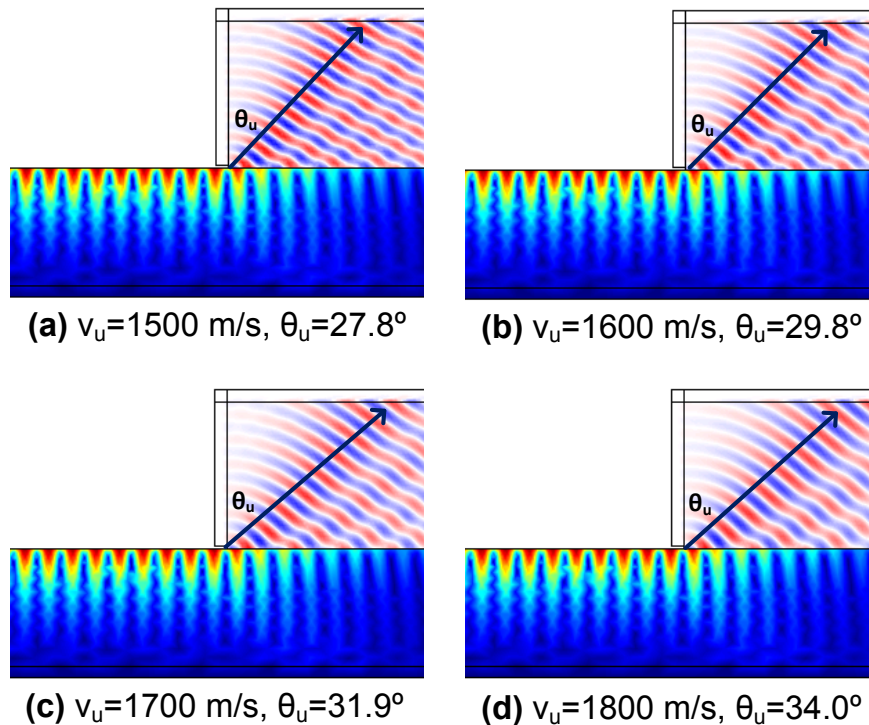
Figure 3.5. Simulation results showing the angle of ultrasound excitation.

While the density only has a small effect on the incidence angle since it is correlated to velocity indirectly, it directly affects the pressure level transferred to the liquid domain according to the resultant acoustic impedance. If η and η_B are

considered to be equal to each other, the effect of density and viscosity on attenuation can be observed as given in Figure 3.6. For v_u set to 1610 m/s and for varying ρ_0 and viscosities, the sound pressure level transmitted to the liquid was calculated and seen to agree well with theory. It can be seen that density affects the pressure linearly while an inverse linear relationship exists between viscosity and pressure level. The reason for the inverse relationship is that more viscous the liquid, less energy is transferred to it because of dampening. As the viscosity is increased, the penetration depth decreases and this causes less and less energy being transferred to the liquid.
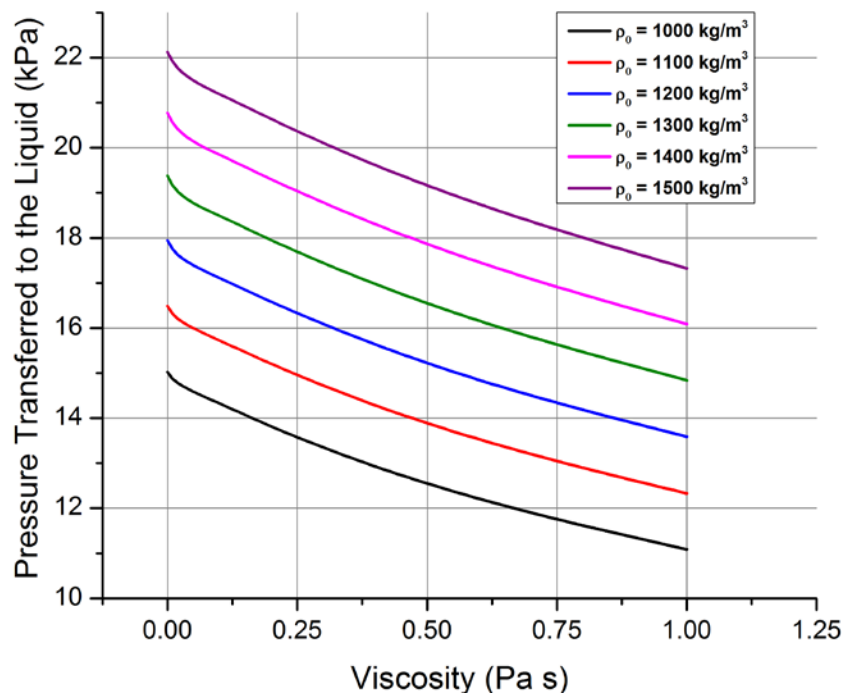
Figure 3.6. Simulation results showing the effect of viscosity and density.

Similar simulations were carried out for solids. Barring the mode conversion and limiting the process to the longitudinal wave, the transmission is heavily dependent on the modulus of elasticity as shown in Figure 3.7.

Transmission the plot shows that transmission is only effective starting near about 1 GPa range of stiffness (or modulus of elasticity). At low stiffness values, most of the wave is already reflected back, making it very difficult to use it in a transmission mode device such the one in this study. On the other hand, polystyrene, with Poisson's ratio and stiffness around 0.35 and 3 GPa, can readily interact with surface waves near a frequency of 200 MHz.
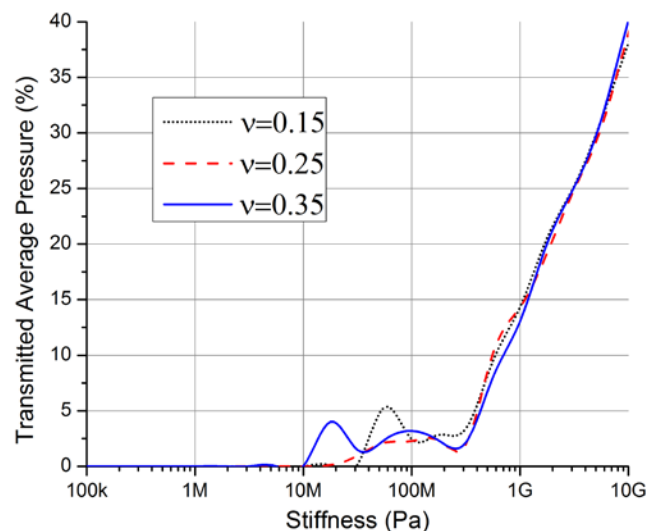
Figure 3.7. Simulations showing elasticity dependent transmission of longitudinal waves to linear elastic solid domains for three different Poisson's ratios at 200 MHz.

3.5. Resonant Cavity Condition in the Microcavity

Placement of the liquid into the cavity causes the SAW to couple into the liquid and form compressional waves. The resultant waves have an angle of incidence defined by Snell's law, i.e. according to the ratio of the wave velocity of the two domains. It should be noted that the longitudinal component of the Rayleigh wave does not couple into the liquid. The component responsible for emitting acoustic radiation into the liquid is the transverse component that travels

along the microcavity sidewalls. Time domain simulations showed that about five full wave cycles after the wave first reaches the microcavity, a resonant cavity condition is attained. This condition is then maintained in the liquid as dictated by its geometry. This is evidenced by the simulation results shown in Figure 3.8.
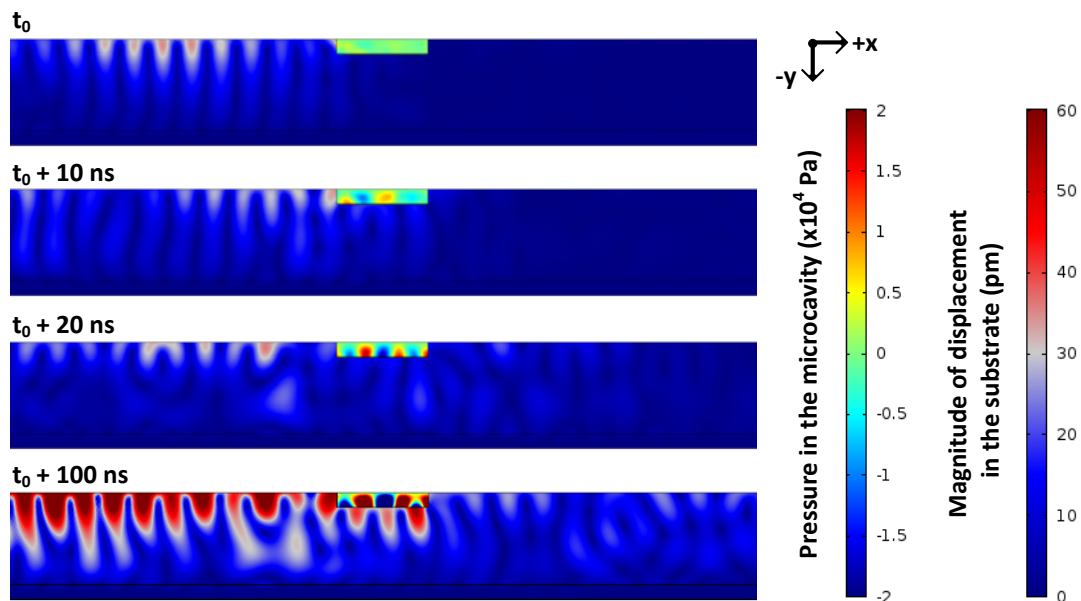
Figure 3.8. Time domain simulation showing the onset of the resonance inside the microcavity. Color bars apply to all instances in time.

When the wave is first emitted into the cavity, it travels in the +x/-y direction with an angle defined by Snell's law as discussed above which, in our case is between approximately 27° to 36° depending on the liquid sound velocity. Some part of it couples to the piezoelectric substrate, some of it gets reflected and travels to the boundary above. The simulated interface to air at the top reflects the waves according to a soft boundary condition which maintains the phase. This process repeats for the rest of the width of the microcavity. The part of the surface waves traveling from the bottom of the cavity also launches

acoustic waves into the liquid. Putting it all together, the geometry of the microcavity, namely width and depth, cause it to act similar to a 2D resonant cavity bounded as given in Figure 3.9. As the microcavity depth increases, more wavelengths circulate in the y-direction in the liquid hence the resonance becomes more intricate.

Depth = 4 μm (0.25λ)   Depth = 12 μm (0.75λ)

Depth = 8 μm (0.5λ)   Depth = 16 μm (λ)
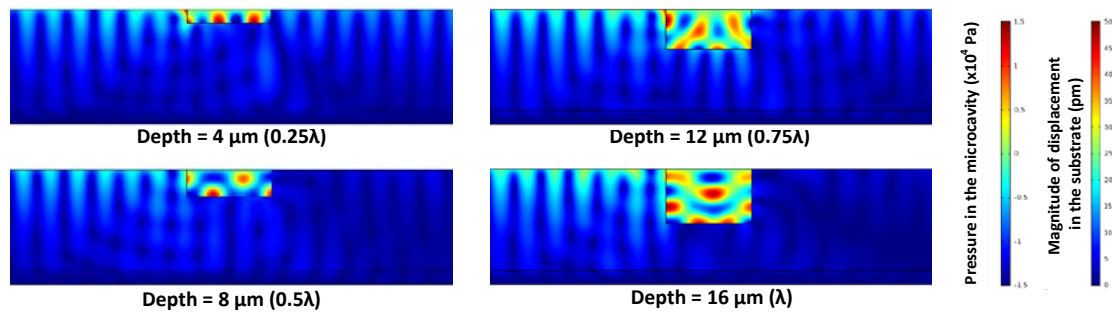
Figure 3.9. Simulation of resonance condition inside the microcavity.

3.6. Sensing Glycerin Concentration

For the same microcavity, amplitudes of the acoustic waves decay and the wavelength of the acoustic waves increase when glycerin concentration is increased. It should be noted that density, velocity of the ultrasound, and viscosity all change with respect to glycerin concentration. Therefore, the output is dependent on all of these parameters. A plot of these parameters was provided in Figure 2.5. The waves transferred to and trapped inside the resonating microcavity couple back to the surface waves and give rise to interferences. The characteristic insertion loss plots are given in Figure 3.10 for two different cavity depths, 4 μm and 12 μm.
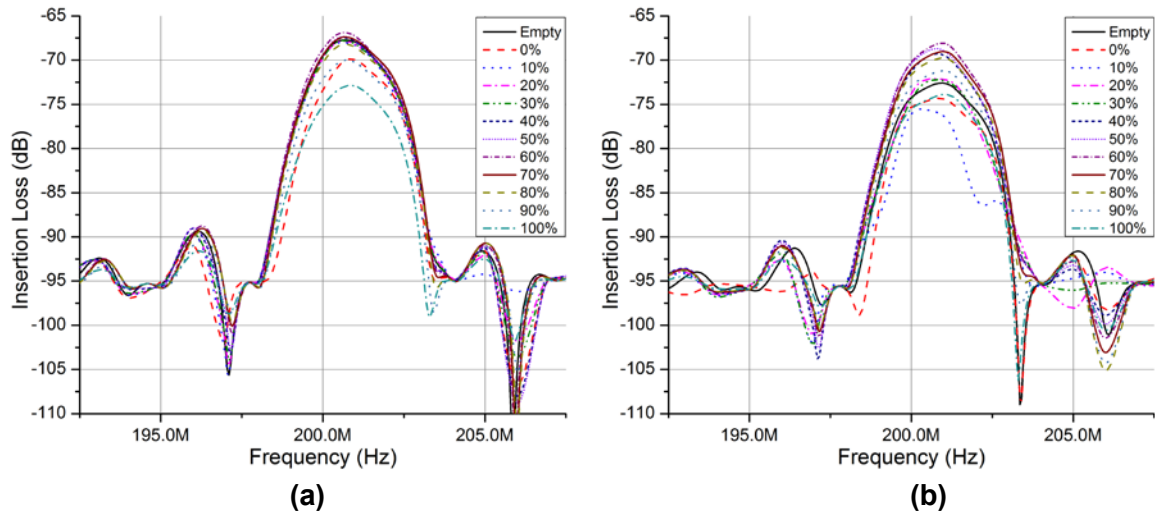
Figure 3.10. Simulated insertion loss for devices with (a) 4 μm and (b) 12 μm deep microcavities for empty microcavities and various concentrations of glycerin in water.

The magnitude of insertion loss is seen to increase and decrease with different liquids while frequency shifts are observed with different profiles. The deeper microcavity of 12 μm is seen to respond with higher magnitude shifts. However, it is seen that direct observation of insertion loss plots is difficult due to numerous samples. For this reason, results are compiled and electrical transfer characteristics are compared for three parameters of interest: peak frequency shifts, change in insertion loss magnitude, and phase information. The study is repeated for different microcavity depths of 2 μm, 4 μm, 8 μm, 12 μm, and 16 μm, which result in different resonance conditions due to specific geometries. The trapped liquid volumes are 1.2 pL, 2.3 pL, 4.6 pL, 6.9 pL, and 9.2 pL, respectively. The results are shown in Figure 3.11, Figure 3.12, and Figure 3.13.
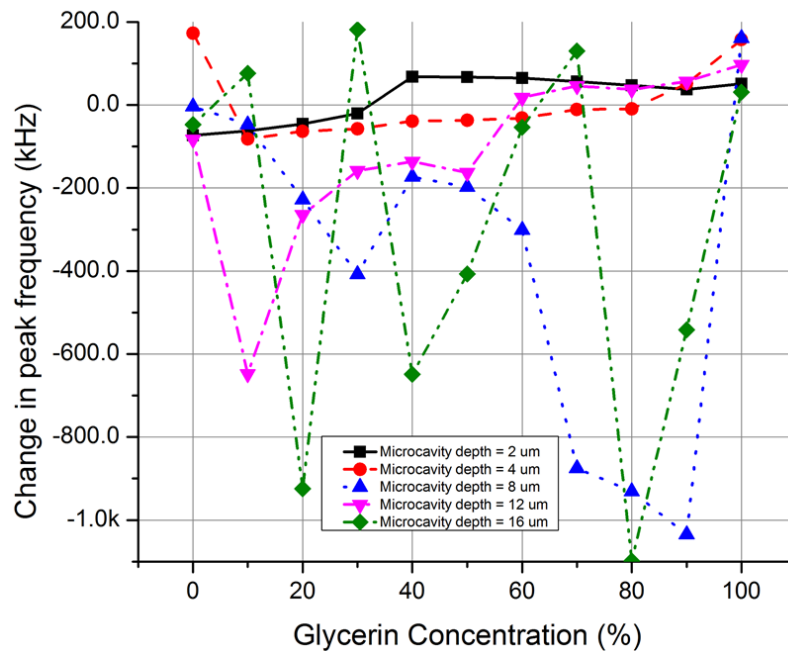
Figure 3.11. Simulated change in peak frequency vs glycerin concentration.
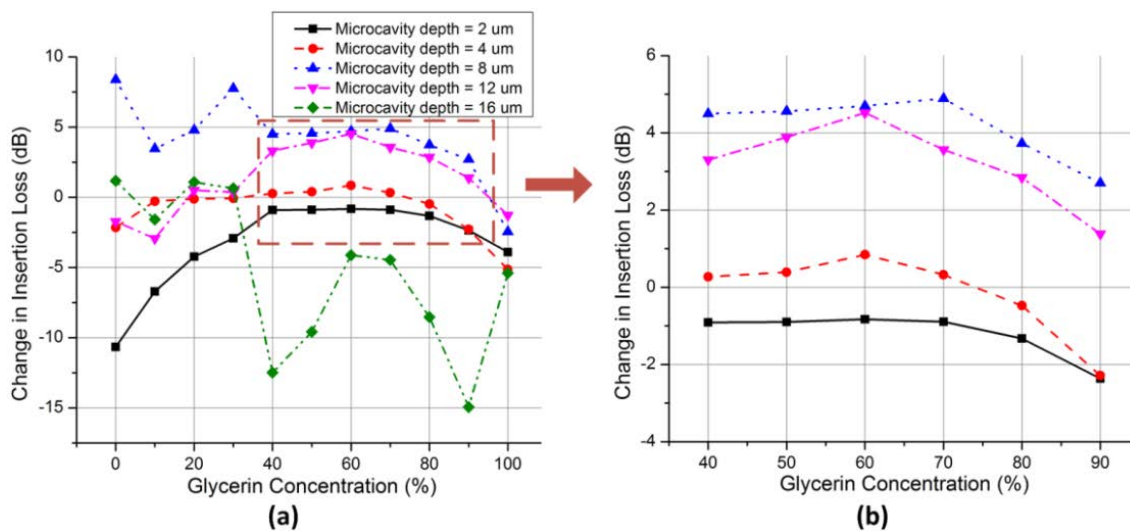
Figure 3.12. Simulated change in insertion loss vs glycerin concentration.
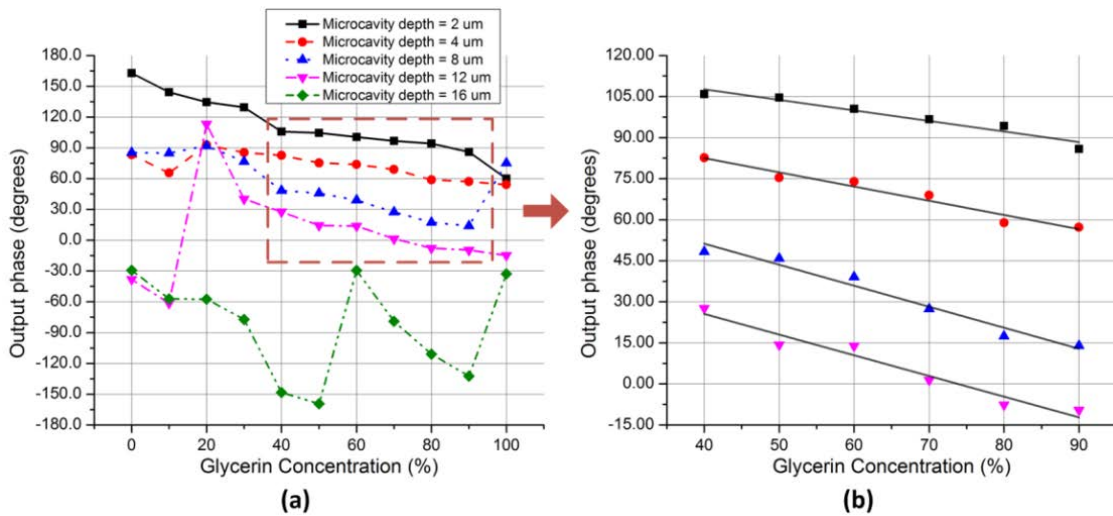
Figure 3.13. Simulated change in phase angle vs glycerin concentration.

It was noticed that wave velocities for glycerin concentrations smaller than 40% are not linear in measured data taken from literature so the outputs in the low concentration region yields spurious fluctuations. Furthermore, excessively high glycerin concentrations cause significant attenuation of the acoustic waves. This is a direct result of the high viscosities in these mixtures which causes exponential decay of pressure within the liquid. For instance, pressure exponentially decays to 0.37 of its initial magnitude after traveling a distance of less than 5 μm in the liquid domain in the simulations for 100% glycerin which holds according to equation (9). Furthermore, >90% concentrations of glycerin start to exponentially increase in relaxation time and move away from the Newtonian approximation as illustrated in Figure 2.7 and Figure 2.8. Therefore, for the proposed method to be effective and consistent with the data being used, the glycerin concentrations of 40% to 90% are considered. Within this region, phase information provides good correlation with parameters.

The changes in insertion loss magnitude are mainly due to conversion of a geometry dependent portion of surface waves into bulk waves which are lost to the substrate. Since PML type domains are employed, these waves do not interfere with the output further but their generation causes drops in the magnitude and extraneous coupling from the surface waves to liquid increases the magnitude. The frequency shifts are the result of the microcavity acting as a surface corrugation that modifies the response [110]. However, this modification is minimal as there is only a single microcavity. It is observed that, overall, the system does not show the characteristics of a mass loaded system. In case of a mass loaded system, a strong negative correlation exists between peak frequency and mass. Although a somewhat similar relation is observed for very shallow microcavities of 2 μm, larger depths operate in a different fashion. In case of deeper microcavities, piezoelectric-liquid coupling and resultant interferences dominate. The relations in this region are highly dependent on depth and are not strongly correlated to the mass as opposed to what is typical of mass loading. This fact points to a different detection mechanism.

On the other hand, the output phase gives useful information as to how the incident Rayleigh surface wave has been delayed. The system is expected to be cyclic in the way the phase changes with respect to liquid properties. For relatively large cavity depths such as λ, the system is seen to oscillate in its phase. Apart from the bulk wave conversion, reflections are reasonably more dominant for the depth of λ. Due to its larger size, a large number of pressure minima and maxima occur inside the liquid region, and distances traveled by the

waves before hitting a boundary are larger. For these reasons, symmetries are harder to obtain in deeper cavities. Inspection of the resonance condition was carried out with a multitude of liquids. It was seen that a combination of these effects breaks the relation between glycerin concentration and phase for microcavities as deep as λ. For very shallow cavities, the distance traveled before hitting a boundary is minimal. In such cases, the model is dominated by the waves emitted into the microcavity from below but not from the side. In the end, viscosity is not the leading factor as it governs attenuation for the traveled distance. Since the angle of refraction of the waves in the liquid are directly related to the sound velocity, the correlation between wave velocity and phase is very high for very shallow cavity conditions, such as 2 μm deep microcavities as shown in Figure 3.14(a). A linear curve fit with $R^2 > 0.99$ gives a sensitivity of -0.13 °/(m/s). For larger depths, higher variations are observed due to the effects of viscosity. The relation of phase angle with viscosity is given Figure 3.14(b).
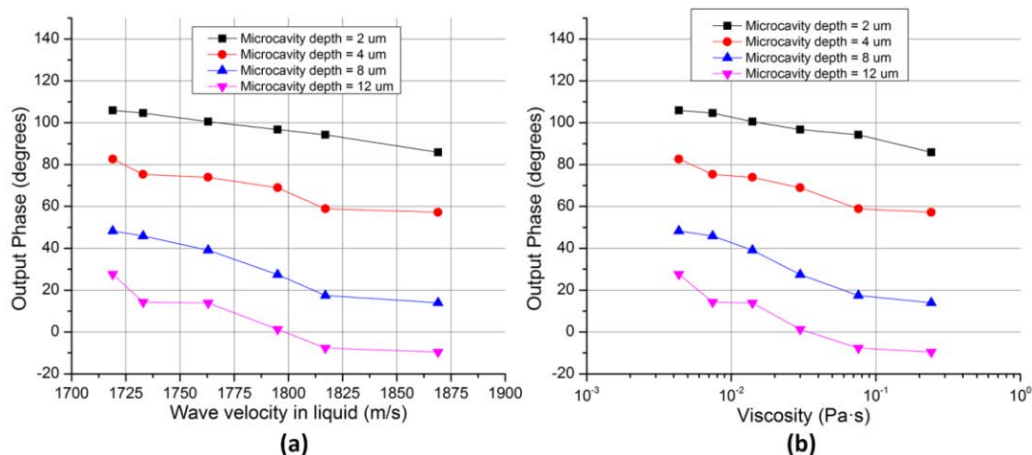
Figure 3.14. A closer look at the effect of wave velocity and viscosity at different microcavity depths for 40-90% glycerin content. For very shallow microcavities, characteristics that are more linear but with lower sensitivity are observed.

Despite the complexity of the resonance condition, a close to linear phase relation exists between 40% and 90% glycerin per glycerin content for microcavity depths between 2 μm and 12 μm as shown in Figure 3.13(b). Referring back to Figure 2.5, this translates to a very large change in viscosity and more linear changes in wave velocity and density. Considering that viscosity varies exponentially with glycerin content, this means that the system operates even for very large variations in viscosity. The largest phase shift range is found for the cavity depth of 8 μm, the linear fitting for which yields -0.77 °/(% glycerin) with $R^2 > 0.94$. Sensitivities for 2 μm and 4 μm deep cavities are -0.39 and -0.52 °/(% glycerin), respectively, both with $R^2 > 0.95$.

The resonance condition is very much dependent on the geometry. The liquid will fill in most microcavity shapes completely; however, the shape of the microcavity itself might not be a perfect rectangle as depicted in the simulations discussed so far. It is assumed that the microcavities would be etched by reactive ion etching (RIE) or a similar process, which might incorporate a certain degree of anisotropy instead of perfectly flat sidewalls. That is, the initially assumed perfect sidewall angle of 90 degrees will vary depending on the process. Sidewall angle can be quantified with a dimensionless anisotropy parameter defined as $\alpha = d_l/d_v$ where d_l is the lateral etch distance or undercut and d_v is the vertical etch distance or depth, and where $\alpha = 0$ gives rectangular or perfectly anisotropic etch profile. The effect of the anisotropy in microcavity formation lends itself to a total difference of less than 2 degrees for anisotropy parameters up to 0.05, and 4 degrees up to larger anisotropy parameters around

0.1, for both undercut and overcut type etches, for a depth of 8 μm as shown Figure 3.15. Although the sidewall angles are important for the resonance condition, the process can be carefully optimized for anisotropy before device fabrication. Also, even in the case of slightly angled sidewalls, the same device used for different liquids will offset and cancel out the effect of geometry.
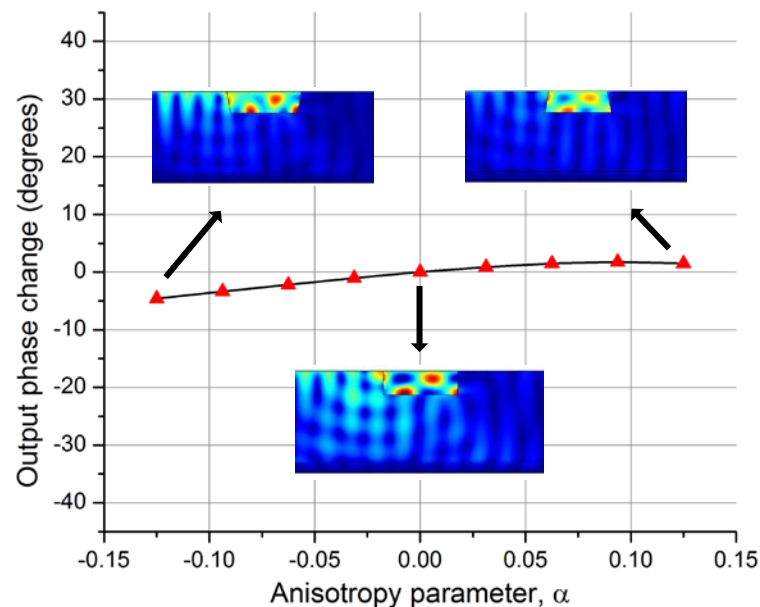
Figure 3.15. Effect of sidewall angle on phase for 8 μm deep microcavities. Anisotropy parameter, α, is defined as the ratio of undercut to etch depth.

3.7. Microparticle Detection

In order to test the system response to sensing and differentiating between solids, the method of application should first be identified. In order to be able to measure different samples with a given sensor and make the SAW sensor reusable for future tests, the sample should be removable from the microcavity easily. A natural choice at this point is polystyrene microbeads with properties listed in Table 3.2.

Table 3.2. Properties of polystyrene microbeads.

Density (kg/m3)	Elastic Modulus (GPa)	Poisson's Ratio
1050	2.9-3.6	0.35

The main difference between the solid polystyrene and the liquid solution is the wave modes they can support. The liquid supports only longitudinal wave modes whereas solid media support longitudinal and shear waves in addition to others such as Rayleigh modes. The propagation characteristics depend on factors including material properties, the nature of excitation, and angle of incidence. Complicating this sensing scheme further, polystyrene microbeads come in a spherical shape not perfectly capable of filling microcavities. In order to enable coupling between the substrate and microbeads, the microbeads are placed in a liquid with known properties, a 90% glycerin-water mixture. The liquid acts as a coupling medium and provides transmission of the SAWs.

A representative displacement map with the microcavity and crystal direction as well as the simulation mesh is given in Figure 3.16(a-b). The simulation mesh and other parameters for the simulation are similar to those given in Table 3.4 except for the microcavity dimensions. The surface waves in the substrate travel along the boundaries of the microcavity and excite ultrasound waves inside the liquid. There is no displacement at the top surface of the liquid domain following from the same idea as with glycerin concentration sensing. The ultrasound resonance inside the microcavity is evident in cross sectional views of

the simulations as shown in Figure 3.16(c-d). The wave motion is transferred to the microbead and back to the liquid domain.
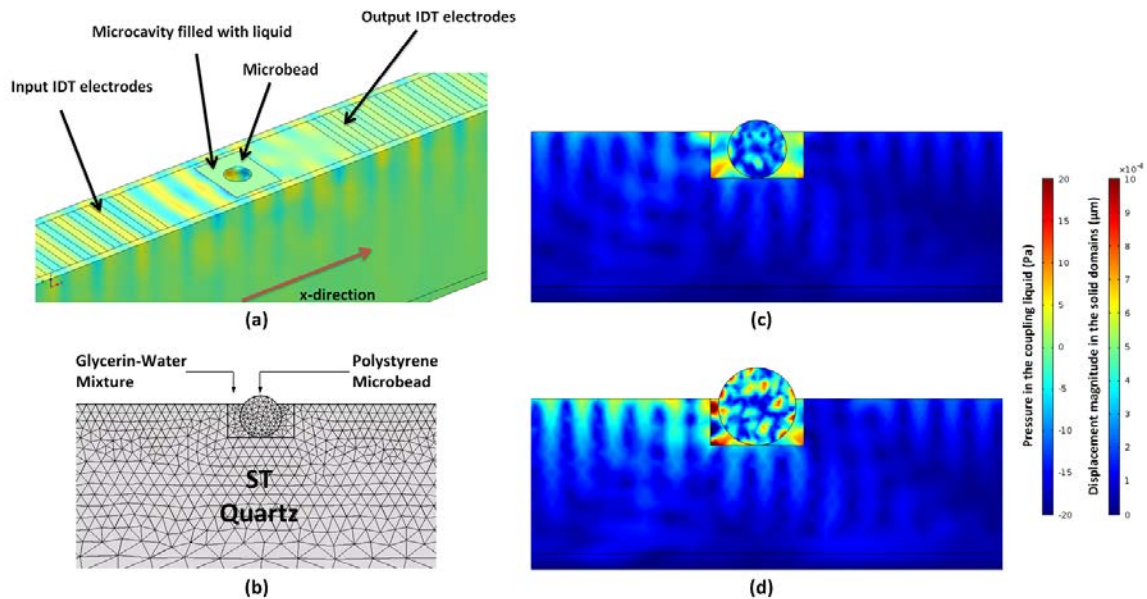
Figure 3.16. (a) Representative displacement map of the system in 3D. (b) Simulation model cross section with the mesh. The total number of mesh elements and other simulation parameters can be obtained from Section 3.8 except the microcavity dimensions. (c) Displacement map inside the cross section of the microcavity for a 10 μm microbead inside an 8 μm deep microcavity. (d) The same case but for a 15 μm microbead. The color bars apply to (c) and (d).

As the path traveled by the acoustic waves is extended due to the presence of a microbead, a delayed component of the wave occurs. On the other hand, smaller sizes of solids do not significantly change the speed or the intensity of the wave inside the liquid. The results imply increased phase shifts as a function of microbead size as shown in Figure 3.17. The expected phase shifts are in the order of degrees, which should be measurable without extensive noise from the experimental sources.
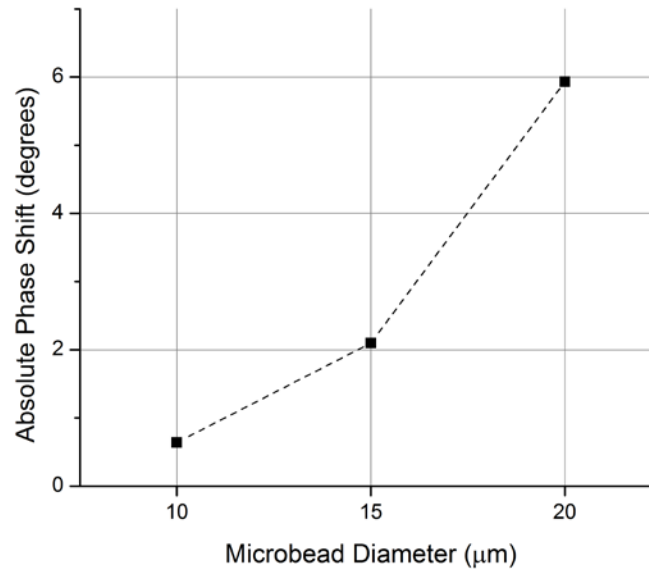
Figure 3.17. Simulation results showing absolute phase shift vs microbead diameter in a 12 µm deep microcavity.

Another possibility is to use this platform for counting particles. For this purpose, microcavities with widths as large as aperture widths were considered. The polystyrene microbeads were placed in a single line order so that they do not significantly interfere with the wave interactions of each other along the propagation path from the input IDT to the output IDT. The same domains and physics were used for this set of simulations whereas the number of microbeads inside the microcavity is varied as shown in Figure 3.18(a) in 3D models of the system. Simulation results for varying number of microbeads are given in Figure 3.18(b). It was seen that decreasing the microcavity depth allows for higher sensitivity for 10 µm microbeads. However, under these conditions, the 5 µm microbeads still provide a challenge in experiments for two reasons. Primarily, smaller microbeads have more space to relocate in the sensing volume, thus

might give rise to ambiguous readings. Secondarily, since the sensitivity is low, it can be difficult to distinguish data from noise in measurements.
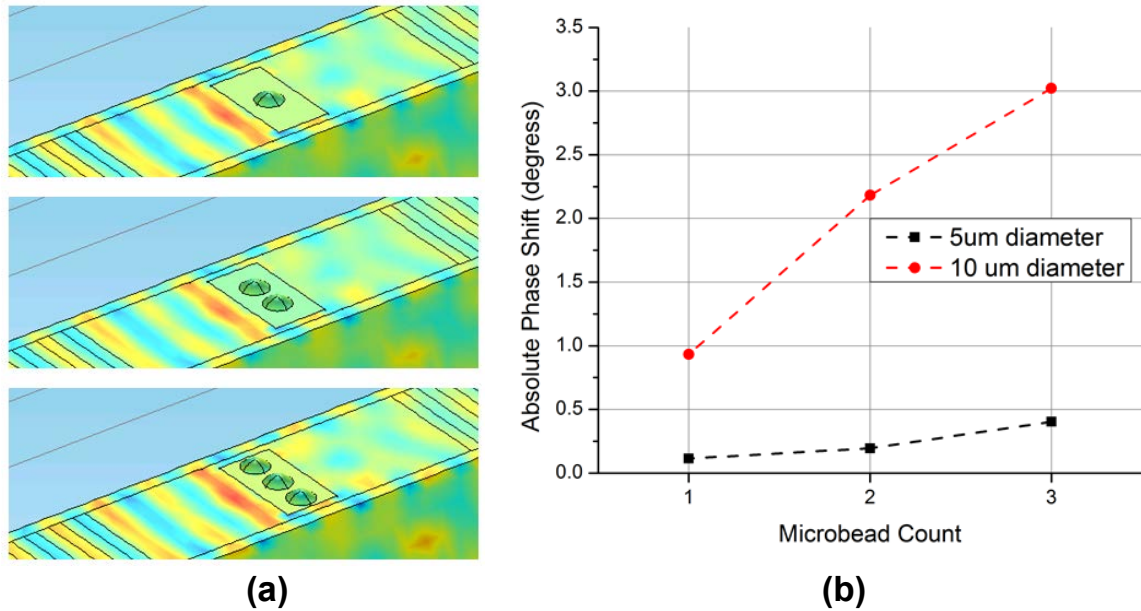
Figure 3.18. (a) Varying number of identical microbeads used for simulations. (b) Simulation results for counting microbeads. The 5 μm diameter microbeads are placed in 32 μm × 16 μm × 4 μm microcavities whereas and 32 μm × 16 μm × 4 μm are used for 10 μm microbeads.

Although the sensing mechanism of the proposed system relies on the mechanical interaction between the sample and the substrate, acoustoelectric coupling still has the potential to adversely affect the output. To estimate this effect on the output, finite element simulations were run. For these studies, the conductivity and dielectric permittivity of polystyrene microbeads and of glycerin solution as a function of concentration were taken from literature [111, 112]. The results show the maximum phase change over the passband to be less than ±0.06° where microbead size is varied from 5 μm to 20 μm. Therefore, the mechanical effects dominate the output and the effect of acoustoelectric coupling

is minimal. This is an expected result from a quartz substrate, since the electromechanical coupling coefficient of quartz is quite small in comparison to substrates such as lithium niobate [113].

3.8. Biological Cell Detection

Biological cells were modeled according to the studies given in section 2.6. Therefore, the biological cells cannot sustain shear waves in them but have elasticities (or bulk moduli) according to the expressions (34) and (35). Consequently, the bulk modulus (or equivalently, elasticity modulus, or stiffness modulus) will be given by:

$$E \approx \rho_0 v_u^2 \tag{37}$$

which is the main parameter measured. It should be noted that multiple combinations of density and velocity can result in the same modulus, i.e. the stiffness moduli are not unique. Elasticities for 900-1100 kg/m^3 samples with ultrasound velocities of 1450-1700 m/s are given in Table 3.3 to provide a guide.

Table 3.3. Realizable elasticity values for cells.

Ultrasound Velocity (m/s)	$\rho_0 = 950$ kg/m^3	$\rho_0 = 975$ kg/m^3	$\rho_0 = 1000$ kg/m^3	$\rho_0 = 1025$ kg/m^3	$\rho_0 = 1050$ kg/m^3
1450	1.997 GPa	2.050 GPa	2.103 GPa	2.155 GPa	2.208 GPa
1500	2.138 GPa	2.194 GPa	2.250 GPa	2.306 GPa	2.363 GPa
1550	2.282 GPa	2.342 GPa	2.403 GPa	2.463 GPa	2.523 GPa
1600	2.432 GPa	2.496 GPa	2.560 GPa	2.624 GPa	2.688 GPa
1650	2.586 GPa	2.654 GPa	2.723 GPa	2.791 GPa	2.859 GPa
1700	2.746 GPa	2.818 GPa	2.890 GPa	2.962 GPa	3.035 GPa

The simulation models prepared in three dimensions consist of approximately 100,000 tetrahedral elements with approximately 1,200,000 degrees of freedom. Due to the low electromechanical coupling coefficient of quartz and requirement for a small aperture, 64 electrode pairs were used for both input and output IDTs. The wavelength of the device is 16 µm, and thickness of the model was set to 80 µm with geometrically increasing element size with distance from the surface to capture the most detail in the surface wave. The highest element detail is attained at the surface and around the microcavity. The finite element model used is shown in Figure 3.19, and the simulation parameters are given in Table 3.4. Similar to the previous results, phase data shows correlation with ultrasound velocity and density; however, the correlation is strong for ultrasound velocity and weak for density when shallow microcavity depths are selected.
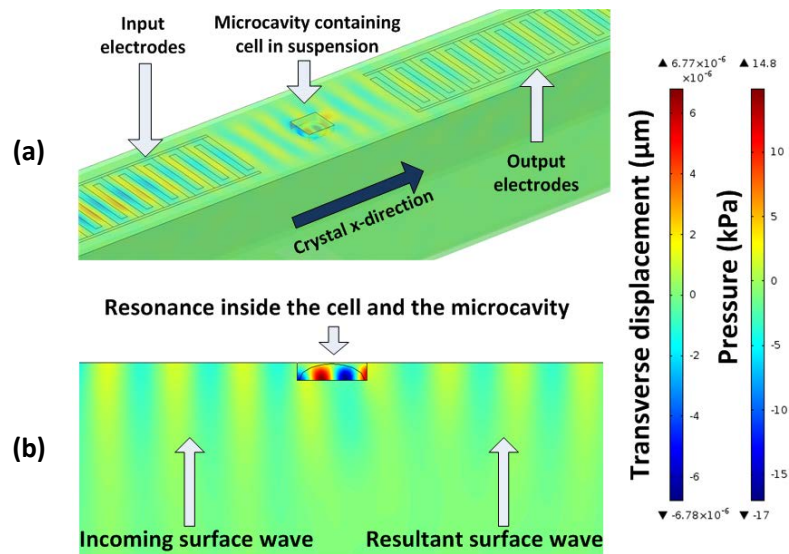
Figure 3.19. (a) 3D simulation model. (b) Cross sectional image from the center axis of microcavity. The top of the microcavity shows no pressure since it is in contact with air. The displacement color map applies to the

piezoelectric material while the pressure map refers to inside of the microcavity in both parts of the figure.

Table 3.4. Finite element simulation 3D model parameters.

Substrate	Quartz (ST-X)	Wavelength (λ)	16 μm
Electrode pairs	64	Microcavity width/length	λ
Electrode width/spacing	4 μm/4 μm	Microcavity depth	0.25λ
IDT separation	6λ	Mesh Elements	~100,000 (tetrahedral)
Depth	4λ	Degrees of freedom	~1,200,000
Aperture	1.5λ	Shape Function Order	Quartic
Cell/Microcavity Volume	0.94 pL/1.02 pL	Cell viscosity	3–5 mPa·s
Cell density	980–1020 kg/m^3	Cell ultrasound velocity	1480–1650 m/s

It was assumed that the cells occupy most of the space inside microcavities so that the interaction in the microcavity is mostly with cells. The rest of the space is occupied by HBSS/5% glycerin solution. SEM investigation shows that cells tend to conform to the shape of sample microcavities as shown in Figure 3.20. Scanning electron microscope (SEM) images of cells in Figure 3.20(b) are used in FEA studies for accurate modeling of cells.

(a)   (b)
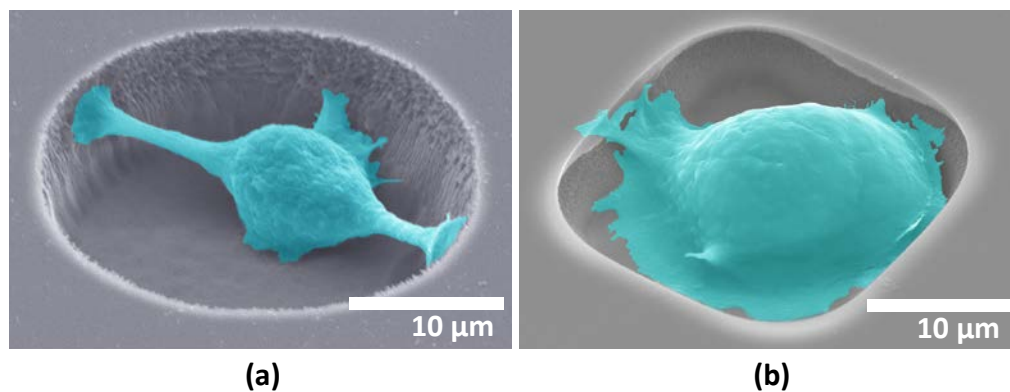
Figure 3.20. MCF-7 cells in (a) a circular microcavity and (b) a rectangular microcavity which is of the used in biological cell studies.

Previously, it was seen in the simulations and measurements glycerin content in liquids that phase angle provides an appropriate way of reading out material properties in the form of delays introduced to the wave being transmitted to the output. The viscosity, in contrast to previous observations with high viscosity liquids, is not a good indicator. This is because the observed viscosity from cell to cell is expected to vary by only a small amount of less than about 5 mPa-s according to acoustic microscopy studies. The platform is not capable of responding to such small viscosity changes as found in the FEA studies. Then, difference in the proposed system for cell detection is that the viscosities of cells are not the main parameter.

The main parameter of importance is the ultrasound velocity. The ultrasound velocity changes the angle of incidence of the ultrasound wave emitted into the microcavity, directly affecting the phase of the output. The density also has a small effect as the changes in the acoustic impedance alter the amount of acoustic energy transferred to the liquid domain. However, it is observed in the simulations that the variation due to density is much smaller and can be neglected compared to the effect of ultrasound velocity. Figure 3.21 shows the variation in the output phase angle as a function of both density and ultrasound velocity. Therefore, for the models used in this study, the stiffness is mostly a function of ultrasound velocity.
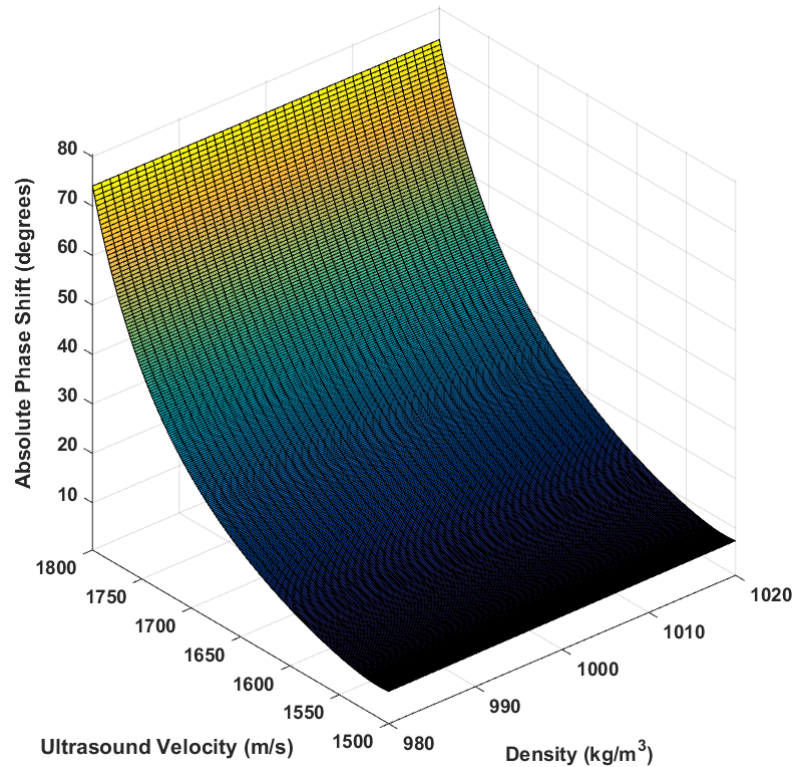
Figure 3.21. Output phase as a function of ultrasound velocity and density which combine to define the stiffness modulus of the cell over a wide range of ultrasound velocities. The data were obtained by a nested study of both variables.

If it is assumed that cell density is the same as the medium, ultrasound velocity is left as the determining factor for the elasticity modulus. In Figure 3.22, the change in the phase shift as a function of ultrasound velocity is shown relative to the medium. The medium in this case is HBSS/5% glycerin solution. Ultimately, the phase shift that occurs as a result of placing the cell in the medium is compared to the case where only the medium is occupying the microcavity. The modulus of the cell can be calculated by working back from the phase shift to the velocity differential and plugging it into equation (37) to find a figure for bulk modulus. The sensitivity increases as the difference between the

ultrasound velocity differential grows. A figure for system sensitivity can be calculated from this figure by curve fitting as roughly 0.05 º/[m/s] or ~0.35 º/MPa for the region of interest. These results were obtained at microcavity dimensions of λ × λ × 0.25λ.
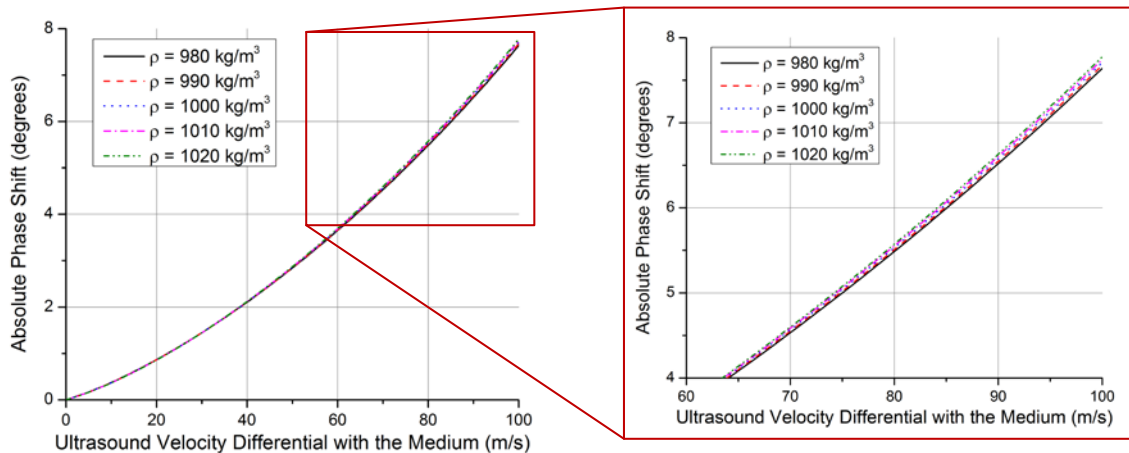
Figure 3.22. Absolute output phase shift as a function of ultrasound velocity differential with the medium. The volume occupied by the cell gives rise to the phase shift depending on the difference of the ultrasound velocity in the cell and the medium. The density has only a marginal effect on the phase and mostly at a high velocity differential with the medium.

3.9. Matching Circuits and Devices

There are numerous constraints that go into designing microcavity coupled SAW devices that differ from those of regular SAW filters. First of all, as it stands, the wavelength is constrained to be comparable to the cell size which brings lithographical process limits into play. Consequently, the aperture of the device is not a parameter that can be freely manipulated to improve the insertion loss characteristics. Instead, the aperture should also be kept comparable to the cell size to increase wave interaction with the cells. It is quite difficult to design apodized electrode geometrized with very small apertures and critical dimension

limits of ±1 µm in lithography processes. Therefore, very straightforward constant overlap and unity metallization patterning of electrodes were selected.

On top of these, the substrate should have a good etch chemistry for microcavities to be formed directly into the substrate. For this last constraint, quartz substrates were generally employed in the studies. Selection of quartz means a high insertion loss and a small bandwidth for the SAW sensor. Neither of these consequences equate to a bad performance as the geometry of the microcavity is the main factor for facilitating the wave interaction.

It was seen that microcavities with large depths such as 8 µm and 12 µm make better devices for cases where viscosity of the liquid solution is to be measured. This is a result of the longer wave path inside the microcavity for exploiting viscosity variation. On the other hand, biological cells with their small viscosity variations work better with small microcavity depths for ultrasound velocity measurements.

In the measurement stage, the combination of the small piezoelectric coupling coefficient of quartz and the small device apertures make it difficult to match the input of the devices to 50 Ω for better insertion loss characteristics while keeping the overall size manageable. In order to improve the insertion loss and the signal to noise ratio, the SAW devices can be integrated with matching circuits. Consequently, a high frequency PCB has been designed to match the input of the SAW devices to 50 Ω and provide a higher performance.

Modeling SAW devices as two port networks can be a primitive practice for extracting device characteristics as well as designs. However, this is a widely used method for matching network design. In such models, the finger pairs on an IDT all have static capacitances between them which can be summed up as a lumped C_t parameter. The resistive losses in the device are modeled with a radiation conductance, G_{rad}, (or equivalently, a radiation resistance) which form the real part of the SAW device input impedance. The radiation conductance at the peak frequency of the filter is given as

$$G_{rad}(f_0) = 8k^2 f_0 N C_t \tag{38}$$

where N is the number of finger pairs, k^2 is the electromechanical coupling coefficient, and f_0 is the peak frequency. There is also an additional parameter, acoustic susceptance, which is used to model acoustic wave phenomena as an electrical parameter and is denoted as B_a. The acoustic susceptance is zero at the synchronous frequency and can be neglected for matching purposes since matching is considered only at the passband of the SAW filter. There are package parasitic elements that need to be accounted for as well as the inductance from wire bonds, L_{wire_bond}. The model should take into account the vector network analyzer (VNA) as a voltage source with its 50 Ω output impedance and the transmission line of matched 50 Ω impedance. The entire model is then given as in Figure 3.23. The purpose of the matching network is to change the input impedance looking into the network so that it matches that of the source, which is 50 Ω.
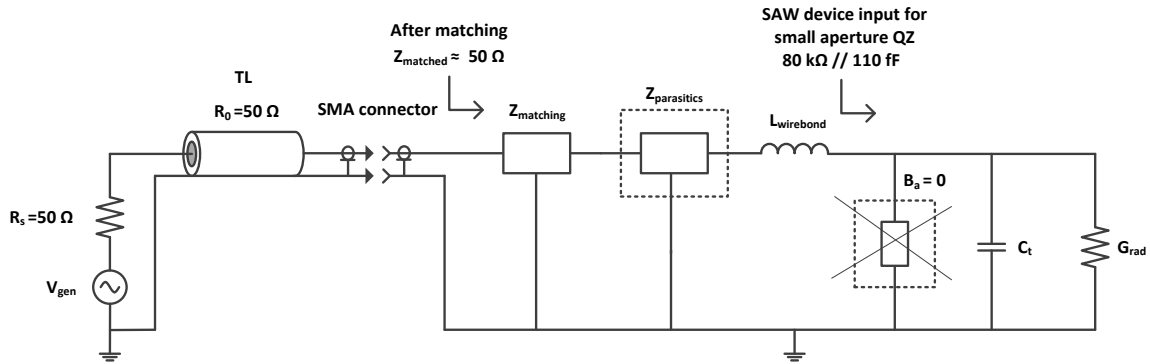
Figure 3.23. Complete model for matching circuit design. Extra components such as parasitics and Lwirebond are not included at the first stage of the design but added later. After they are added, the design is fine tuned.

The values given in Figure 3.23 are for a 64-IDT-pair SAW device on ST-X quartz with an aperture of 30 µm. The topology of the network is dependent on the Q values needed and the impedance of the SAW device. The Q value of the impedance matching network needs to be smaller than the Q of the SAW filter in order not to mask its passband. In the case of a quartz sample as shown in the figure, the resistance is quite large and the capacitance is very small. So the resistive losses will still be considerable and an impractically large inductance might be needed to bypass the C_t. Several different topologies exist to fit this situation as shown in Figure 3.24.

The problem of large inductance can be alleviated (but not entirely solved) by placing the elements so that the bypass inductor for C_t is in parallel with another inductor that is part of the matching network. This way, the two can be combined, and the small inductance will dominate. In the case of very small apertures as the devices used, tapped capacitor transformer is the better solution.

Comparison of various topologies is given below in Table 3.5 for SAW devices on quartz.
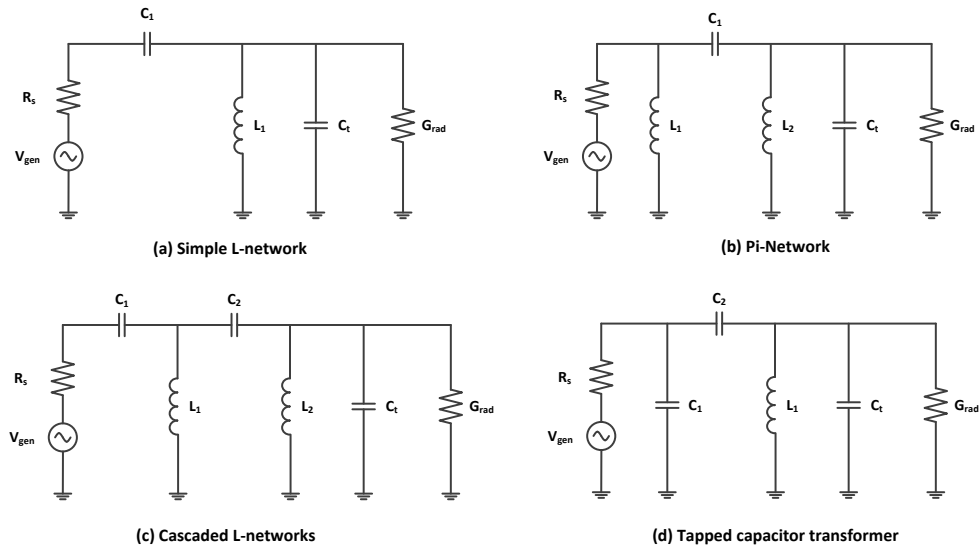
Figure 3.24. Four possible network topologies for matching. The inductor always needs to shunt the internal capacitance of the SAW device. This directly affects the selection of the best topology.

Consequently, a high frequency PCB has been designed on an FR4 substrate with microstrip transmission lines for unbalanced SAW device operation. The microstrip was preferred over suspended stripline and coplanar waveguide due to simplicity and adequate performance as the frequency is much lower than the GHz range. The FR4 thickness is selected as 31 mils. The copper layer thickness is selected as 1.4 mils whereas the trace width is 50 mils. Outer dimensions of the board are 2.60" × 2.80". The PCB as designed is shown in Figure 3.25.

Table 3.5. Comparison of performances of various topologies with the aforementioned SAW device simulated in this chapter on ST-X quartz. The measured actual bandwidth of the device is 1.15 MHz.

Approach	Return Loss	3dB-BW	Components	Flexibility	Parasitics
L-network	-50.5 dB	7.7 MHz	> 1 μH inductors Not realizable	Low	Very high
Pi-network	-74.6 dB	2.6 MHz	Standard value components	Medium	Medium
Cascaded L-networks	-70.1 to -99.2 dB	450 kHz to 2.8 MHz	Requires many components for high performance	High	Medium to high
Tapped capacitor	-60 dB	2.4 MHz	All components are standard values, Few components	High	Low to medium

The design has a metal area in the center to be used for bonding of SAW devices and grounding to prevent electromagnetic interference. Up to three SAW device pairs can be matched and operated at the same whereas several other ports are available for calibration and testing purposes for SMD components, vias, and transmission lines. The SMD component solder pads accommodate the 0402 package. On the four corners, there are mounting holes for fixing the board into the housing that will be shown in the next chapter. The PCB also contains a reserved DC section for future use separate from the RF section.
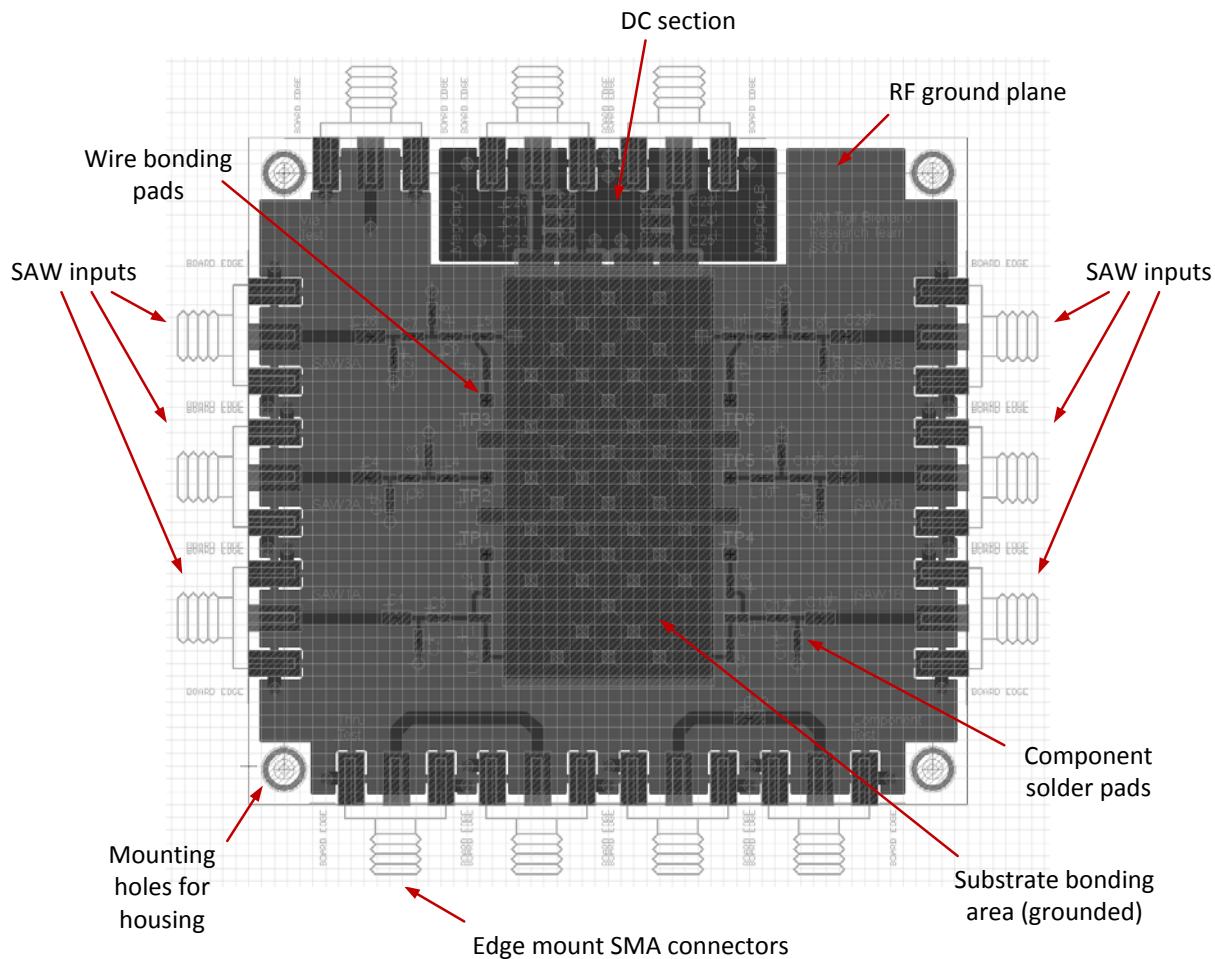
Figure 3.25. High frequency PCB for testing SAW devices.

CHAPTER 4: MICROFABRICATION

The microfabrication of the devices was carried out at a class 100 cleanroom. Microcavity coupled SAW sensor process requires two major steps, namely, IDT patterning and microcavity formation, along with an optional step of microfluidic integration. This chapter deals with the photomasks designed for the process, fabrication flow of the samples, optimization of the process steps, and metrology studies regarding the process.

4.1. Photomask Design

The SAW microdevices have been fabricated with the help of photomasks as opposed to direct laser writing due to cost and throughput considerations. Three different photomask sets were prepared for this purpose for different purposes. A successfully fabricated photomask belonging to *Photomask_set_2* is shown in Figure 4.1.

(a)	(b)
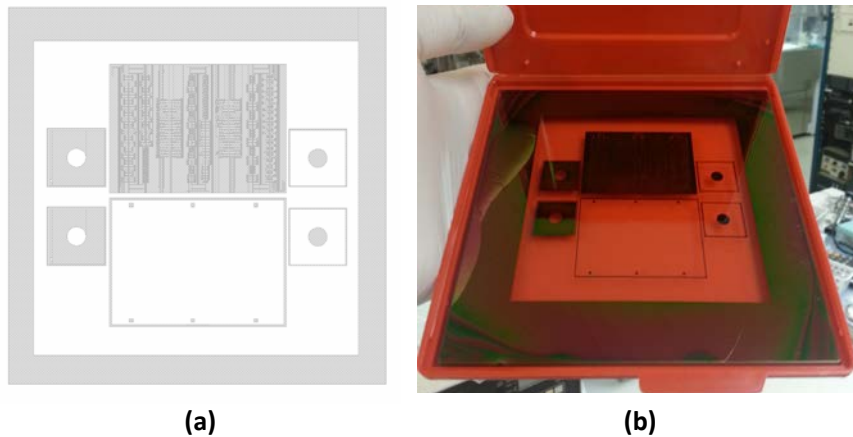
Figure 4.1. Photomask_set_2 designed for the process. (a) The design file. (b) Mask fabricated on 5" soda lime glass photomask plate.

Photomask_set_1 was designed with the intention of identifying viable substrates for SAW generation. These devices were used as proof of concept for several substrates including lithium niobate (LiNbO$_3$), lead zirconium titanate (PZT), polyvinylidene fluoride (PVDF), poly[(vinylidenefluoride-co-trifluoroethylene] (PVDF-TrFE), and zinc oxide (ZnO) in addition to quartz (SiO$_2$). The aperture sizes of these devices are the largest to ascertain wave generation and low insertion loss parameters.

Photomask_set_2 was designed with the highest number of devices on it to attain high throughput for testing on quartz substrates. All devices have a large number of IDT pairs (64) due to the piezoelectric coupling coefficient of quartz. This mask also houses devices that are orthogonal to the Rayleigh wave propagation axis on quartz to excite SH-waves, specifically SSBW on quartz rotated ST 90º-cut. This set contains the most varying types of microcavities as well.

Photomask_set_3 contains varying numbers of IDT pairs on various devices as well as different wavelengths. This mask contains devices compatible with some microfluidic designs. These designs accommodate reservoirs for entry and exit ports of the liquid and do not cause loading on the IDT electrodes due to the specific design of the microchannel and the elongated busbars of the IDT devices.

Photomask_set_4 contains various IDTs designed for use on Y-Z lithium niobate. These devices utilize surface microcavities instead of etched substrate

type microcavities. In addition to the fixed aperture devices same as on other masks, this mask set also contains focused IDT designs and pseudo-chirped IDTs for future use (not detailed in this dissertation). One mask on this set is designed for microchannel molding, with a matching 3D-printed microchannel size template. The microchannels are to be used with pseudo-chirped IDTs, and both are designed in a similar manner to Photomask_set_3 to prevent mass loading.

All photomasks are compatible with ground-signal (GS) and ground-signal-ground (GSG) type RF measurement probes as well as probe pitches from 50 µm to 125 µm. All masks also house a large amount of extra microcavities to work on dispensation studies as well as structures compatible with stylus based surface profiler to measure microcavity depth. The fourth mask set also contains some large solder pads for wire soldering for accessibility at the expense of added capacitance.

4.2. Microfabrication Flow

As stated before, the microfabrication consists of two major steps with an optional step of microfluidic integration. The major steps are microcavity etching and IDT electrode formation. The microfabrication flow is given in Figure 4.2. Prior to actual microfabrication the steps, substrates underwent a cleaning process. This step consisted of acetone cleaning to remove organic impurities on the surface followed by isopropyl alcohol (IPA) spraying and deionized water (DIW) spraying. Acetone application was carried out inside a 20 kHz commercially available ultrasonic bath at 50ºC to provide agitation.
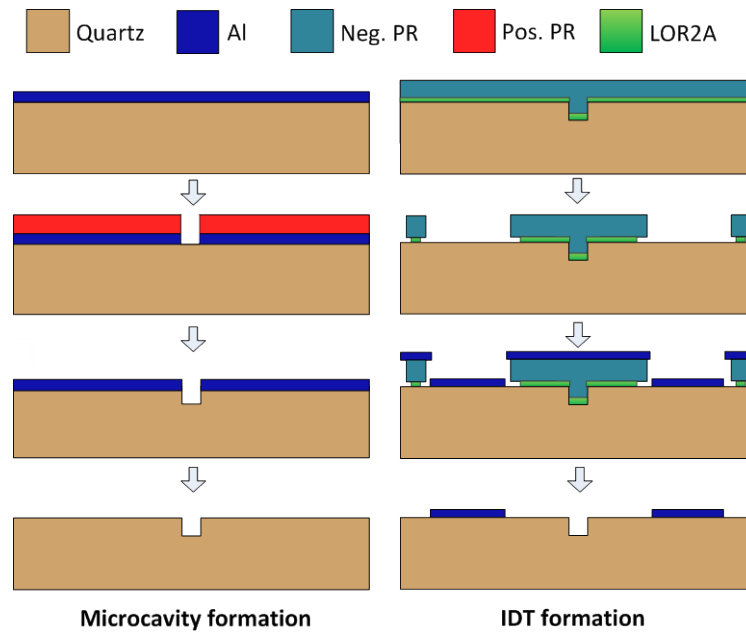
Figure 4.2. Overview of the microfabrication flow.

4.3. Process Steps and Optimization

Each process step was optimized separately as detailed in the upcoming sections. These processes include etching the microcavity, SAW device IDT electrode patterning, microfluidic channels, and SU-8 soft microprobes as well as 3D printed housing and ancillaries.

4.3.1. Microcavity Etching

Microcavity etching is an important step that is integral to the success of the proof of concept and there are two important points to consider in this process: the fidelity (and reproducibility) of dimensions, and preventing damage to surface during the etching process. The former becomes of importance as microcavity dimensions related to the wavelength of the SAW device dictates the interaction of the SAW and the sample in the microcavity. The latter matters as the SAW can get adversely affected due to surface defects.

The first concepts were prepared on silicon substrates with RIE processes to utilize ZnO thin films deposited on top of silicon as the piezoelectric material. For silicon, it is usually enough to mask the etch process with photoresist to easily obtain high aspect ratio vertical etch profiles in the 10-20 µm etch depth range as shown in Figure 4.3 (a). However, due to problems with ZnO processes, the concept had to be migrated to other materials.

The second generation of microcavities was prepared on lithium niobate and quartz. It is well known that lithium niobate is a very hard material to etch without mechanical methods. Lithium niobate's etching characteristics depend on the orientation of the crystal although it is always very slow (<200 nm/hr) with RIE [114, 115]. Wet etching with chemicals has been reported to work under some specific conditions but these methods usually include interactions with proton exchange membranes to alter the surface [116]. This is detrimental to the surface integrity and is not preferred for the SAW devices in this study for obvious reasons. Despite these difficulties, lithium niobate was still utilized with very shallow microcavities in the range of 1.0-1.2 µm as shown in Figure 4.3(b).
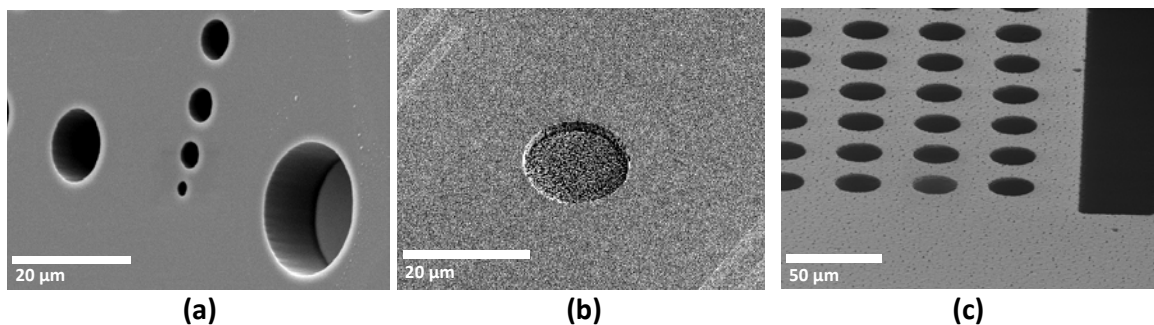
Figure 4.3. Initial microcavity etching results in (a) silicon, (b) quartz, and (c) lithium niobate.

Quartz is a material with relatively well-known etch characteristics in both wet and dry processes. Wet etching is possible with diluted hydrofluoric acid (HF) but dry etching with RIE was preferred to attain higher process control. The only issue at this point is the low selectivity of photoresist which caused it to completely get etched away in less than 20 minutes of RIE treatment. Therefore, the samples with Cr and Al were tested as hard mask materials. Cr selectivity is lower than Al for the CF_4 based recipe being used, so Al is preferred. The deposition of the hard mask Al layer was carried out with an e-beam evaporator over 6 minutes of processing time to a thickness of 0.8-1.0 μm on all samples. Lithography of this layer was carried out with AZ5214E type photoresist in positive mode. Etching was completed in 8 minutes at room temperature with commercially available aluminum etchant type-A from Transene company. The details of this process are given in Table 4.1.

The process recipe is given in Table 4.1 and the evolution of etch depth is given in Figure 4.4 as measured by a stylus-based surface profiler. The process was carried out in intermittent steps of 30 minutes to prevent overheating. Due to spatial non-uniformity of the plasma, the sample was rotated by 180 degrees at every subsequent step. The etch depth uniformity obtained from samples are shown in Figure 4.15. After formation of microcavities, the masking Al layer was removed by submerging in the same wet etchant for 16 minutes. There were no visible signs of damage on the substrate surfaces with an optical microscope.

Table 4.1. Etch recipe for quartz in RIE.

Power	Process Gases	Gas Flow Ratio	Pressure	Etch Rate
300 W	CF_4/O_2	4:1	170 mT	~130 nm/min
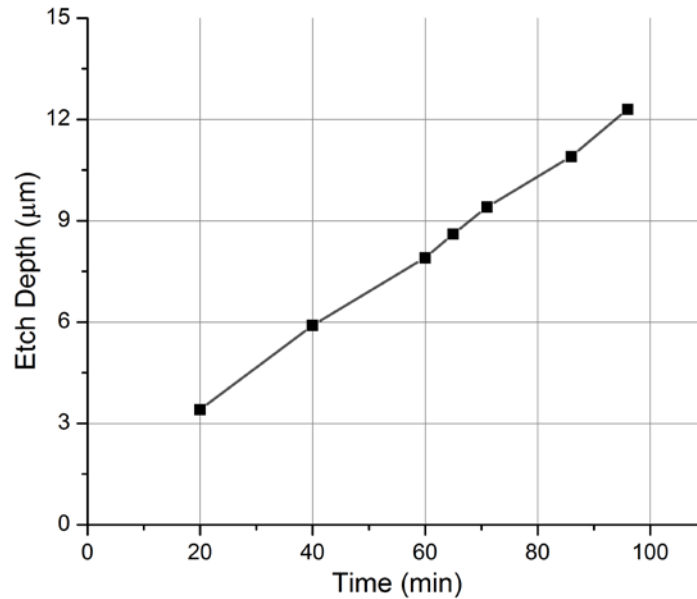
Figure 4.4. Quartz dry etch depth study.

The microcavity bottom surfaces were treated with both SF6 plasma and concentrated BHF on separate samples in order to reduce surface roughness of 0.5 μm after the RIE process. The SF6 method resulted in no significant change in surface roughness whereas BHF solution was seen to be more effective. After treatment in this solution for 30 minutes, the resultant average roughness was measured with an AFM as shown in Figure 4.5 and found to be approximately 0.35 μm which is much smaller than the wavelength of 16 μm.
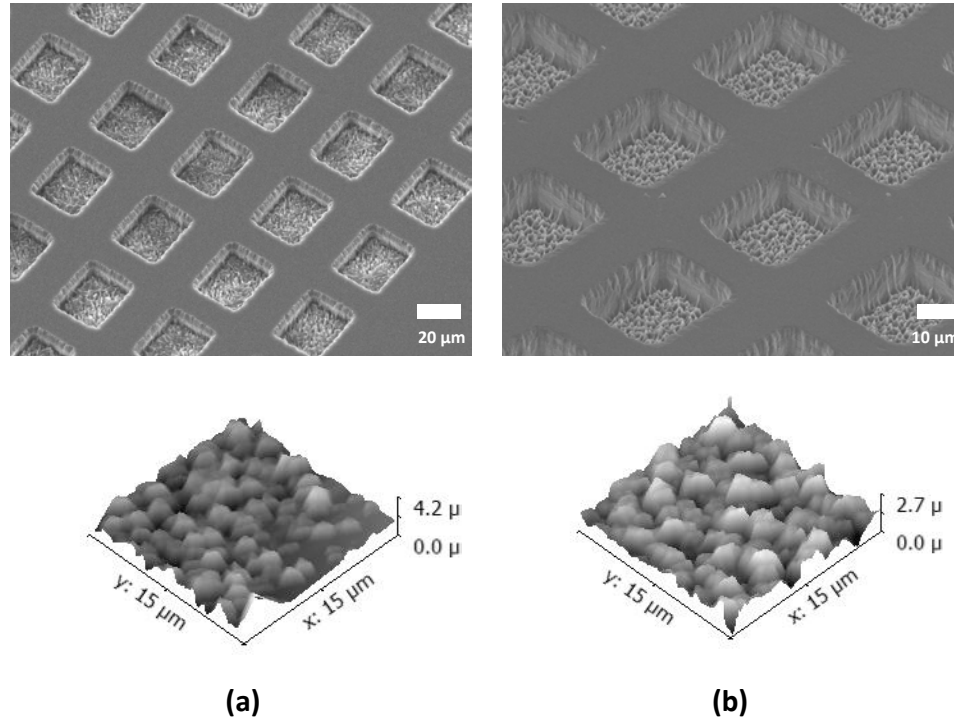
Figure 4.5. (a) Microcavity bottom profile after RIE (R_q = ~0.5 µm). Some residues and sharper surface roughness showing. (b) Microcavity bottom profile after 30 minute BHF:HCl:IPA treatment (R_q = ~0.35 µm).

4.3.2. Electrode Formation

IDT electrodes have been fabricated using aluminum as the metal layer due to similarity of acoustic impedance of aluminum films to that of piezoelectric substrates to minimize reflections. The electrode formation has been preferred as the second step of the process after microcavities as the same metal layer is used for masking of the other step as well. In order to prevent undercutting in this process, electrodes have been formed with the lift-off process. The optimization effort for this process has largely been spent towards the sidewall profile of the photoresist. Negative photoresists are usually associated with lift-off processes due to their negative sidewall angles. In this process, the same photoresist, AZ5214E, has been utilized in negative mode to obtain an inverted frustum-like

shape. Upon further optimization, it became clear that special lift-off photoresists help tremendously with creating discontinuities in the photoresist profile, so LOR2A was incorporated into the process as schematically shown in Figure 4.2. In the microfabrication flow of the devices of the fourth mask set, only one layer of photoresist, nLOF 2020, is used. nLOF is a negative photoresist with excellent undercut properties suited for lift-off processes. It also requires no image reversal or hard bake steps. Parameters for lithography process are shown in Table 4.2.

Table 4.2 Parameters of the lithography processes in the electrode formation step. The first values for baking and exposure processes for AZ5214E are the ones after spinning and the second ones are for image reversal.

Process	Material	Spin Speed (rpm)	Spin Time (sec)	Bake Temp. (ºC)	Bake Time (sec)	Exposure Dose (mJ/cm^2)	Development type and duration
Process 1	HMDS	5000	30	110	60	-	-
	LOR2A	2500	45	150	120	-	-
	AZ5214E	5000	45	110/120	50/80	18/180	MF-26A, 35 sec
Process 2	nLOF 2020	4000	45	110/110	60/60	65/-	AZ MIF 300, 35 sec

After the lithography process was completed, the samples in Process 1 were hard baked at 120 ºC for 20 minutes to prevent outgassing in vacuum environment required for thin film deposition. Process 2 with nLOF 2020 does not require a hard bake step. The deposition was carried out using an e-beam evaporator to obtain a discontinuous film over the photoresist profile as shown in

Figure 4.6(a). The last step of the process was to lift the photoresist off to remove unwanted metal lines. Remover-pg, a commercially available solvent from Microchem was used for this purpose. The samples were dipped in remover-pg and soaked for 2 hours followed by ultrasonication for 5 minutes. Samples were then moved to a fresh solution to prevent the removed film from sticking on the surface and soaked for 1 hour followed by 5 minutes of ultrasonic bath. The samples were then removed from the solution, cleaned with DIW, and dried with a nitrogen gun. Successfully formed IDTs from process 1 are shown in Figure 4.6(b). Measurements of film thickness are given in metrology studies at the end of the chapter.

(a)   (b)
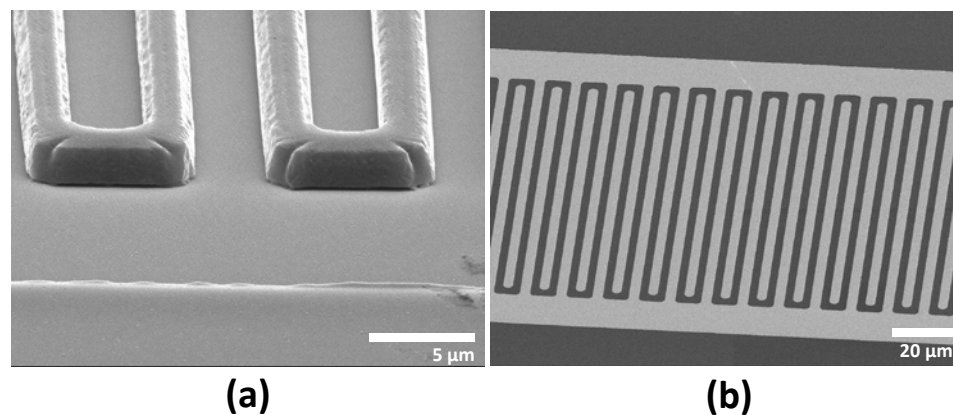
Figure 4.6. (a) Metal on patterned photoresist according to Process one. (b) Metal IDTs after lift-off.

4.3.3. Integration with Microfluidics and Housing

Integrating the system with microfluidics is an optional step and has been accomplished with the intention to prove its viability for future work. The microfluidic channels are fabricated by molding SU-8 samples with

polydimethylsiloxane (PDMS) which is a well-known biocompatible polymer used for microchannels. The fabrication process is shown in Figure 4.7.
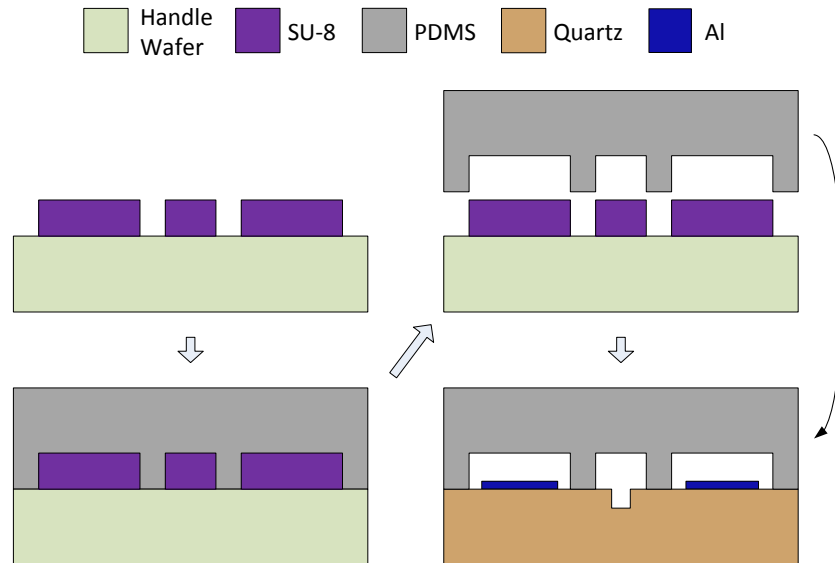
Figure 4.7. Microchannel fabrication flow and integration with SAW devices.

The molds are created by exposing SU-8 2025, a negative mode, epoxy based, permanent type of photoresist which is almost impossible to remove chemically, on a silicon or glass substrate. After hardbaking and silanizing, an ABS plastic template 3D printed to accommodate the outline of PDMS microchannel slab is placed on the SU-8 coated substrate. The template is necessary to precisely define the lateral dimensions as well as the height of the PDMS slab. The slabs used in the study were approximately 14 mm × 36 mm with a height of 5 mm. Once this template is fixed to the substrate with binder clips, individual microchannel shapes are covered with the PDMS solution and left to cure overnight as shown in Figure 4.8(a). Although it is possible to expedite this process by baking the PDMS, it was found that the overnight

process provides better results in clean removal of PDMS from the mold and the template. After removal, the reservoirs at the end of the microchannel are punched with surgical punches of 1.5 mm diameter to create the inlet and outlet ports for the fluid flow. Following this, individual PDMS slabs are loaded onto a spring loaded alignment apparatus. This apparatus helps keep the slab steady in place and is installed on a probe station. Using the integrated microscope, this system is used for precise alignment and bonding of the microchannels by using the positional control of the stage and the height control of the platen. The microchannel is bonded simply by contact and minimal pressure is applied. This kind of bonding was seen to be strong enough for many microfluidic operations especially involving negative pressures.

(a)   (b)
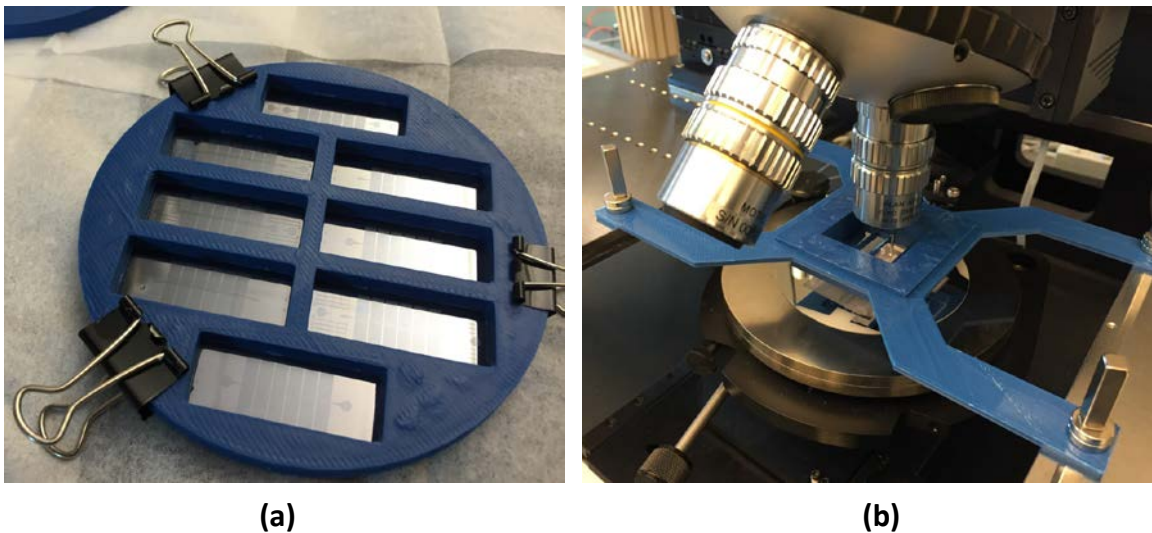
Figure 4.8. (a) Preparation of the microchannels in desired dimensions with a 4"-diameter 3D printed template on a 4" substrate. (b) 3D printed alignment apparatus installed on probe station for precise microchannel bonding.

If a stronger and more stable bond is desired between PDMS and the substrate there is an alternative process that was developed in [117]. In this method, PDMS can be spin coated to a thin layer on a disposable substrate. This layer is then transferred onto the PDMS slab by contact in order to be used as glue for microchannel. Once this microchannel is situated on top of the desired substrate, it is left to cure overnight as in the first step, forming a cured bond between the microchannel and the substrate. Microscope images of PDMS microchannels aligned and contact bonded to substrates are given in Figure 4.9.

(a)   **(b)**
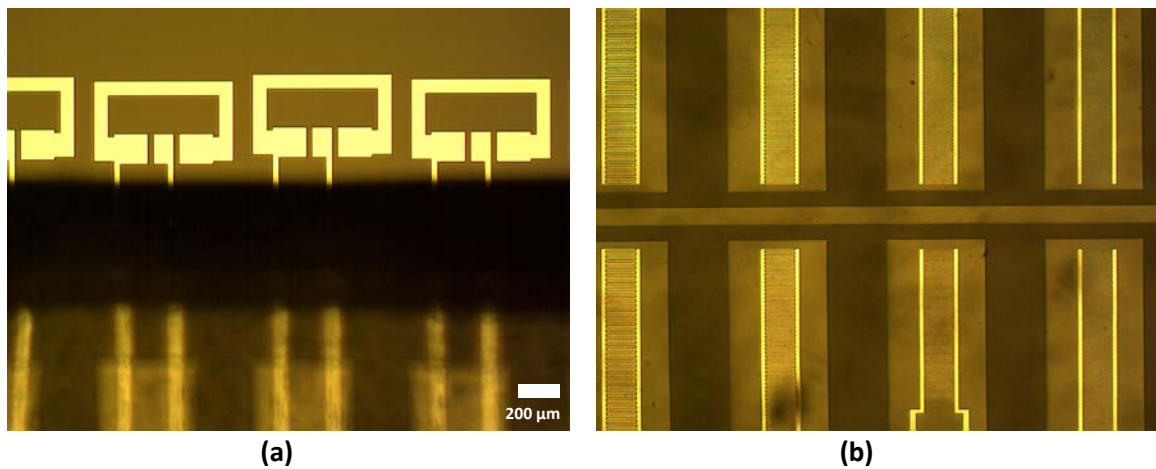
Figure 4.9. Microscope images of PDMS bonded to a substrate (a) at the edge of the PDMS slab and (b) near the microchannel region. Electrical access to device pads is unobstructed. The microchannel is designed and aligned to avoid mass loading the SAW device IDT electrodes. The scale bar applies to both images.

In order to serve as housing, a plastic box was made using a 3D printer out of ABS plastic. The box consists of a base that uses spacers for mounting and screwing in the circuit board designed as shown in Section 3.9, and a lid that incorporates a microscope slide to serve as a viewport. The housing box provides access to all inputs on the PCB through SMA connections as well as

microfluidic tubing for microchannels. Interior of the housing can be lined with aluminum foil to obtain a simple Faraday cage. The housing box is shown in Figure 4.10.

(a)   (b)
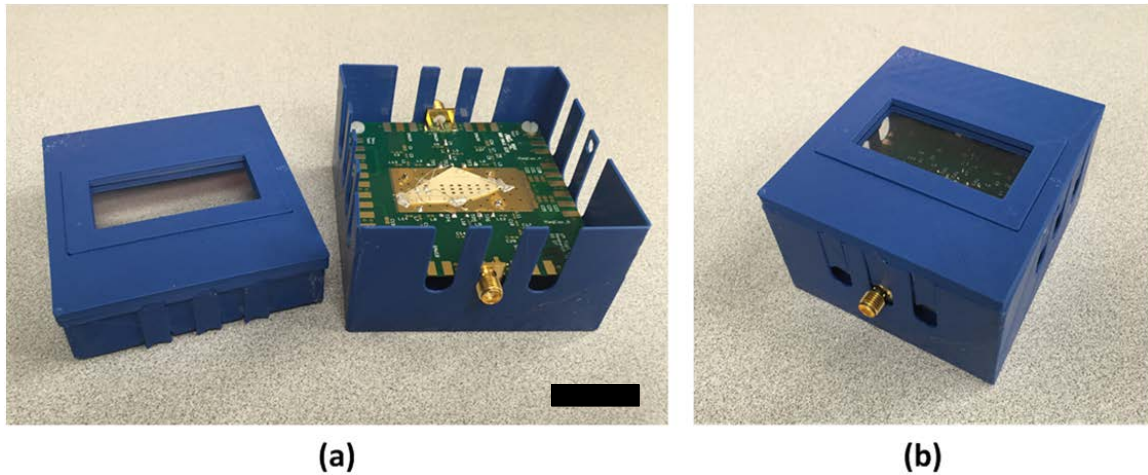
Figure 4.10. (a) The lid and the base made of ABS plastic using a 3D printer. The scale bar is 1 inch. (b) Closed housing box with SMA connections.

4.3.4. Cell Dispensation Microprobes

Dispensation of biological cells into microcavities comes with numerous difficulties if no microchannel is involved. To overcome these issues flexible, fully suspended, biocompatible microprobes were fabricated from SU-8. These microprobes have large bodies so they can be manipulated by hand and have very small sized tips (10-30 µm) to pick up and manipulate cells in cell solution. Some microprobe tip designs are shown in Figure 4.11.

Since they are made of SU-8, the microprobes exert little stress on biological cells so as not to cause lysis or changed cell function and do not crush or puncture them as metal probes do. These microprobes are fabricated as shown schematically in Figure 4.12.
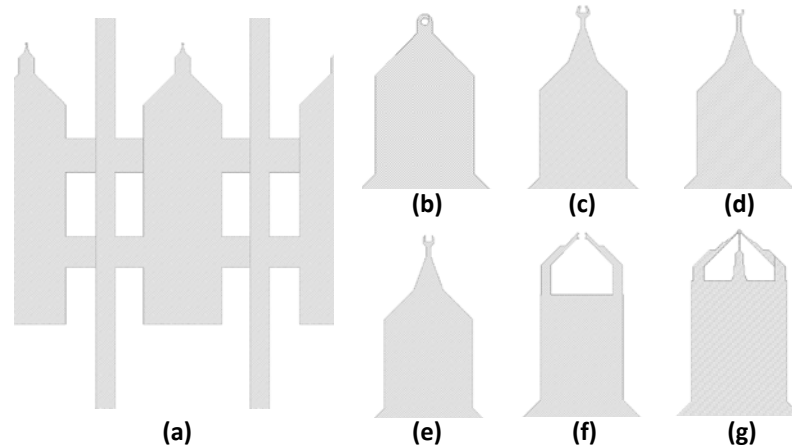
Figure 4.11. Microprobe designs in photomasks. (a) The body of microprobe and (b-g) various tip geometries used in the experiments.
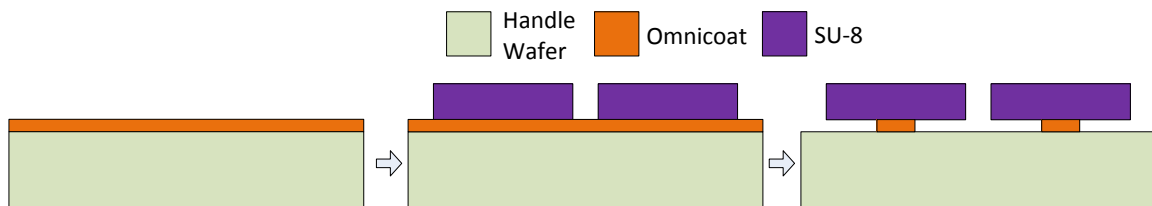
Figure 4.12. Soft microprobe fabrication flow.

A handle wafer, in this case n-type silicon, is spin coated with a chemical known as Omnicoat which has good adhesion properties to substrates and SU-8 type photoresists. The coating thickness is around 50 nm at 2500 rpm spin speed. A bake is required at 200 ºC to stabilize the coating. This process is followed by spinning of SU-8 2005 at spin speeds of around 800-1500 rpm to obtain around 6-10 µm thick films of SU-8. This formulation of SU-8, the 2005, has much lower viscosity than the 2025 variant which makes it easier to make thinner structures and pattern them with lithography. After soft baking, exposure, and post exposure baking, the SU-8 film is developed with regular SU-8 developer for patterning. SU-8 is then hard baked for 5 minutes in a convection oven at 150 ºC.

This step hardens the film and causes reflow to relieve internal stress to prevent cracks occurring on the film. Finally, the handle wafer is dipped in MF-26A developer to controllably undercut the Omnicoat film underneath SU-8. The photomask is designed in a way so that the soft probes are much smaller in size than anchoring lines so they get undercut first. When the SU-8 film is mostly but not completely undercut during visual inspection of MF-26A development, the handle wafer is taken out of the solution and cleaned with DI water carefully. DI water is evaporated using a hotplate to obtain the handle wafer with microprobes on it as given in Figure 4.13(a). Following this, microprobes can be removed easily by scotch tapes.

(a)   (b)
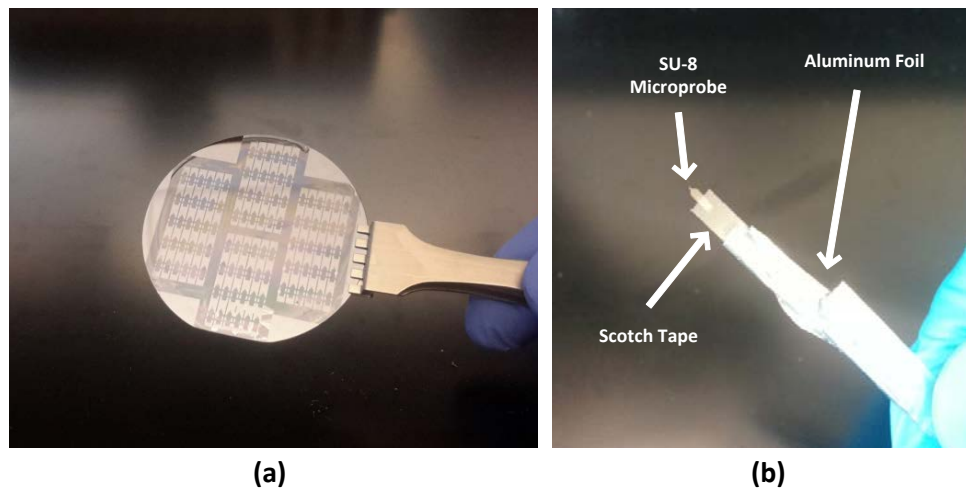
Figure 4.13. (a) Microfabricated SU-8 soft microprobes on 2" diameter handle wafer. (b) SU-8 microprobe ready to use.

These SU-8 microprobes are then attached to 3D printed connector pieces using the same scotch tapes. Chemical treatment of micro-probes to increase their contact angle was seen to be beneficial. In order to improve the holding efficiency of the probes, they were dipped in a 100 mM ethanolamine

solution for 20 minutes at 50°C. This process results in an increased number of surface OH groups on the SU-8 and makes it easier for water molecules to attach [118]. After ethanolamine treatment, microprobes were attached to 3D printed connector pieces made of ABS plastic which are in turn attached to micropositioners. Usage of scotch tape coupled with the low modulus of elasticity (~3 GPa) and thickness (<10 μm) of SU-8 make the microprobes quite soft and therefore non-damaging toward cells. A microprobe after being released from the handle substrate and ethanolamine treatment is shown in Figure 4.13(b).

4.4. Additional Metrology Studies and Completed Devices

This section includes the measurement results that validate the microfabrication efforts in this study. The microcavity dimensions are integral to the success of the study, so depths of microcavities were characterized using a surface profiler with the results given in Figure 4.15(a).
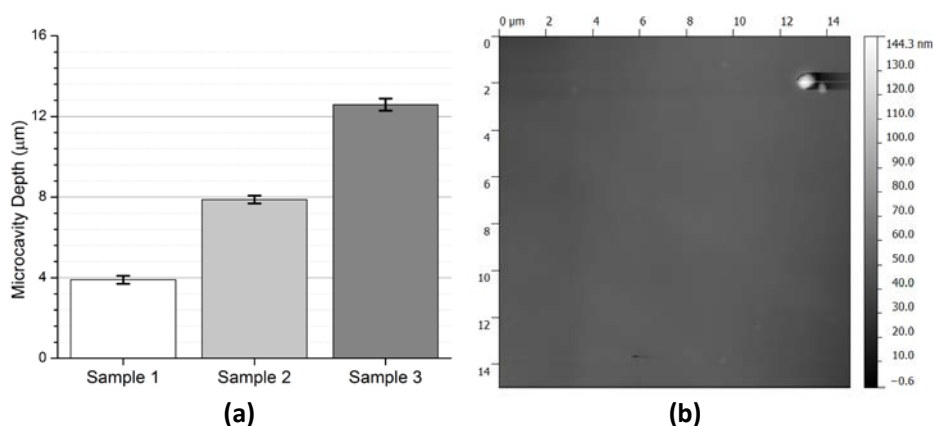
Figure 4.14. (a) Microcavity depths obtained from 2"x2" areas on quartz samples. Depths of samples were 3.9 ± 0.2 μm, 7.9 ± 0.2 μm, and 12.5 ± 0.3 μm, respectively. (b) AFM studies showing roughness of quartz (~ 3nm) after chemical processing. A dust particle due to contamination is observed on the top right.

Another important aspect of the process was finding out the surface roughness of quartz samples after physical deposition of aluminum on its surface and chemical etching to evaluate its compatibility with SAW propagation. The AFM studies show a very small surface roughness of ~3 nm which is negligible as seen in Figure 4.15(b).

The IDT electrode metal thickness was measured using a stylus based contact mode surface profiler and was found to be 140-150 nm which is smaller than 1% of the SAW wavelength and therefore can be neglected in reflection of the SAWs back to the launching electrode and beyond. Figure 4.17 shows devices on 1.3" × 1.8" substrates. Figure 4.18 shows microprobes, microcavity coupled SAW devices and 4" substrates. Diced lithium niobate substrates and microchannel samples are also shown.
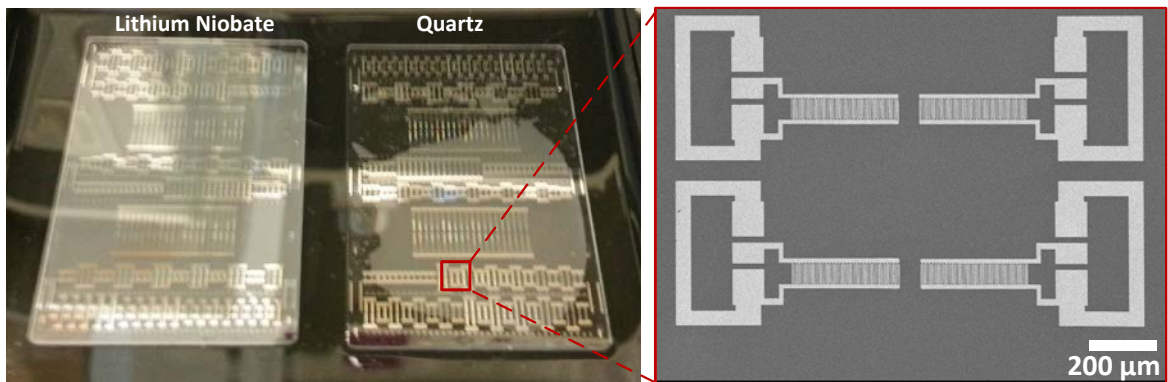
Figure 4.15. Fabricated devices on quartz and lithium niobate.
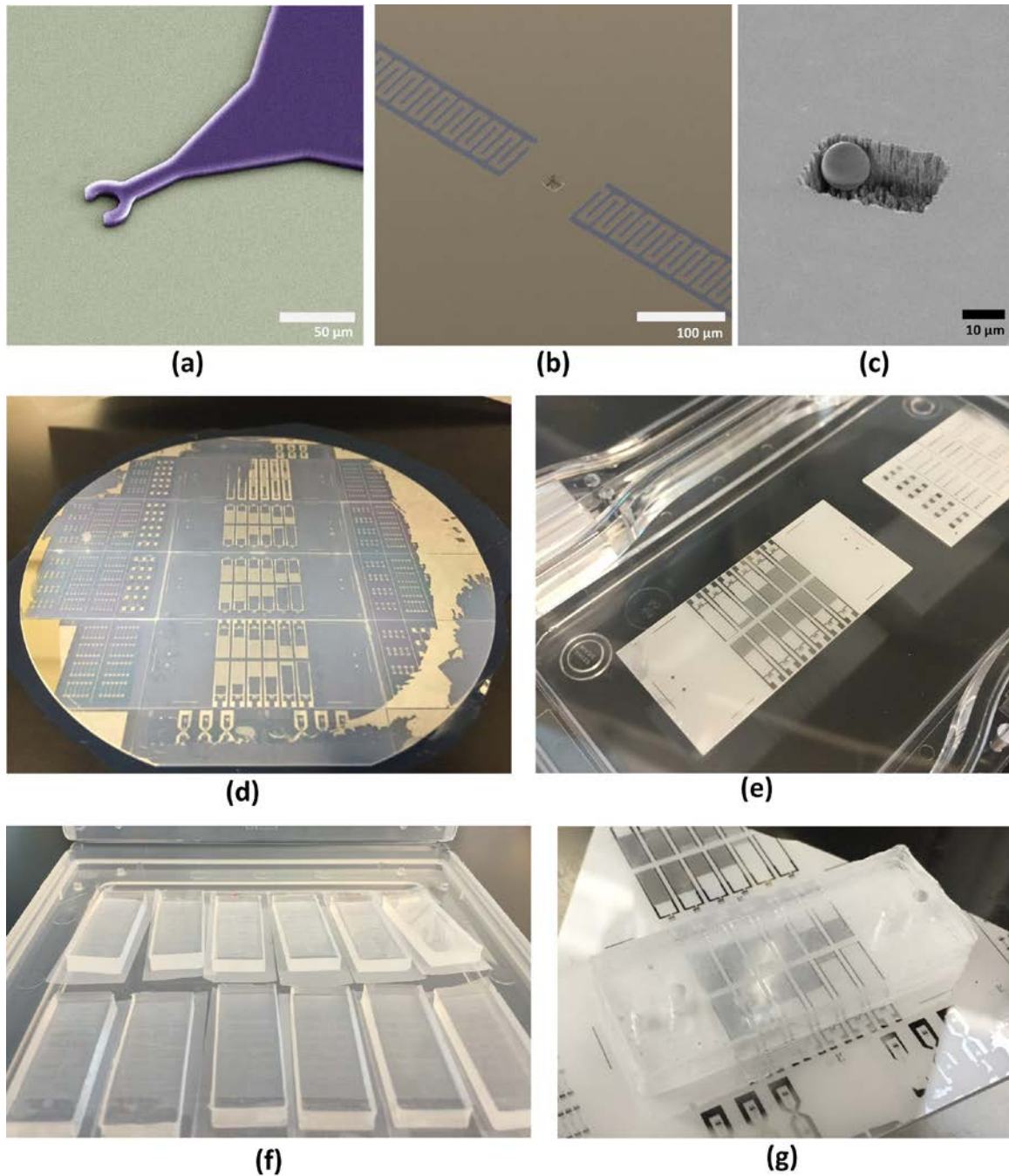
Figure 4.16. (a) False colored SEM image of an SU-8 microprobe still on handle wafer. (b) False colored SEM image of a fully fabricated microcavity coupled SAW device. (c) SEM image of a 10 µm diameter polystyrene microbead inside an 8 µm deep sample microcavity in quartz. Note that the liquid has evaporated due to required SEM observation chamber conditions. (d) A diced 4" substrate. (e) A die successfully extracted from this substrate. (f) A batch of PDMS microchannel slabs ready to use. (g) A microchannel bonded on a compatible substrate with IDTs designed specifically for the microchannel.

CHAPTER 5: EXPERIMENTS

Experimental studies on the proposed microcavity coupled SAW sensor platform forms the most important step of the process. This chapter discusses the measurement setup used for collecting data in the biomedical research labs. The major challenge of delivering ultra-small volumes of samples into microcavities in a reliable fashion is tackled next. Ultimately, measurements from microcavity coupled SAW devices are given, followed by glycerin concentration and microbead studies, leading up to tumor cell analysis. The platform integrated on a printed circuit board with a matching circuit inside 3D printed housing are also discussed at the end of this chapter.

5.1. Measurement Setup

SAW systems are discrete and spatially sampled systems. Due to their inherent properties, they can be tested as either time domain or frequency domain systems which are entirely equivalent to each other. It is usually preferred to obtain data in the frequency domain for throughput considerations. It is also more intuitional and appealing to reveal the passband characteristics in frequency domain. Therefore, most of the data has been collected in the frequency domain using two port network analyses through an automated network analyzer system. The setup is shown in Figure 5.1.
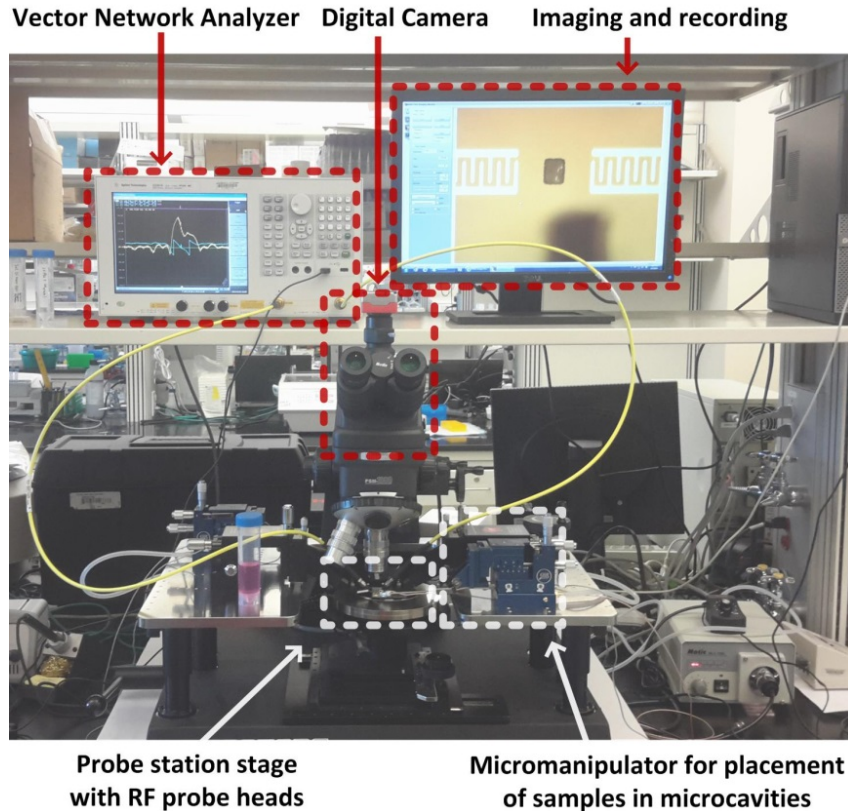
Figure 5.1. Test setup used for measurements.

The whole measurement setup is situated on top of an air table pressurized by a dedicated nitrogen cylinder. This minimizes the damage from ambient vibrations to both the substrate and test equipment and also alleviates contact problems when probing. The probe station houses two RF micromanipulators installed with two ground-signal-ground (GSG) type RF probes that operate in the 10 MHz – 40 GHz range. The probe tips have a pitch of 200 μm to reduce the internal crosstalk and they are calibrated before each set of measurements using the calibration standard, CS-5, from Picoprobe with short-open-lead-thru (SOLT) method. A sample measurement through the RF probes is shown in Figure 5.2.
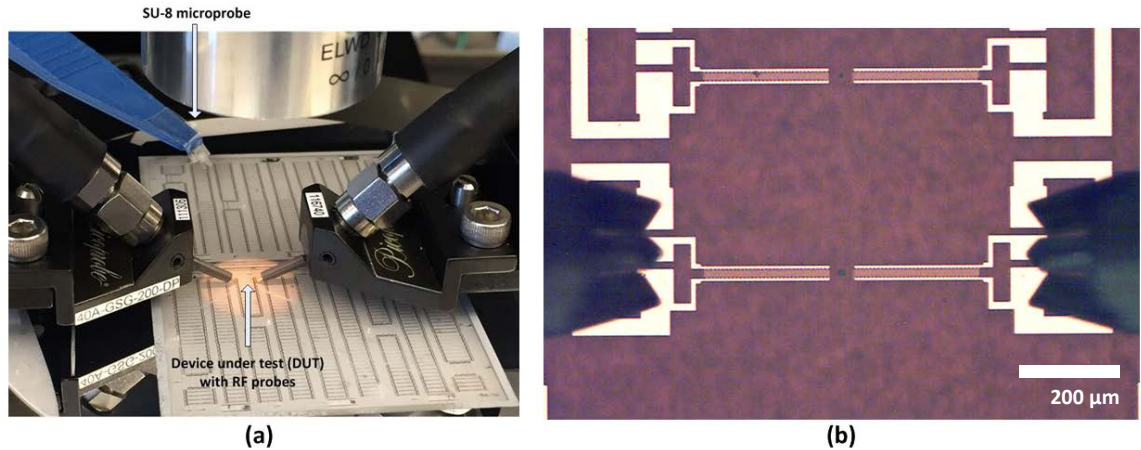
Figure 5.2. (a) Testing of devices from the third photomask set. (b) Microscope image showing probing of large aperture SAW devices from the first photomask set with GSG type RF probes.

Magnitude and phase of insertion loss (or S21, in terms of scattering parameters) data were obtained using an Agilent E5061-B vector network analyzer. The input power applied to the devices was kept low at -10 dBm in order not to damage the IDTs or cause undesired damage to cells in biological studies. Intermediate frequency bandwidth (IFBW) was selected to a low value of 300 Hz to ensure little or no leakage from the local oscillator into the output. Choosing a low IFBW also causes the measurements to take considerably longer but maintains consistent data collection. Furthermore, collected data were averaged at least four times in all measurements on the spot to rule out transient effects and limit the noise level.

5.2. Dispensation Studies

One of the biggest challenges in demonstrating the proof of concept for the SAW microcavity devices is the actual application of the sample to be measured into the microcavities. The microcavities dimensions need to be

comparable to biological cells to utilize them; therefore they have been designed for those sizes. However, at these small dimensions, with droplet volumes of less than 10 pL, there are a few fundamental issues to overcome such as manipulation (or dispensation) and evaporation. Microfluidics that are envisioned for future implemented alleviate these issues.

5.2.1. Dispensation of Liquids and Microbeads

It was experimentally verified that pure deionized water (DIW) was extremely volatile when produced in small amounts which renders it unusable. For reference, at 23ºC and 41% humidity recorded at the test labs, the time it takes for less than 10 pL of DIW to completely evaporate is less than 10 seconds. Surface tension of oils proved it to be difficult for them to stay together during placement into microcavities. Some other types of chemicals such as photoresists tend to harden and change to solid phase very quickly when in small amounts.

Contrary to other common liquids and liquid mixtures, glycerin based mixtures, due to their rather viscous nature, were seen to be easier to manipulate. It is assumed that for the measurements that the liquid droplet is analyzed a long time after it is dispensed onto the substrate compared to its wetting time, therefore it has settled and time dependent wetting processes are out of the picture. Also, capillary forces far outweigh other immediate forces acting on the droplet such as gravity, and capillary forces hold the droplet in place. According to the capillary length relation,

$$l_c = \sqrt{\frac{\gamma}{\rho g}} \qquad (39)$$

where l_c is the capillary length, γ is the surface tension, ρ is the density, g is the gravitational acceleration [73]. The capillary length calculated by this method is in the order of millimeters and is vastly larger than the droplet dimensions in the microcavity (< 30 µm), therefore effect of gravity can be ignored. Under these conditions, varying concentrations of mixtures of glycerin and DIW were prepared. For mixing purposes, glycerin and DIW were placed in Eppendorf tubes after measuring with micropipettes, and then mixed using an automatic vortexer system for 1 minute. This process was followed by ultrasonication of the tubes for 30 minutes. The obtained mixtures contained no heterogeneities or air bubbles observable by a standard optical microscope. Due to a shortcoming of the dispensation that will be explained, only four samples were prepared with 60%, 70%, 80%, and 90% were prepared and used to demonstrate the operation of our microcavity based SAW sensors.

Although the evaporation is ruled out from the list of problems, dispensation remains a big question mark. Even the smallest needles available such as gauge 25 failed to create droplets smaller than 400 µm in diameter in our experiments which is more than one order of magnitude larger than needed. For dispensation of liquids, regular DC probes with made of tungsten were used to carry them to the microcavity and apply them. Studies conducted on the quartz and lithium niobate surfaces showed liquid contact angles of ~40º which was seen to be ideal for such manipulation methods as shown in Figure 5.3. It is not

large enough to cause slip along the boundary as explained before in the previous section and it is not too small so as to inhibit manipulation such as in oils.
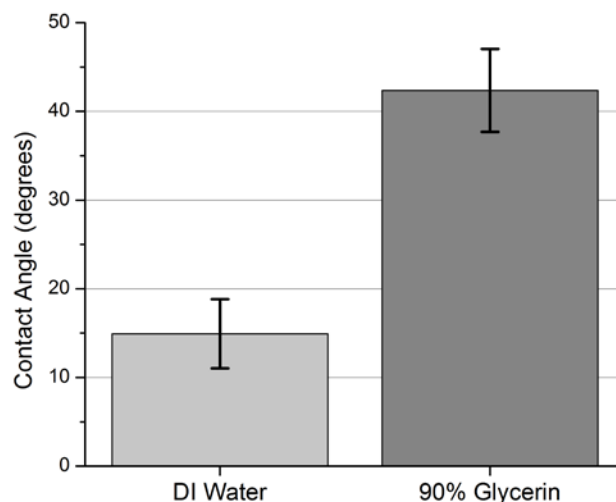
Figure 5.3. Measured liquid contact angles study on quartz. Results are averaged over seven measurements each.

This shows that they are neither too hydrophilic nor too hydrophobic. The former case would limit the minimum amount of liquid dispensable by attracting more liquid to the surface whereas the latter would cause the microcavities to reject the liquid. It was observed that 5 μm tip diameter for the probe was optimum. Figure 5.4 shows the method used for applying liquid into the microcavities and snapshots from actual application sequence. Furthermore, Figure 5.5 shows the difference in droplet shapes inside the microcavities in addition to the substrate surfaces. The droplets are seen to indeed seep into microcavities and fill them completely. It is worthwhile to note that the shapes of the liquid inside microcavities validate the assumptions made before in the

simulation steps. This process only works with glycerin content between 60% and 90% due to hydrophilicity issues.
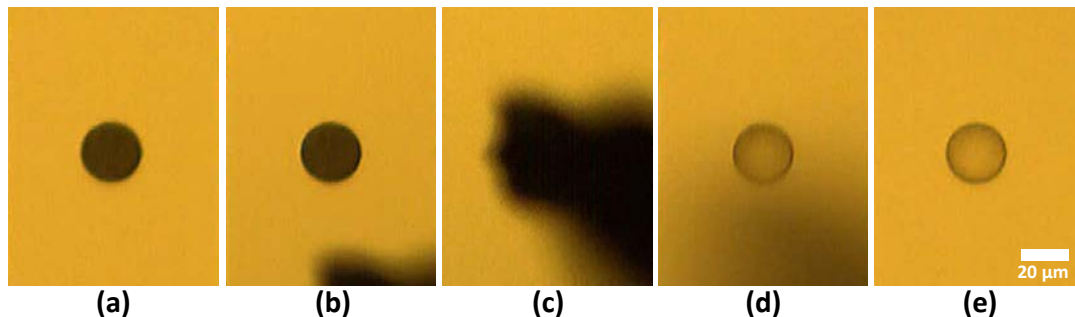
Figure 5.4. Method of applying liquids into microcavities shown sequentially from (a) through (e). The scale bar applies to all images.
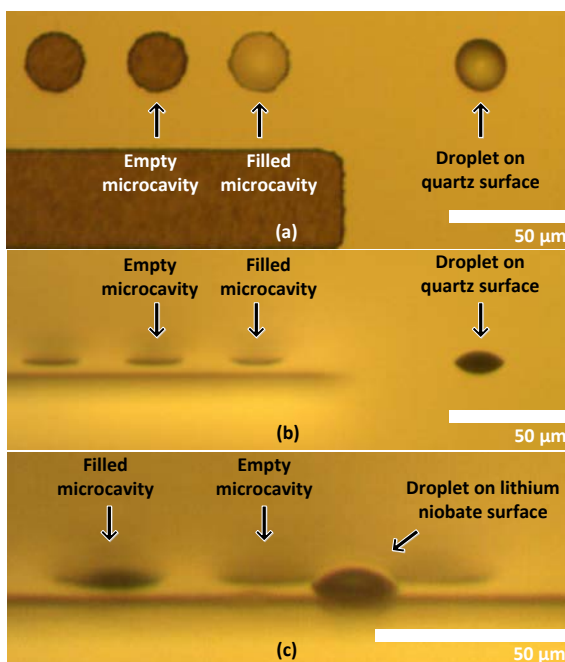
Figure 5.5. (a) Top view of liquid droplets on the surface of quartz. (b) Side view of the same area on quartz. (c) Side view of lithium niobate.

In order to test the system response to sensing and differentiating between solids by virtue of their sizes, the samples should be removable from the microcavity easily. A natural choice is polystyrene microbeads as they are

easily obtainable and applicable. Polystyrene microbeads of diameters 5 µm, 10 µm, 15 µm, and 20 µm from Polysciences were prepared for use by first spinning down using a centrifuge machine into a pellet and aspirating the original medium with water and sodium azide. Then the microbeads were resuspended in 90% glycerin. The mixture was vortexed for 1 min and ultrasonicated for 30 min to attain homogeneity. The method in Figure 5.4 could not be applied reliably with microbeads. Instead, the method shown in Figure 5.6 was used. This method was applicable as the hydrophobicity and viscosity of 90% glycerin was high enough to be manipulated without leaving residues behind.
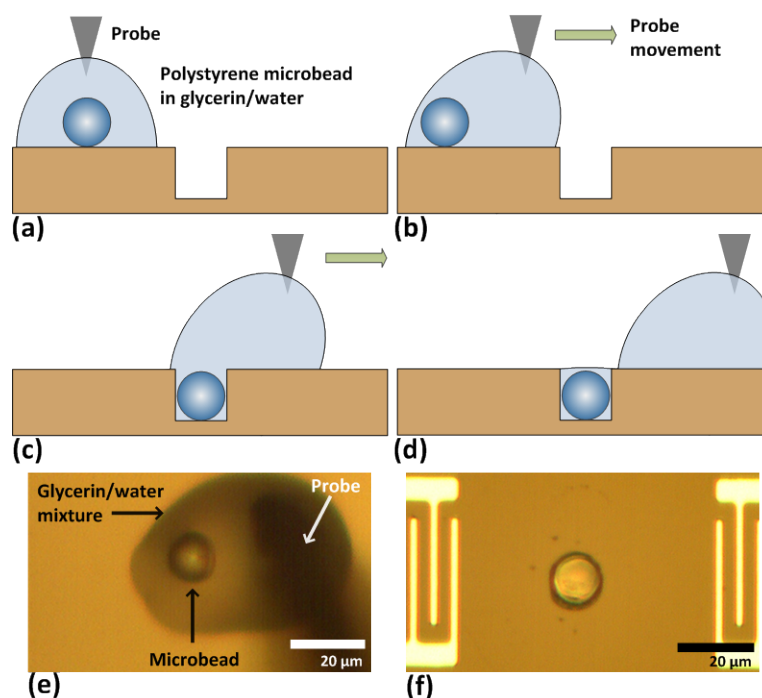
Figure 5.6. Application of microbeads into the microcavities.

5.2.2. Dispensation with SU-8 Microprobes

Biological cells are very sensitive and vulnerable to external stimuli. It was observed clearly that manipulation with metal probes similar to liquids and

microbeads was not a viable option. For this reason, the SU-8 microprobes discussed in the previous chapter were utilized to manipulate cells. These structures were attached to vacuum clamped micromanipulators to achieve precisely controlled movement of the microprobes all over the sample stage. An SU-8 microprobe attached to a 3D-printed connector piece and a micromanipulator is shown in Figure 5.7.
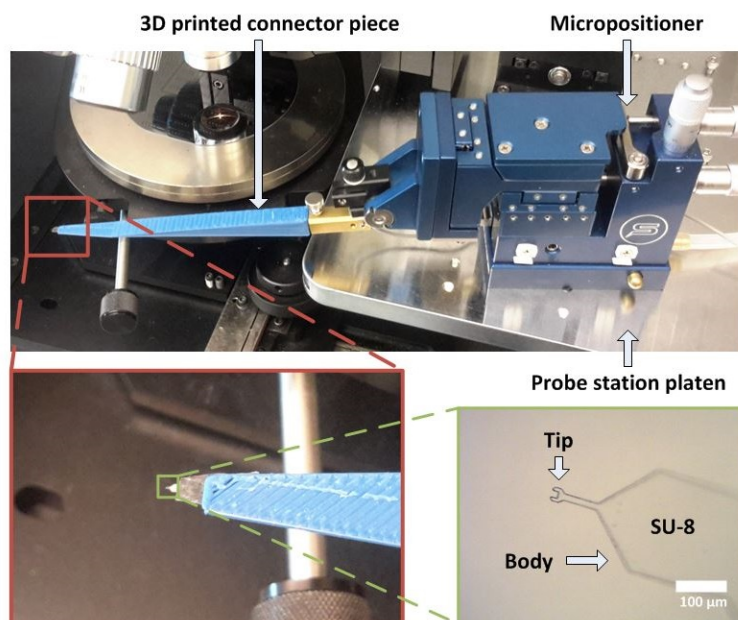
Figure 5.7. An SU-8 soft microprobe attached to a micromanipulator.

The microprobe tips were designed to simply trap and hold liquid samples using surface tension on the curved tip in the shape of a hook when the tip is brought out of the solution. The tension on the hook shaped tip is larger than the outer perimeter of a droplet so the liquid payload sticks to the tip. However, when the microprobe tip with a small protruding liquid droplet makes contact with the substrate, the droplet expands in diameter, loses contact with the microprobe tip and is released onto the substrate. The result is a uniform and repeatable

dispensing process as shown over several microcavities and different angles of incidence in Figure 5.8.
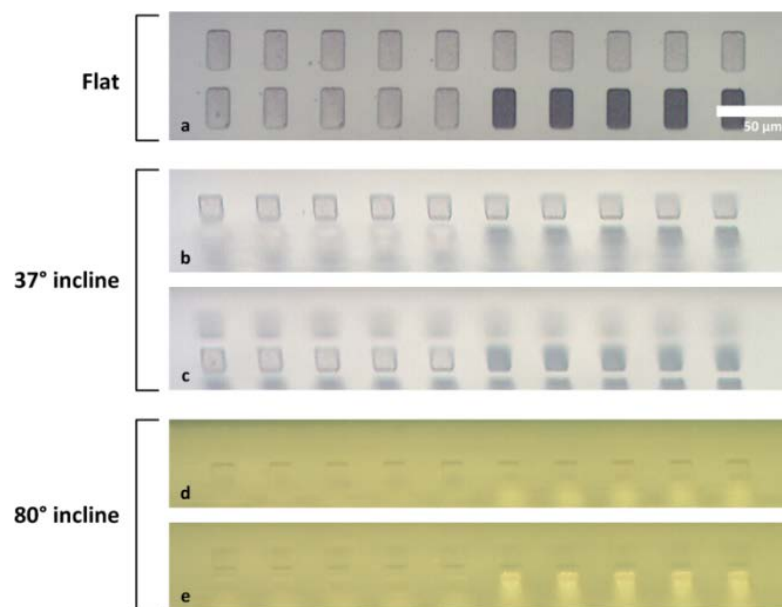
Figure 5.8. Microscope images showing uniformity among the volumes of media delivered into 15 sample microcavities out of 20. (a) Two rows of microcavities at perpendicular incidence. (b and d) The top row at differing inclines. (c and e) The bottom row at differing inclines.

The process for dispensing cells follows this same sequence of events. Firstly, a small droplet is placed on a surface using a micropipette and a cell is identified in the suspension for testing. The microprobe approaches this cell and holds it in place using the surface tension of the small droplet. After being transported to the location of interest using the micromanipulator, the cell is dispensed. Dispensation occurs as the suspension is brought into contact with the substrate by lowering the microprobe. In some cases, the cells had to be transported similar to microbeads, with the suspension still in contact with the surface. Cell viability was lower in this latter case. The process of dispensing cells is depicted in Figure 5.9.
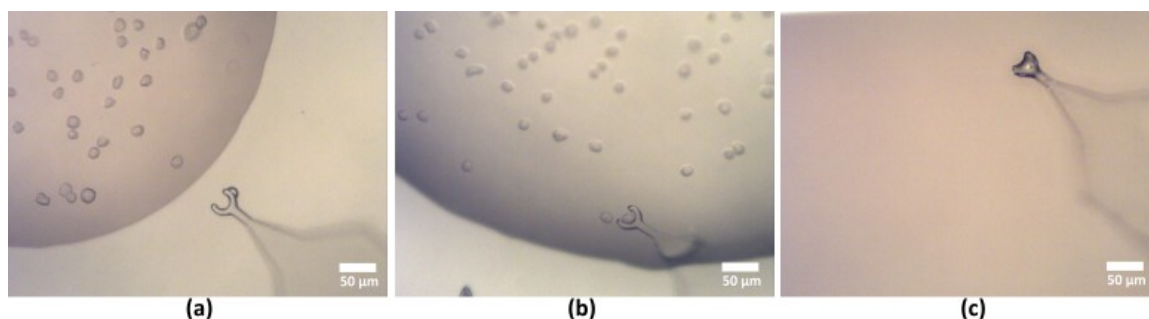
Figure 5.9. Cells being picked up from a droplet with microprobes shown sequentially from (a) through (c).

The microprobe tip dimensions and shape were determined empirically through experiments as the exact capillary forces are very hard to determine for the scales used. It was seen that the probes operate at their best when the tip is in a circular shape with an inner diameter of 24 μm with an SU-8 thickness of ~6 μm after ethanolamine treatment as described in the previous section.

5.3. Experimental Measurement Results

As mentioned in the beginning with the introduction and motivation of this study, the efforts start with liquids and solids and lead up to biological cells. So firstly, different glycerin concentrations were sensed with the system. Results with polystyrene microbeads are given afterwards. Finally, the results with biological cells are presented.

5.3.1. Liquid Sensing with Microcavities

In order to validate operation with liquids, different concentrations of glycerin in aqueous mixtures was investigated. This is in part due to abundance of data about glycerin based mixtures in the literature and in part due to practical reasons, i.e. ease of manipulation and very slow evaporation rate. DC probe

method limited the applicability of the manual dispensation approach to above about 60% glycerin concentration. Pure glycerin partly deviates from the Newtonian approximation as explained in Chapter 2; therefore, 60%-90% concentrations were employed. The resistivities of DI:glycerin mixtures are larger than 10^6 Ω-cm [119]. Therefore, for their electrical loading can be neglected for sensing purposes. On the other hand, the steady state mechanical properties of these liquids, L1 through L4, are given in Table 5.1.

Table 5.1. Properties of liquids used in experiments.

	L1	L2	L3	L4
Glycerin volume ratio in Glycerin : DI water mixture	60%	70%	80%	90%
Glycerin mass ratio in Glycerin : DI water mixture	65.5%	74.7%	83.5%	91.9%
Density (kg/m^3)	1171	1195	1218	1241
Sound velocity (m/s)	1763	1795	1817	1869
Viscosity (mPa-s)	14.0	30.0	75.7	241.7
Density-viscosity product (kg/m^2-√s)	4.0	6.0	9.6	17.3

Both quartz (8 μm deep) and lithium niobate (1.2 μm deep) samples were used in the experiments. Analysis of the data was carried out using Matlab to find the peak frequencies and the magnitude of insertion loss, and the phase shift data were averaged 8 times over for accuracy. Phase shifts were calculated around the peak frequency. The results are shown in Figure 5.10 and Figure 5.11.
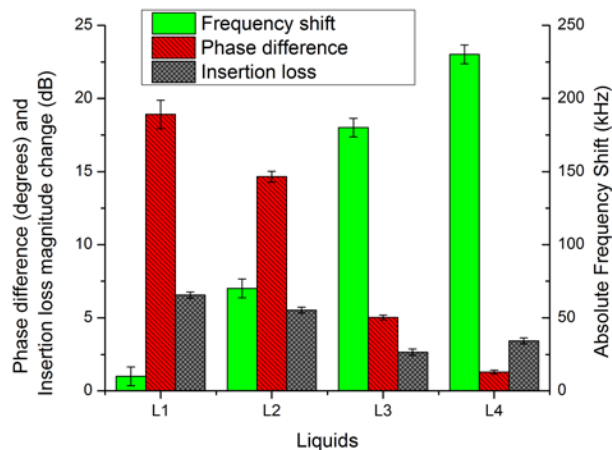
Figure 5.10. Compilation of results for Y-Z lithium niobate with 1.2 μm microcavities.
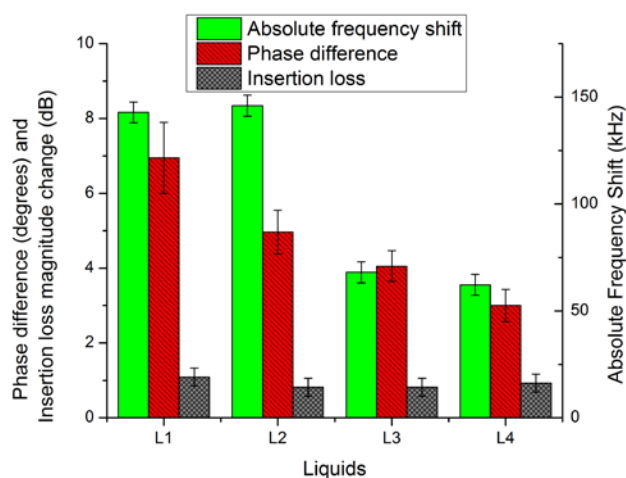
Figure 5.11. Compilation of results for ST-X quartz with 8 μm microcavities.

Judging by the results from both types of devices and as expected from simulations, insertion loss magnitude is not a reliable parameter for detection as it varies to a great extent with the exact shape of the microcavity, and in turn the portion of SAW converted into bulk waves. The effect of mass loading is more evident with the lithium niobate sample as well as acoustoelectric coupling. This

is an expected result as the microcavities are shallower in lithium niobate which, intuitively, is closer to a standard delay line condition and the piezoelectric coupling coefficient is much higher than quartz. The frequency drop increases with increased loading as expected. The slope after linear fitting is found as -16 kHz/(kg/m^2·√s) or -7.7 kHz/(% glycerin in the mixture). The phase difference is also larger than predicted with the simulations as the profile of the droplet differs by a small amount over the open top part of the microcavity. The fit for phase difference slope gives -1.3 °/(kg/m^2·√s) or -0.63 °/(% glycerin in the mixture).

On the other hand, frequency drop readings exhibit much smaller differences and are not as accurate for the deeper microcavity on quartz. This is likely due to loading effects not effectively accounted for by the simulations. Correlation for frequency shifts is therefore not adequate sensing purposes. However, the phase difference shows the same type of dependency. As the acoustic impedance of the liquid increases from L1 to L4, it starts getting closer to that of the substrate. A negative slope relation exists between the liquid acoustic impedance and phase difference for the analyzed geometries as found in the finite element analysis. The fit curve for the quartz phase change gives -0.26 °/(kg/m^2·√s) or -0.13 °/(% glycerin in the mixture). As mentioned before, rather than a direct measurement; this is a result of the resonant microcavity condition which occurs due to the specific microcavity geometry on the substrate. The shifts in phase are an indirect result of the liquid acoustic impedance. Acoustic impedance is dependent on viscosity, and viscosity is strongly dependent on glycerin concentration. As the viscosity rises, the attenuation of the

compressional waves is significantly increased. Therefore, the effect of the compressional waves at the output is lessened and the difference in phase gets smaller.

The differences between FEA and measurement results in both cases are attributed to the difference between constants used in simulations and the real samples. Frequencies that are used in experiments are in the order of 200 MHz for very small sample sizes, unlike the other studies on the topic; therefore the constants are likely to deviate from tabulated values. Furthermore, the simulations assume exact dimensions that are multiples of the wavelength, deviations from these values also cause uncertainties especially in lithium niobate with shallow microcavities. The smallest density viscosity product differentiated with the systems is 1.9 kg/m^2·√s as observed from the phase difference. The lithium niobate also gives a large frequency shift data which shows that shallow microcavities are useful for trapping liquids for measurement with less of the incoming Rayleigh wave lost to bulk waves. On the other hand, the measurements with quartz demonstrate that deeper microcavities can be used for full interaction with the surface waves although losses are more significant (partly due to losses to the bulk); therefore the signal levels are lower. Errors are also larger with quartz due to higher magnitudes of insertion loss.

5.3.2. Microbead Studies with Microcavities

After dispensation into microcavities the microbeads were examined using the same experimental protocols used for glycerin based liquids in the previous section. Phase shifts of 0.14° ±0.05°, 0.81° ±0.26°, and 3.54° ±0.49° were

obtained in rectangular microcavities for 10 µm, 15 µm, and 20 µm microbeads, respectively, as shown in Figure 5.12. Due to the larger inaccuracy of placement of smaller microbeads inside microcavities, relative error over measurements was observed to be larger as microbead size decreases.
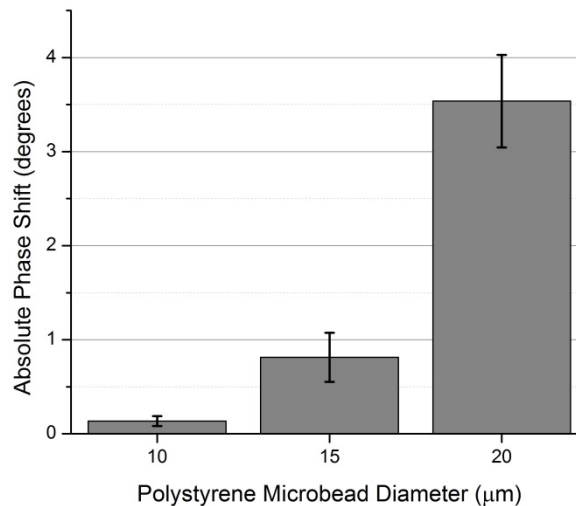
Figure 5.12. Experimental results showing the output phase signatures. The results are collected from microbeads of three different sizes in rectangular 24 × 16 × 12 µm microcavities. Values for each size are the average of four distinct measurements.

Counting or quantification of microparticles was the other concept explored during the experiments. This study was carried out for 10 µm and 5 µm beads in microcavities of various dimensions. Figure 5.13 shows 10 µm microbeads placed roughly in a single file order using the micromanipulators and the results obtained. The best results for counting these 10 µm microbeads were obtained from microcavities with dimensions of 32 × 16 × 8 µm with phase shifts of 0.51° ±0.19°, 0.98° ±0.12°, and 1.34° ±0.15° for counting one, two, and three microbeads, respectively. The motivation behind choosing the microcavity dimensions arises from finite element analysis results in the previous chapters

which show that certain microcavity depth and dimensions yield higher sensitivity. The portion of microbead that is not covered by the medium is of importance as it makes a large difference in terms of the path traveled by the acoustic wave. In this case, 8 µm deep microcavities increased the phase sensitivity for 10 µm microbeads to more than double its initial value given for the size differentiation studies.
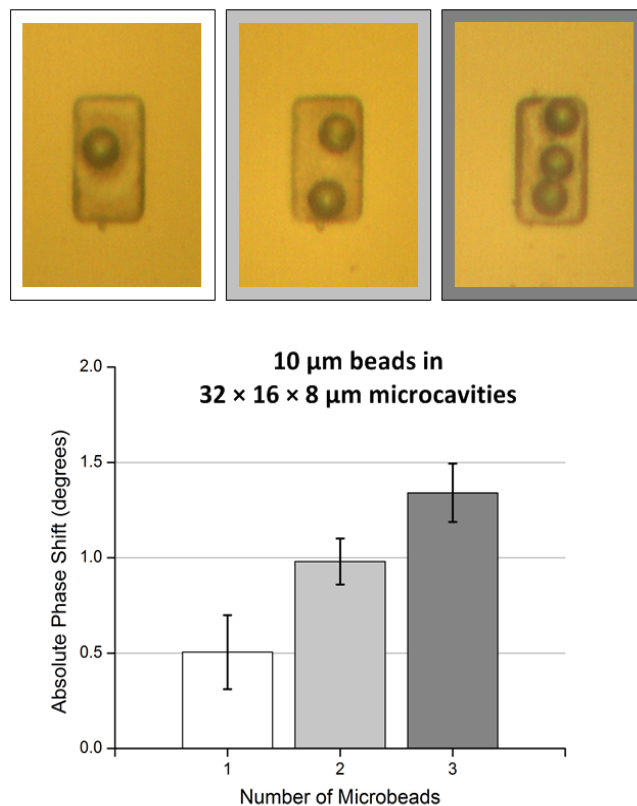
Figure 5.13. Counting 10 µm beads in 32 × 16 × 8 µm microcavities. Placement of microbeads from one set of measurements is also given.

The results obtained from these microcavities were also compared to microcavities of same lateral dimensions but with a smaller depth and with the same depth but larger length. These studies illustrated in Figure 5.14 show that shallower microcavities result in a more limited contact with the microbead in

practice. This causes smaller phase shifts to be collected from shallow microcavities. On the other hand, increased microcavity length in the propagation direction such as 32 × 24 × 8 μm results in larger relative errors and smaller shifts compared to the 32 × 16 × 8 μm microcavities.
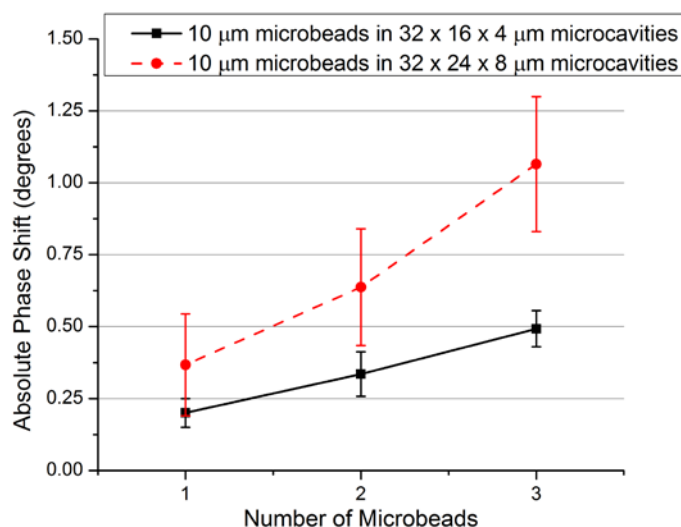
Figure 5.14. 10 μm microbeads in different microcavity geometries.

The dimensions also set a lower limit for the size of microparticle detectable using the microcavity considering the uncertainty in the data. Although microbeads larger than microcavities (such as 20 μm beads in 12 μm deep microcavities) result in the highest phase shifts due to larger displacement of medium inside the microcavity, quantification and particle counting require multiple microparticles inside the sensing zone. On the other hand, 5 μm beads proved too small compared to the lateral dimensions of microcavities as shown in Figure 5.15. These results point to the fact that microbead size should be similar to the microcavity dimensions for optimum quantification or counting efficiency. Furthermore, small sizes of the 5 μm microbeads in comparison to microcavities

result in a large deviation and show little correlation experimentally. This is a result that is expected somewhat intuitively and also proves important for measurements on biological cells.
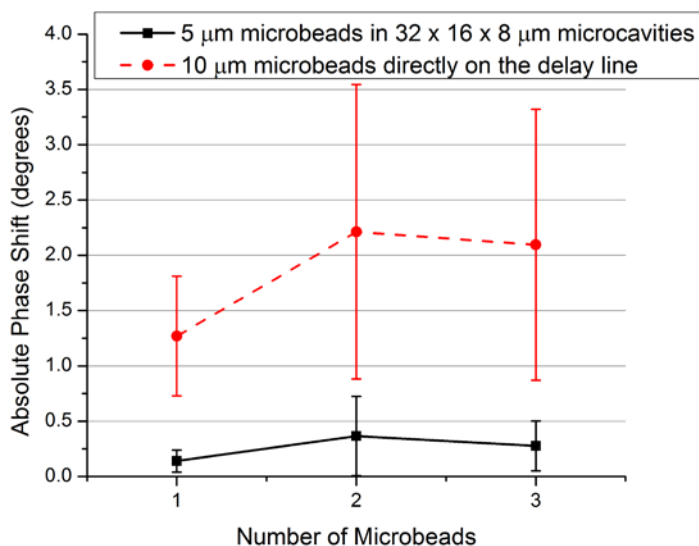
Figure 5.15. Results from 5 μm microbeads and results where no microcavity is present. The volume and shape of the samples are not repeatable, thus the large error bars for microbeads on the delay line with no microcavity.

Overall, counting results show that it is possible to enumerate beads if the microbead size is similar to microcavity depth. The measurement results generally show lower sensitivities than the finite element study results; however, exhibit the same characteristics. This can be attributed to differences in material constants used in simulations as well as variations in particle locations during measurements.

In simulations, the particles are precisely ordered in the sensing region; however, in the experiments there are large variations in the particle placement. Ordering particles very accurately inside microcavities is not easy using the

probes as illustrated in Figure 5.13. The deviation of polystyrene microbeads from their simulated locations is accepted as part of the data to evaluate the robustness of the system. The deviation in the collected data was large especially for 5 µm microbeads. The microbead placement is the biggest problem for the no microcavity case which was presented in Figure 5.15. When the microbeads were dispensed directly on the delay line without the microcavity, the sample volume is not consistent and gives rise to ambiguous readings even though the overall phase response is larger. The microbeads are usually not in a single file order and the hemispherical shape of the droplet changes for every measurement along with the total volume of the solution. The proposed concept of using the microcavity resolves this problem by restricting the sample to a certain volume and shape.

The uncertainty of readings due to sample placement was also investigated. For these tests, the same 10 µm microbead was placed in different arbitrary locations in the same 32 × 16 × 8 µm microcavity eight different times to calculate the standard deviation. These measurements yielded a phase uncertainty of ±0.28°. The placement of the microbeads was more randomized and extreme than the other measurements in this case to test the system limits.

5.3.3. Biological Cell Studies

Four different cell lines were selected and tested with the proposed platform. Three cells were selected based on their similar origins whereas two of these have similar tumorigenic potentials. The fourth cell line is of a similar tumorigenicity but of a separate origin to provide contrast. During the culture

process, cells were cultured up to similar confluence levels, treated in the same way, placed in the same containers, etc. in an effort to minimize the effect of environmental factors on the measurements. Therefore, based on their properties these cell lines provide a good picture of the capabilities of the proposed system in relation to distinguishing between different cells.

A human chondrosarcoma cell line, JJ012, along with breast cancer cell lines MDA-MB-231, SKBR3, and MCF7 were used in the biological cell studies. All breast cancer cell lines were obtained from ATCC whereas the JJ012 cells were obtained from Dr. Jonathan Trent at Sylvester Comprehensive cancer center at University of Miami. All breast cancer cells are epithelial cells derived from metastatic site originating from pleural effusion. JJ012 cells are of mesenchymal origin (obtained from cartilage tissue) and are known for being hard to treat with radiation methods. All types of cells were cultured separately in RPMI media. They were incubated at 37 ºC in under dark conditions and 5% CO_2 atmosphere until they reached confluence. They were removed from culture flasks using trypsin, formed into pellets, and resuspended in the measurement medium prepared prior to measurements. The measurement medium consists of 1xHBSS to maintain isotonicity to extend cell life and to maintain a healthy pH level along with 5% v/v glycerin. The augmentation with glycerin is necessary in order to avoid evaporation during measurements as well as to increase the surface tension for microprobe dispensation. After mixing, the medium was vortexed for 1 min and treated in an ultrasonic bath for 30 min to attain homogeneity.

The residual content from RPMI left in the measurement medium at the resuspension step adversely affects the surface tension of small sized droplets (<50 μm). This makes it very difficult to use the microprobes. In order to address this issue, the cells were processed using a centrifuge machine to form pellets and resuspended in the measurement medium three times, while carefully aspirating the remaining RPMI to the maximum extent. A small volume of ~1 μL of resulting medium containing cells is then placed on an unused area of the substrate using a micropipette. Individual cells are picked from this droplet and dispensed into microcavities using SU-8 soft microprobes. Microscope images of cells placed in microcavities are shown in Figure 5.16.
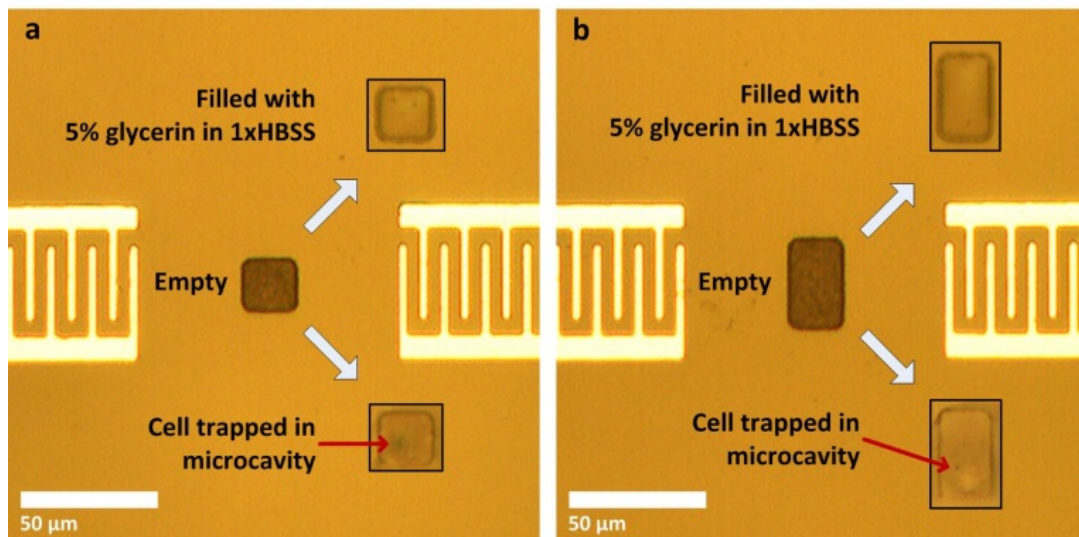
Figure 5.16. (a and b) Dispensed cells. The two stages of the differential measurements are shown with the arrows, i.e. where the microcavity is filled with only the medium and where the microcavity contains the medium with a cell in it.

Data analysis was carried out using Matlab, and the phase shift data were measured along the passband of the device around the peak frequency

according to previous measurements. The phase shifts were obtained by comparing the cases where the medium alone fills the microcavity and where the cell is in the microcavity with a sample measurement shown in Figure 5.17. Using this process, the differential properties of the cell in comparison to the medium it displaces are measured and uncertainties due to the glycerin based medium are minimized. In the cases where microcavities are much larger than cells, such as in Figure 5.16(b), phase differences are scaled accordingly.
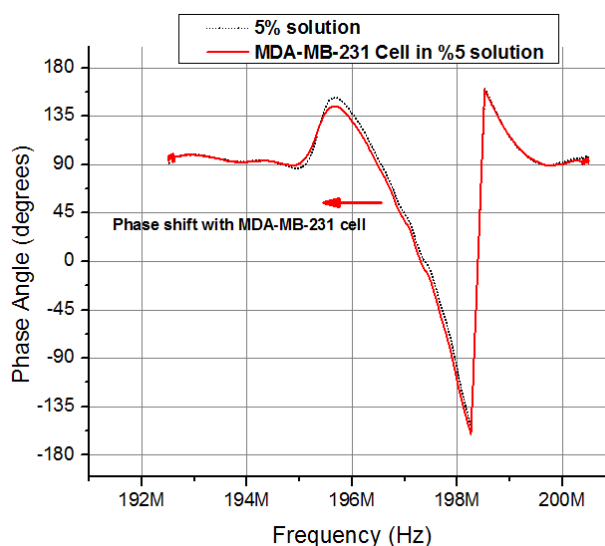
Figure 5.17. Sample measurement data from MDA-MB-231 cells with the phase shift shown.

The sizes of the cells were measured using the optical microscope before and after dispensation to ensure similar size cells were used in order to keep the results consistent. The diameters of the cells over the populations used for stiffness measurements were found to be 16.0 ±0.7, 14.7 ±2.0, 14.3 ±1.1, and 15.8 ±2.1 µm for SKBR3, MCF7, MDA-MB-231, and JJ012 cells, respectively,. The cells have similar dimensions. These size measurements further justify the

correlation between ultrasound velocity and phase shift by ruling out solely size-based detection. In the experiments, at least five different cells were measured from each population. Individual results from some sample cell lines are shown in Figure 5.18. Overall populations yielded phase shifts of 1.84º ±0.24º, 1.62º ±0.57º, 4.26º ±1.43º, and 2.43º ±0.94º for SKBR3, MCF7, MDA-MB-231, and JJ012 cell lines, respectively.
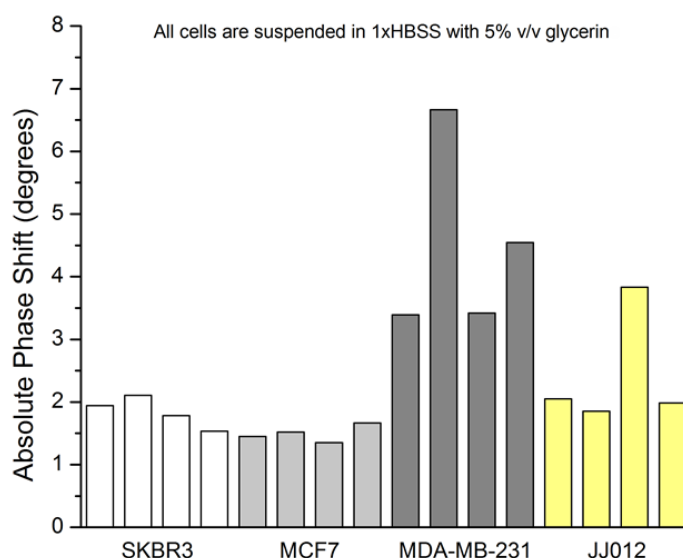
Figure 5.18. Sample compilation of individual phase shift data collected from four different cell lines.

The microcavity coupled SAW biosensor is not operating in the mass loading mode and as a result, the contribution of density is very small. Since its effects on the output phase are negligible, density becomes important only for estimation of elasticity but cannot be accurately determined by the proposed system. For this reason, wet weighing tests were run on MDA-MB-231 and MCF7 cell lines. After the cells were submerged in HBSS/5% glycerin solution for 15 minutes, pellets were formed. The masses of individual cells were determined by

counting in the small effect of the glycerin intake in the form of volume expansion and the number of cells. Cell sizes and counts were obtained using a Nexcelom Cellometer T4. Densities of 0.987 ±0.016 and 0.990 ±0.013 g/cm^3 were obtained for MDA-MB-231 and MCF7, respectively from four different samples. It is thought that with certain finite glycerin intake, cells settle at a certain level below the density of the HBSS/5% glycerin medium. On the other hand, the density of this medium was measured as 1.013 g/cm^3. This agrees with the expected value of 1.014 g/cm^3. The cells are all assumed to have a density of 0.990 g/cm^3 which was obtained from the averages and plugged in for calculating the estimated stiffness moduli.

The elastic moduli of the cells were extracted from the phase shift measurements according to the trends of Figure 3.22 by curve fitting and by using equation (37). The compilation of results with estimated elastic moduli extracted from phase angle measurements for all cell lines is given in Figure 5.19. Subsequent measurements with a given SAW device yielded an uncertainty of degrees ±0.15° which forms the basis of the noise from measurement to measurement. The same exact SAW device was used for taking the differential measurement (first the reference measurement with the medium and the second measurement with the medium and the cell) for each cell. However, a distinct device was used for every set of differential measurements in order to avoid any cellular residues after the previous measurement. In the end, as many distinct devices were used as the number of cells. The approximate theoretical sensitivity was given as ~0.35º/MPa from the finite element analysis. The throughput of the

system is quite low, with a cell placement taking up to 10 minutes. As cells are measured in groups of 3 or 4, the throughput is around this number of cells per hour whereas the average overhead from the onset of microprobe use to taking the measurements is around 30 minutes for each cell. These results are summarized in Table 5.2.
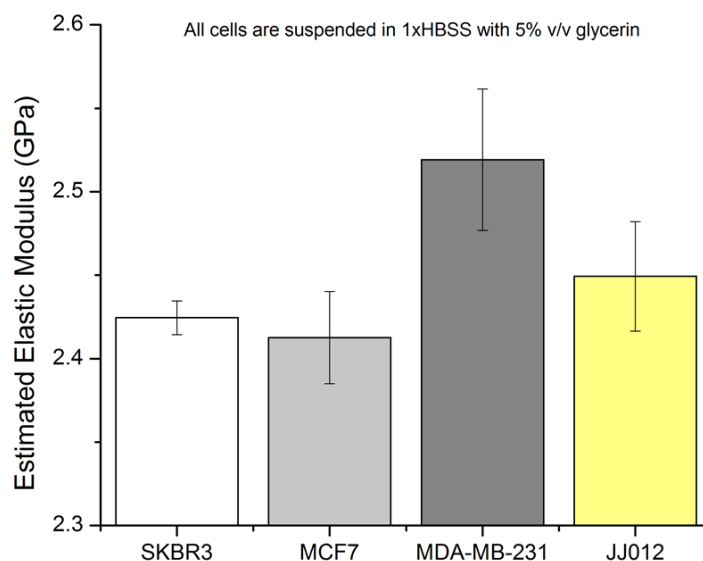
Figure 5.19. Compilation of stiffness data collected from four different cell lines.

Table 5.2. Measurement statistics and characteristics of the platform.

Number of measurements from each cell	8
Number of distinct cells measured	28
Number of distinct devices used	28
Approximate theoretical sensitivity	~0.35º/MPa
Noise from measurement to measurement	±0.15°
Minimum signal-to-noise ratio for cell measurements	5.49
Average overhead for cell dispensation	~ 30 mins
Throughput	~ 3-4 cells/hour

Some of the cell lines were seen to form discernible populations. Statistical analysis of the results starting with ANOVA showed that null hypothesis can be rejected. Subsequent analysis was carried out using student t-tests among separate groups of data. Results from MDA-MB-231 cells were statistically different from all of the other cell lines with greater than 99.9% confidence. However, MCF7 and JJ012 lines are distinguishable with 95% confidence. Final measurement results from cells are put together in Table 5.3. This compilation of results serves as a lumped model of cells for further studies as well as a library for their very high frequency behavior.

Table 5.3. Library of biophysical properties for analyzed cells.

	MDA-MB-231	SKBR3	MCF7	JJ012
Origin	Breast Cancer	Breast Cancer	Breast Cancer	Chondrosarcoma
Type or Origin	Epithelial (mesenchymal phenotype)	Epithelial	Epithelial	Mesenchymal
Tumorigenicity	High	Medium	Medium	High
Mean Diameter (μm)	14.3 ± 1.1	16.0 ± 0.7	14.7 ± 2.0	15.8 ± 2.1
Mean Wet Mass (g/cm^3)	0.987 ± 0.016	N/M	0.990 ± 0.013	N/M
High Frequency Mean Elasticity (GPa)	2.516 ± 0.054	2.425 ± 0.011	2.413 ± 0.028	2.449 ± 0.038

Although MDA-MB-231 cells are epithelial cells derived from breast tissue, they are reported for expressing mesenchymal-like behavior as well [120]. Taking into account the similar phenotype with JJ012 cells, similar moduli might be

expected from MDA-MB-231 and JJ012 cells. This is actually how they are placed among the cell lines in the results (somewhat separate from MCF7 and SKBR3). SKBR3 and MCF7, very similar cell lines, are also statistically similar. SKBR3 and JJ012 lines are also not statistically different despite the expected difference between them.

Glycerin is known to be readily metabolized by cells and change the cytoplasmic contents. This, in turn, is expected to lower the apparent bulk moduli of the cells after a certain amount of time. Measurements taken from MDA-MB-231 cells over a period of over two hours shows decreasing phase shifts as anticipated. Different phase shifts are obtained as starting points; however, the glycerin intake is observed in all of them in roughly the same manner. These measurement results are given in Figure 5.20.
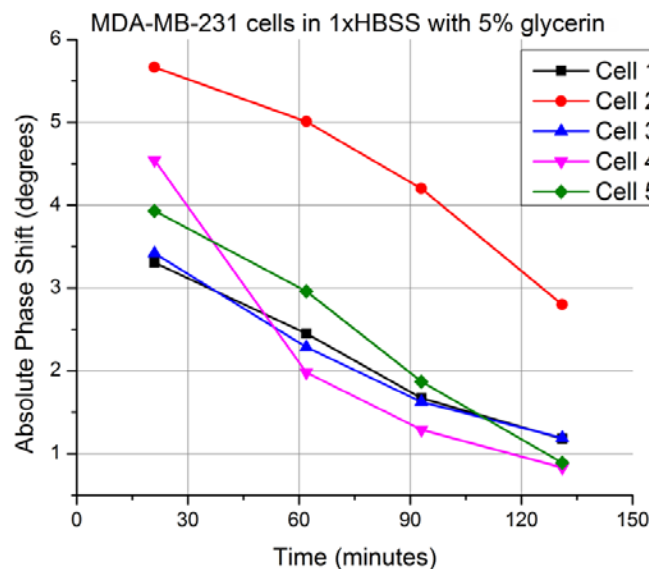
Figure 5.20. Measurement from same MDA-MB-231 cells over time, suggesting glycerin intake.

Cell viability is an integral part of the system. Before measurements, cells are kept strictly in growth medium with enough nutrients and at bodily temperature. However, for the measurement process they are separated from a relatively large volume of medium and placed in an HBSS medium. Furthermore, manual dispensation of the cells into microcavities is also a time consuming process. For this reason, the cells need to be checked for viability for extended periods of time in HBSS media at room temperature. This test was run using an automated cell counter on MDA-MBA-231 cells over a period of 5 hours. The results in Figure 5.21 show that more than 90% of the cells were viable more than 5 hours after harvesting from culture flasks.
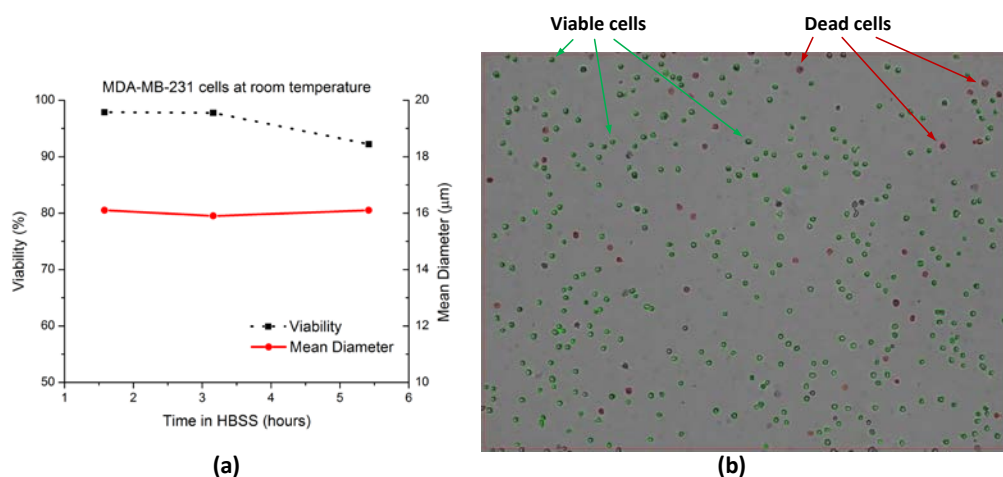
Figure 5.21. (a) MDA-MB-231 cell viability and cell size measured over 5 hours with Nexcelom Cellometer T4 using Trypan blue dye exclusion protocol. (b) Image processing results at 3 hours and 10 minutes. Green outlines show viable cells whereas the red circles outline cells that take up Trypan blue. Some sample viable and dead cells are pointed out.

During actual measurements, cells are under acoustic pressure. This pressure, albeit small, is enough to start a resonance in the microcavity. For this reason, cell viability was also investigated directly inside microcavities. MDA-MB-

231 cells in regular HBSS/5% glycerin measurement medium were augmented with 1:1 (v:v) 0.4% Trypan blue solution. After dispensation into microcavities, acoustic waves were applied for 3 and 10 minutes with an electrical input power of -10 dBm to the input IDT. This input power applied to the IDTs in question yield about 10-20 kPa of peak pressure in the microcavity according to finite element simulations not shown here. No significant cell damage was observed afterwards, despite the resonance formed in the microcavity. Results for this experiment are given in Figure 5.22 along with regular cells in droplets for comparison purposes.

Viable cell in HBSS in large area droplet   Dead cell in HBSS in large area droplet   Cell after 3 min of 10-20 kPa   Cell after 10 min of 10-20 kPa
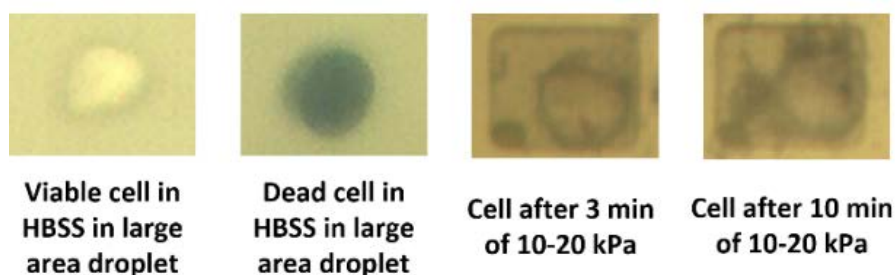
Figure 5.22. Microscope images of MDA-MB-231 cells after a set of measurements in the HBSS/5% glycerin medium including Trypan blue. One viable and one dead cell in a separate large droplet are included on the left for comparison purposes. The cells in microcavities shown on the right do not take up the Trypan dye.

5.3.4. Integration of the System with PCB and Housing

The high frequency PCB described in section 3.9 was sent out for manufacturing and used for demonstrating PCB integration. For these measurements, regular delay lines on lithium niobate with no microcavities were used as shown in Figure 5.23. These devices contain two identical IDTs with 30 split finger pairs, with an aperture of 20 μm, and a short circuited delay line.
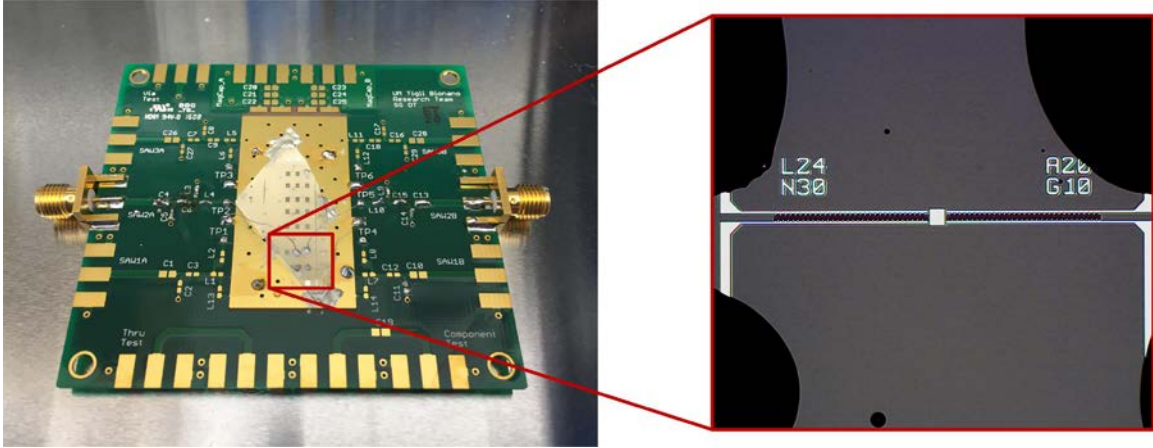
Figure 5.23. SAW delay line on a lithium niobate die connected to the PCB. A microscope image of the device with large conductive epoxy bonding interfaces on the device pads is also shown.

Wire bonding to aluminum on the pads was not possible due to adhesion problems with the gold ball bonding setup available. As a solution, one ends of thin metal wires were soldered onto the pads on the PCB. The other ends were connected to the devices by applying conductive epoxy with q-tips and curing at 100 °C for 10 minutes. In order to demonstrate a working device integrated with the PCB, unused component solder pads are soldered as short circuits whereas surface mount 0402 packaged capacitors and inductors are used for components. The circuit model used for matching is shown in Figure 5.24.
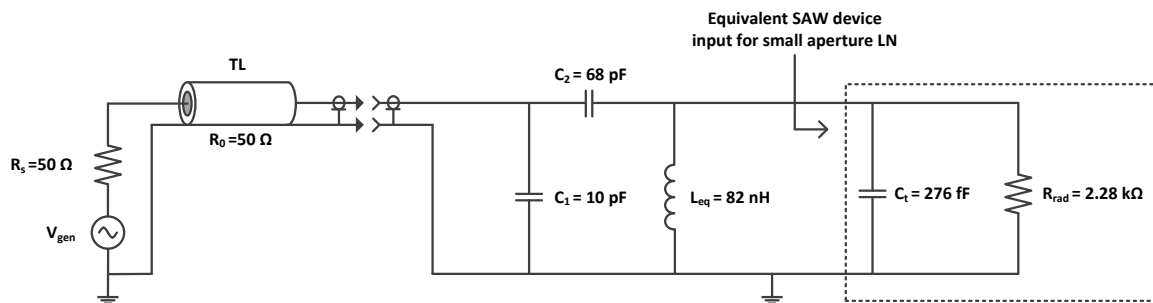
Figure 5.24. Equivalent model with the tapped capacitor matching circuit.

The tapped capacitor type matching circuit was simulated using LTspice for a SAW delay line at the passband frequency of approximately 144 MHz. The inductance, L_{eq}, is the parallel equivalent of two inductors. First one of these inductors is 90 nH, and this is the one illustrated in Figure 3.24(d) to complete the tapped capacitor transformer. The second inductor is quite large (4.42 µH) and used for bypassing the unusually small equivalent capacitance of the SAW device (276 fF) that is a result of the small aperture. These two inductances are absorbed into the equivalent inductance of 82 nH in an effort to keep the component values manageable. Connections from the VNA to the board are made through SMA connectors and flexible cabling. The cabling and SMA connectors were calibrated before measurements using SOLT method on the available test ports and 50 Ω external loads. Results from these measurements are shown in Figure 5.25.
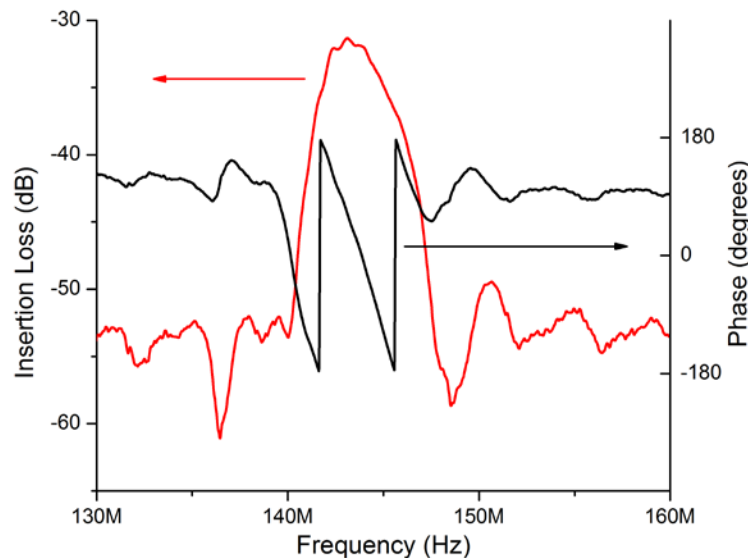
Figure 5.25. Measurement results from the PCB with matching circuit using flexible cabling.

The unusual wire connections between the PCB pads and SAW device pads, and their large footprints add parasitic capacitances and inductances to the circuit model of Figure 5.24. Furthermore, cost efficient flexible cables were used on purpose instead of the high quality cables displayed in Figure 5.1. Despite these conditions combined with the non-ideal input impedances of the devices, the insertion loss was found to be around -31 dB with the matching circuit in place with very linear phase characteristics.

In the end, the benefit of this approach with PCBs is the possible increase in performance with reduced noise, as well as reduction in overall size. In order to keep the PCB and devices together and shield them from the outside, the 3D printed housing shown in Chapter 4 was utilized. The overall system with the housing, PCB, and VNA is shown in Figure 5.26, much smaller in size compared to the setup in Figure 5.1.
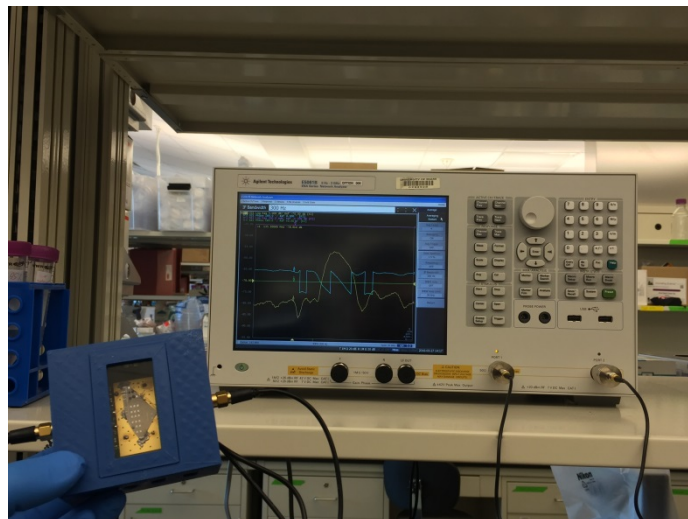
Figure 5.26. Integrated system showing the VNA, PCB, and the measured SAW device in the 3D printed housing.

5.3.5. Initial Results from Integration with Microfluidics

The efforts detailed in Chapter 4 extend to integration of SAW device biosensors with microfluidics. The fabrication studies detailed the alignment and bonding of microfluidic channels to compatible with SAW devices. These are quasi-chirped devices with reflector arrays and responses at multiple frequency bands. Therefore, the passband response presents multiple localized maxima and minima. This manifests itself as a high passband ripple. In this section, initial measurement results from these devices with no microcavity are presented. Therefore, these results serve only to demonstrate the capability of microfluidic integration during the testing phase which is shown in Figure 5.27.
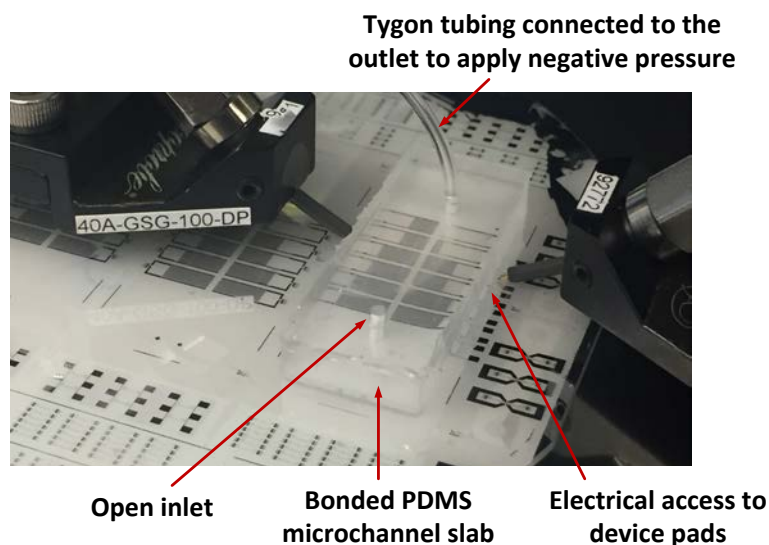
Figure 5.27. Experimental setup for microfluidic testing of SAW devices. The UMP3 micropump connected to the outlet through Tygon tubing is not shown.

The specific device used for microfluidic testing has an aperture of 2 mm and a passband peak frequency around 215 MHz with extreme levels of passband ripple. The delay line is partly loaded with the PDMS microchannel

sidewalls that are 200 µm wide. There is no mass loading on the IDT electrodes as the PDMS slab is hollow in these regions. The microchannel is 150 µm wide and 30 µm high. No electrical shorting structure is present in the microchannel to prevent electroacoustic coupling to liquids. The microchannel is filled using a UMP3 micropump driving a 1 mL syringe to create negative pressure in the outlet. The liquid to be tested is dispensed using a syringe into the open inlet port. This liquid fills the microchannel upon application of negative pressure through the outlet. Empty and filled microchannels are shown in Figure 5.28.
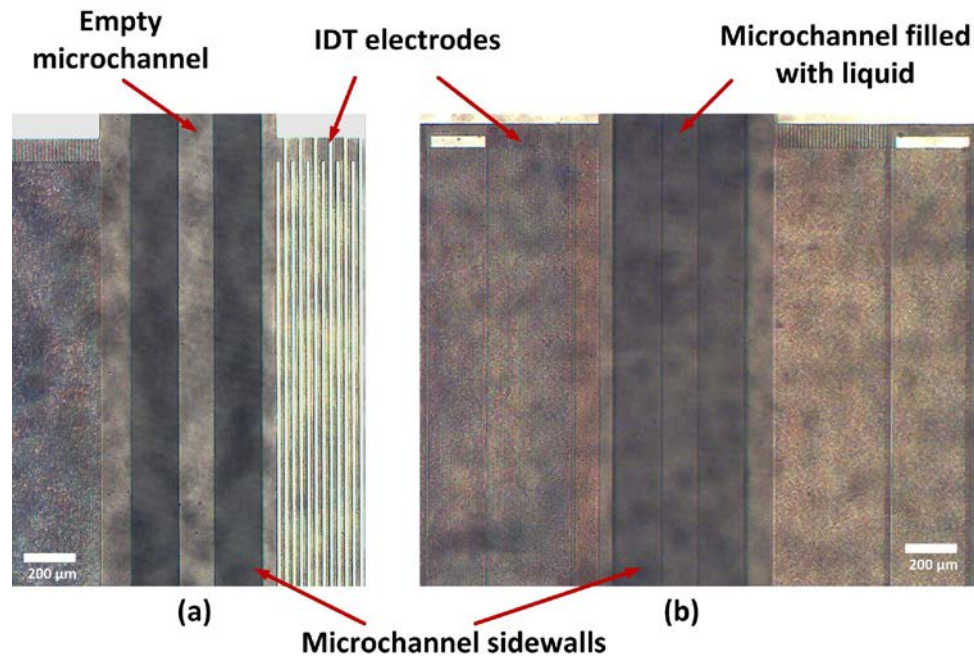
Figure 5.28. Testing steps showing (a) the empty microchannel and (b) liquid in the microchannel. The IDT electrodes are shielded from being loaded by the PDMS and the liquids.

Once the measurements are taken for a liquid, the microchannel is emptied by applying negative pressure again. The process is then repeated for other liquids. The system is operated using negative pressure to avoid bursting

the contact bonding at the PDMS/substrate interface. The results were collected for empty microchannels, and microchannels filled with 0%, 5%, 10%, 15%, and 20% glycerin content in aqueous solutions of glycerin. The results are given in Figure 5.29.
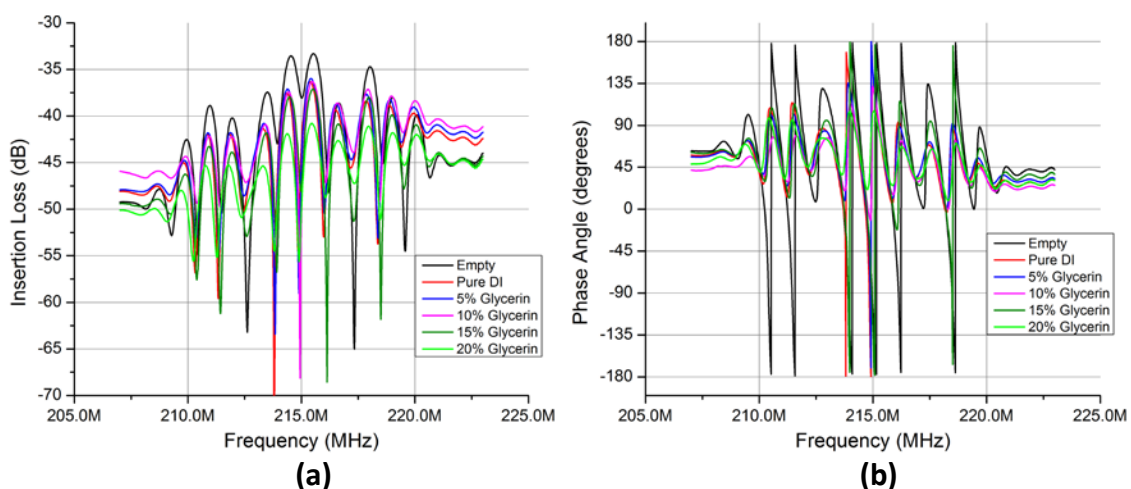
Figure 5.29. Insertion loss and phase measurement results for SAW devices integrated with microfluidic channels.

Due to the extreme ripple in the supposed passband region, the peak at 215.5 MHz was set as the reference point for calculation of experimental results. The insertion loss measurements show a marked drop in the magnitude of signal transmission although. Phase results are delayed as expected due to the presence of the liquid samples. Frequency is also shifted in response to the glycerin concentration whereas insertion loss is not a good indicator in a similar fashion to the results from liquid sensing with microcavities. However, neither the frequency nor the phase shift seems to be strictly proportional to glycerin content for 20% glycerin. Overall, the results were consistent when retesting a given liquid sample. A compilation of these results is given in Figure 5.30.
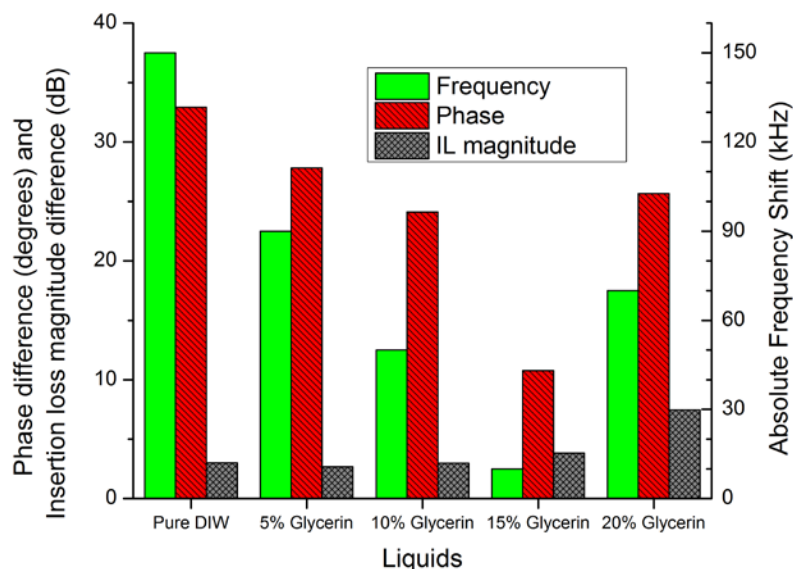
Figure 5.30. Compilation of initial results from low concentration glycerin in PDMS microchannels.

In contrast to the studies of liquids using microcavity coupled devices, the microchannel volume is orders of magnitude larger. The acoustic apertures are orders of magnitude larger than the microcavity coupled counterparts, and device designs are markedly different. Therefore, the resonance conditions in the enclosed volume are more difficult to obtain and are possibly quite different. Furthermore, acoustoelectric coupling might be causing interference with mechanical coupling. Ultimately, these initial results show that sensing is taking place; however, specifically designed SAW devices, further analysis through FEA, and further testing with more samples are necessary for a better understanding. Devices based on SH-type surface waves are also expected to operate better for future designs for this type of application.

CHAPTER 6: CONCLUSIONS AND FUTURE WORK

This study presented the microcavity coupled SAW device concept for analyzing biological cells and other materials at the micron scale. The system has been demonstrated to work for glycerin based liquids by measuring their high viscosity and for distinguishing between the sizes and numbers of polystyrene microbeads. Ultimately, the microcavity coupled SAW device concept was demonstrated for tumor cell differentiation.

For liquid testing, SAW sensors were prepared on Y-Z lithium niobate and ST-X quartz substrates and etched to form microcavities. Liquid mixtures with varying glycerin/DI water contents were prepared for testing and then dispensed into the microcavities using probes and micropositioners. The characteristics expected from finite element simulations were also observed from measurements, and the proposed system with a microcavity has been differentiated from regular mass loading mode operation. The behavior of the system becomes closer to that of a mass loaded delay line if the microcavities are very shallow and the effect of microcavities are more clearly observed when microcavities are etched deeper as correlation is maintained between the liquid properties and the phase. Lithium niobate provides a higher sensitivity due to its higher coupling constant but can only support small depths of microcavities. For more controlled volume testing, quartz with specific microcavity depths was considered. Materials with higher acoustic impedances placed in microcavities cause smaller shifts in the phase of the output insertion loss for the considered geometries. The phase shift

operates in a cyclic fashion after some point in the density-viscosity product, and sets an upper limit to the dynamic range of the system. As a conclusion, less than 5 pL volume of DIW:glycerin with concentrations varying between 60% and 90% have been analyzed using the setup and the minimum detectable density-viscosity product among measurements was 1.9 kg/m$^2 \cdot \sqrt{s}$.

Sensing and counting of polystyrene microbeads were other applications of the system building up to biological cells. It was shown that the proposed platform is capable of differentiating between the sizes as well as the numbers of identical polystyrene particles suspended and trapped in identical media. For separate size of microbeads, phase shifts of 0.14° ±0.05°, 0.81° ±0.26°, and 3.54° ±0.49° were obtained in rectangular microcavities for 10 μm, 15 μm, and 20 μm polystyrene particles, respectively. For particle counting purposes, highest sensitivity was obtained where 10 μm microbeads were successfully quantified with 0.51° ±0.19°, 0.98° ±0.12°, and 1.34° ±0.15° phase shift data collected for respectively increasing number of polystyrene microbeads. Insufficient correlation is observed for 5 μm particles. This result points to the fact that smaller microcavities are needed for smaller particles of this size, as supported by finite element analysis. It was also shown that the microcavities serve to keep the microbeads in an organized fashion and yield consistent measurements.

Biological cells of different types were successfully analyzed with the proposed system. Analysis of certain different cell lines revealed pronounced differences. However, it was not possible to safely distinguish between SKBR3

and MCF7 as the elastic moduli of these cell lines were not distinguishable at 2.425 ±0.011 GPa and 2.413 ±0.028 GPa, respectively, according to student's t-tests. On the other hand, MDA-MB-231 shows a pronounced difference to all other cells lines with an estimated stiffness of 2.516 ±0.054 GPa. MCF7 and SKBR3 are similar, normally non-metastatic cells of the same origin whereas MDA-MB-231 cell line is known to be metastatic and thus different from the former lines [121, 122]. The mesenchymal phenotype observable in MDA-MB-231 makes it closer to JJ012 cells in comparison. In the results, these two cells are placed separately from MCF7 and SKBR3. JJ012 cells are actually placed between all other lines in terms of stiffness at 2.449 ±0.038 GPa; however, the results from this cell line are not statistically distinguishable from SKBR3 cell line despite the differences of these cell lines. This lack of distinguishability despite their different origins and the contrast of the results from MDA-MB-231 cells compared to the rest suggest that high frequency stiffness modulus of the cells is a possible biomarker for aggressiveness or metastatic potential as opposed to cell origin.

In comparison to popular mechanical characterization methods, the obtained elasticity values are about six orders of magnitude larger than the results obtained from AFM studies; however, this was expected due to the high frequency nature of the measurements. On the other hand, stiffness differential between the cells are in the order of megapascals, meaning that distinguishing between certain cell populations is possible. Unfortunately, comparison to other studies is difficult as there are few studies that analyze the given cell lines at

similar frequencies. However, acoustic microscopy studies done by Strohm, et al. report the MCF7 cell stiffness as 2.47 ±0.03 GPa which is close to the presented findings of 2.413 ±0.028 GPa. Considering different media and methods used for these studies, such discrepancies should be expected. Comparisons to other sensing methods are given in Table 6.1. In terms of application and practicality, the proposed platform is open to be improved through the use of microfluidics. The result is expected to be much greater throughput compared to AFM, magnetic bead twisting, and micropipette aspiration. AFM and bead twisting are inherently not suitable for microfluidic integration. Micropipette aspiration might be possible to integrate with microchannels in some form; however, the great deal of stress exerted on the cells makes it a less-than-ideal choice.

Table 6.1. Comparison to other biophysical studies in the literature.

	This Study	Strohm, et al. [66]	Weiss, et al. [65]	Cross, et al. [59]
Method	**Microcavity coupled SAW sensor**	Acoustic Microscopy	Acoustic Microscopy	Atomic Force Microscopy
Measurement Frequency	**200 MHz**	375 MHz	860 MHz	Static (0 Hz)
Cell Type	**MCF7**	MCF7	HeLa	Breast Ductal Adenocarcinoma
Cell Origin	**Epithelial**	Epithelial	Epithelial	Epithelial
Mean Elasticity	**2.413 ±0.028 GPa**	2.47 ±0.03 GPa	2.59 ±0.12 GPa	0.50 ±0.08 kPa

Ultimately, the novel SAW device with the embedded microcavity outlined in this study is a low cost microsystem capable of analyzing biological cell samples at high frequencies similar to acoustic microscopy techniques but in a miniaturized form. Furthermore, it can analyze sample volumes as small as approximately 1 pL which is orders of magnitude smaller than any other study in the literature, and it is capable of analyzing single cells with sizes similar to those of the microcavities. SAW devices have been used analyzing for proteins and other biomarkers in the past but this study is the first demonstration of single cell analysis with high frequency acoustic wave approach using a miniature sensor.

There are various ways to improve the performance of the system. First of all, better lithography processes can be used to form split electrodes instead of regular electrodes to prevent triple transit interference on the output signals. In order to make the matching easier, focused IDT electrodes can be used. This approach would result in improved insertion loss figures and make the input impedance manageable for discrete surface mount components. Proper electrical excitation with curved electrodes required for focused SAW operation necessitates a substrate with high tolerance for beam steering such as Y-Z lithium niobate. However, etching of lithium niobate is very difficult for beneficial microcavity depths as mentioned in Chapter 4. Therefore surface microcavities formed with a biocompatible material such as SU-8 can be utilized.

Throughput can be readily improved by microfluidic integration. It has been demonstrated through initial glycerin measurement results presented in this study that through specific designs, the microchannels can be readily integrated

with SAW sensors in seamless fashion and experiments can be run. It should be noted that such an integration strategy is also going to necessitate an efficient way of immobilizing cells for the duration of analysis as well as a robust way of detecting cells. Cells can be immobilized with an electromagnetic or hydrodynamic capturing scheme. On the other hand, an SH-wave based detection approach is necessary to avoid degrading the acoustic signal throughout the microfluidic channel, avoid the multiple reflections of the ultrasonic waves inside the large volume of the microchannel, and therefore obtain a better sensing scheme. SH-waves can be excited directly on 90° rotated ST-X samples, on essentially the same substrates as ST-X samples, in the orthogonal direction.

Stable temperatures around 37 °C help put less stress on the cells and prolong their viability. Uniform hotplates or embedded micro heaters can be integrated into the SAW device architecture to set the cell environment to body temperature. This might prove useful especially for possible subsequent tests on the morphology of the cells. Integration of this study with acoustic manipulation techniques [123] is also possible for continued development of the platform and increased functionality.

REFERENCES

1. Erickson, D., et al., *Nanobiosensors: Optofluidic, Electrical and Mechanical Approaches to Biomolecular Detection at the Nanoscale.* Microfluidics and Nanofluidics, 2008. 4(1-2): p. 33-52.

2. Lieber, C.M., F. Patolsky, and G.F. Zheng, *Nanowire-Based Biosensors.* Analytical Chemistry, 2006. 78(13): p. 4260-4269.

3. Liu, J., et al., *Real-Time Protein Detection Using Zno Nanowire/Thin Film Bio-Sensor Integrated with Microfluidic System.* 58th Electronic Components & Technology Conference, Proceedings, 2008: p. 1317-1322.

4. Boisen, A., et al., *Cantilever-Like Micromechanical Sensors.* Reports on Progress in Physics, 2011. 74(3): p. 1-30.

5. Waggoner, P.S. and H.G. Craighead, *Micro- and Nanomechanical Sensors for Environmental, Chemical, and Biological Detection.* Lab on a Chip, 2007. 7(10): p. 1238-1255.

6. Xu, S., *Electromechanical Biosensors for Pathogen Detection.* Microchim Acta, 2012. 178(3-4): p. 245-260.

7. Braun, T., et al., *Micromechanical Mass Sensors for Biomolecular Detection in a Physiological Environment.* Physical Review E, 2005. 72(3).

8. Bellan, L.M., D. Wu, and R.S. Langer, *Current Trends in Nanobiosensor Technology.* Wiley Interdisciplinary Reviews-Nanomedicine and Nanobiotechnology, 2011. 3(3): p. 229-246.

9. Fan, X.D., et al., *Sensitive Optical Biosensors for Unlabeled Targets: A Review.* Analytica Chimica Acta, 2008. 620(1-2): p. 8-26.

10. Boozer, C., et al., *Looking Towards Label-Free Biomolecular Interaction Analysis in a High-Throughput Format: A Review of New Surface Plasmon Resonance Technologies.* Current Opinion in Biotechnology, 2006. 17(4): p. 400-405.

11. Roh, S., T. Chung, and B. Lee, *Overview of the Characteristics of Micro- and Nano-Structured Surface Plasmon Resonance Sensors.* Sensors, 2011. 11(2): p. 1565-1588.

12. Clark, L. and C. Lyons, *Electrode Systems for Continuous Monitoring in Cardiovascular Surgery.* Annals New York Academy of Sciences, 1962. 102(102): p. 29-45.

13. Bergveld, P., *Development of an Ion-Sensitive Solid-State Device for Neurophysiological Measurements.* IEEE Transactions on Biomedical Engineering, 1970. BME-17(1): p. 70-71.

14. Liedberg, B., C. Nylander, and I. Lundstrom, *Surface-Plasmon Resonance for Gas-Detection and Biosensing.* Sensors and Actuators, 1983. 4(2): p. 299-304.

15. Kundu, T., *Ultrasonic Nondestructive Evaluation: Engineering and Biological Material Characterization*. Boca Raton, FL: CRC Press, 2004.

16. Morgan, D., *Surface Acoustic Wave Filters: With Applications to Electronic Communications and Signal Processing*. Academic Press, 2007.

17. White, R.M. and F.W. Voltmer, *Direct Piezoelectric Coupling to Surface Elastic Waves.* Applied Physics Letters, 1965. 7(12): p. 314-316.

18. Campbell, C., *Surface Acoustic Wave Devices for Mobile and Wireless Communications*. San Diego; Toronto: Academic Press, 1998.

19. Tigli, O., et al., *Fabrication and Characterization of a Surface-Acoustic-Wave Biosensor in Cmos Technology for Cancer Biomarker Detection.* Biomedical Circuits and Systems, IEEE Transactions on, 2010. 4(1): p. 62-73.

20. Kalantar-Zadeh, K., et al., *Comparison of Layered Based Saw Sensors.* Sensors and Actuators B-Chemical, 2003. 91(1-3): p. 303-308.

21. Ferrari, V. and R. Lucklum, *Overview of Acoustic-Wave Microsensors* in *Piezoelectric Transducers and Applications.* 2008, p. 39-62.

22. Tigli, O. and M.E. Zaghloul, *Surface Acoustic Wave (Saw) Biosensors.* 53rd IEEE International Midwest Symposium on Circuits and Systems, 2010: p. 77-80.

23. Ding, X., et al., *Surface Acoustic Wave Microfluidics.* Lab on a Chip, 2013. 13(18): p. 3626-3649.

24. Renaudin, A., et al., *Integrated Active Mixing and Biosensing Using Surface Acoustic Waves (Saw) and Surface Plasmon Resonance (Spr) on a Common Substrate.* Lab on a Chip, 2010. 10(1): p. 111-115.

25. Piazza, G., et al., *Piezoelectric Aluminum Nitride Thin Films for Microelectromechanical Systems.* MRS Bulletin, 2012. 37(11): p. 1051-1061.

26.   Fu, Y.Q., et al., *Recent Developments on Zno Films for Acoustic Wave Based Bio-Sensing and Microfluidic Applications: A Review.* Sensors and Actuators B: Chemical, 2010. 143(2): p. 606-619.

27.   Lange, K., B.E. Rapp, and M. Rapp, *Surface Acoustic Wave Biosensors: A Review.* Analytical and Bioanalytical Chemistry, 2008. 391(5): p. 1509-1519.

28.   Wixforth, A., et al., *Acoustic Manipulation of Small Droplets.* Analytical and Bioanalytical Chemistry, 2004. 379(7): p. 982-991.

29.   Gammoudi, I., et al., *Love-Wave Bacteria-Based Sensor for the Detection of Heavy Metal Toxicity in Liquid Medium.* Biosensors and Bioelectronics, 2010. 26(4): p. 1723-1726.

30.   Lindner, G., *Sensors and Actuators Based on Surface Acoustic Waves Propagating Along Solid–Liquid Interfaces.* Journal of Physics D: Applied Physics, 2008. 41(12): p. 123002.

31.   Raimbault, V., D. Rebière, and C. Dejous, *A Microfluidic Surface Acoustic Wave Sensor Platform: Application to High Viscosity Measurements.* Materials Science and Engineering: C, 2008. 28(5): p. 759-764.

32.   Lee, R., et al. *Prototype Microwave Acoustic Fluid Sensors* in *Ultrasonics Symposium*, 1988: IEEE.

33.   Wang, Z. and J. Zhe, *Recent Advances in Particle and Droplet Manipulation for Lab-on-a-Chip Devices Based on Surface Acoustic Waves.* Lab on a Chip, 2011. 11(7): p. 1280-1285.

34.   Lindstrom, S. and H. Andersson-Svahn, *Single-Cell Analysis: Methods and Protocols*. Humana Press, 2012.

35.   Lindstrom, S. and H. Andersson-Svahn, *Miniaturization of Biological Assays - Overview on Microwell Devices for Single-Cell Analyses.* Biochimica Et Biophysica Acta-General Subjects, 2011. 1810(3): p. 308-316.

36.   Spudich, J.L. and D.E. Koshland, *Non-Genetic Individuality - Chance in Single Cell.* Nature, 1976. 262(5568): p. 467-471.

37.   Sweedler, J.V. and E.A. Arriaga, *Single Cell Analysis.* Analytical and Bioanalytical Chemistry, 2007. 387(1): p. 1-2.

38.   Stingl, J. and C. Caldas, *Molecular Heterogeneity of Breast Carcinomas and the Cancer Stem Cell Hypothesis.* Nature Reviews Cancer, 2007. 7(10): p. 791-799.

39.   Al-Hajj, M., et al., *Prospective Identification of Tumorigenic Breast Cancer Cells.* Proceedings of the National Academy of Sciences, 2003. 100(7): p. 3983-3988.

40.   Powell, A.A., et al., *Single Cell Profiling of Circulating Tumor Cells: Transcriptional Heterogeneity and Diversity from Breast Cancer Cell Lines.* Plos One, 2012. 7(5): p. e33788.

41.   Pece, S., et al., *Biological and Molecular Heterogeneity of Breast Cancers Correlates with Their Cancer Stem Cell Content.* Cell, 2010. 140(1): p. 62-73.

42.   Campbell, L.L. and K. Polyak, *Breast Tumor Heterogeneity: Cancer Stem Cells or Clonal Evolution?* Cell cycle, 2007. 6(19): p. 2332-2338.

43.   Templer, R.H. and O. Ces, *New Frontiers in Single-Cell Analysis.* Journal of the Royal Society Interface, 2008. 5: p. S111-S112.

44.   Makale, M., *Cellular Mechanobiology and Cancer Metastasis.* Birth Defects Research Part C: Embryo Today: Reviews, 2007. 81(4): p. 329-343.

45.   Lim, C.T., *Single Cell Mechanics Study of the Human Disease Malaria.* Journal of Biomechanical Science and Engineering, 2006. 1(1): p. 82-92.

46.   Suresh, S., et al., *Connections between Single-Cell Biomechanics and Human Disease States: Gastrointestinal Cancer and Malaria.* Acta Biomaterialia, 2005. 1(1): p. 15-30.

47.   *http://www.who.int/mediacentre/factsheets/fs297/en/.* Last accessed on: 8-15-14.

48.   Lee, G.Y.H. and C.T. Lim, *Biomechanics Approaches to Studying Human Diseases.* Trends in Biotechnology, 2007. 25(3): p. 111-118.

49.   *http://www.cancer.gov/cancertopics/cancerlibrary/what-is-cancer.* Last accessed on: 8-15-14.

50.   Ingber, D.E., *Mechanobiology and Diseases of Mechanotransduction.* Annals of Medicine, 2003. 35(8): p. 564-577.

51.   Rodriguez, M.L., P.J. McGarry, and N.J. Sniadecki, *Review on Cell Mechanics: Experimental and Modeling Approaches.* Applied Mechanics Reviews, 2013. 65(6).

52.   Darling, E.M., et al., *A Thin-Layer Model for Viscoelastic, Stress-Relaxation Testing of Cells Using Atomic Force Microscopy: Do Cell*

Properties Reflect Metastatic Potential? Biophysical Journal, 2007. 92(5): p. 1784-1791.

53. Ward, K., et al., *Viscoelastic Properties of Transformed Cells: Role in Tumor Cell Progression and Metastasis Formation.* Biorheology, 1990. 28(3-4): p. 301-313.

54. Lim, C., et al., *Experimental Techniques for Single Cell and Single Molecule Biomechanics.* Materials Science and Engineering: C, 2006. 26(8): p. 1278-1288.

55. Mijailovich, S.M., et al., *A Finite Element Model of Cell Deformation During Magnetic Bead Twisting.* Journal of Applied Physiology, 2002. 93(4): p. 1429-1436.

56. Ohayon, J., et al., *Analysis of Nonlinear Responses of Adherent Epithelial Cells Probed by Magnetic Bead Twisting: A Finite Element Model Based on a Homogenization Approach.* Journal of biomechanical engineering, 2004. 126(6): p. 685-698.

57. Li, Q.S., et al., *Afm Indentation Study of Breast Cancer Cells.* Biochemical and Biophysical Research Communications, 2008. 374(4): p. 609-613.

58. Lekka, M., et al., *Elasticity of Normal and Cancerous Human Bladder Cells Studied by Scanning Force Microscopy.* European Biophysics Journal with Biophysics Letters, 1999. 28(4): p. 312-316.

59. Cross, S.E., et al., *Nanomechanical Analysis of Cells from Cancer Patients.* Nature Nanotechnology, 2007. 2(12): p. 780-783.

60. Plodinec, M., et al., *The Nanomechanical Signature of Breast Cancer.* Nature Nanotechnology, 2012. 7(11): p. 757-765.

61. Cross, S.E., et al., *Afm-Based Analysis of Human Metastatic Cancer Cells.* Nanotechnology, 2008. 19(38).

62. Calderon, C., et al., *Differences in the Attenuation of Ultrasound by Normal, Benign, and Malignant Breast Tissue.* Journal of Clinical Ultrasound, 1976. 4(4): p. 249-254.

63. d'Astous, F. and F. Foster, *Frequency Dependence of Ultrasound Attenuation and Backscatter in Breast Tissue.* Ultrasound in Medicine & Biology, 1986. 12(10): p. 795-808.

64. Zhao, X., et al., *Multi-Layer Phase Analysis: Quantifying the Elastic Properties of Soft Tissues and Live Cells with Ultra-High-Frequency Scanning Acoustic Microscopy.* Ultrasonics, Ferroelectrics, and Frequency Control, IEEE Transactions on, 2012. 59(4): p. 610-620.

65. Weiss, E.C., et al., *Mechanical Properties of Single Cells by High-Frequency Time-Resolved Acoustic Microscopy.* IEEE T Ultrason Ferr, 2007. 54(11): p. 2257-2271.

66. Strohm, E.M., G.J. Czarnota, and M.C. Kolios, *Quantitative Measurements of Apoptotic Cell Properties Using Acoustic Microscopy.* Ultrasonics, Ferroelectrics and Frequency Control, IEEE Transactions on, 2010. 57(10): p. 2293-2304.

67. Hou, H.W., et al., *Deformability Study of Breast Cancer Cells Using Microfluidics.* Biomedical Microdevices, 2009. 11(3): p. 557-564.

68. Hur, S.C., et al., *Deformability-Based Cell Classification and Enrichment Using Inertial Microfluidics.* Lab on a Chip, 2011. 11(5): p. 912-920.

69. Gossett, D.R., et al., *Hydrodynamic Stretching of Single Cells for Large Population Mechanical Phenotyping.* Proceedings of the National Academy of Sciences of the United States of America, 2012. 109(20): p. 7630-7635.

70. Cular, S., S.K.R.S. Sankaranarayanan, and V.R. Bhethanabotla, *Enhancing Effects of Microcavities on Shear-Horizontal Surface Acoustic Wave Sensors: A Finite Element Simulation Study.* Applied Physics Letters, 2008. 92(24): p. 244104-244104-3.

71. Hashimoto, K.Y., *Surface Acoustic Wave Devices in Telecommunications: Modelling and Simulation*. Springer, 2000.

72. Landau, L.D. and E.M. Lifshitz, *Fluid Mechanics*. London, UK: Pergamon Press, 1966.

73. Lautrup, B., *Physics of Continuous Matter*. Bristol ; Philadelphia, PA: Institute of Physics Pub., 2005.

74. Litovitz, T.A. and C.M. Davis, *Physical Acoustics*. NY, USA: Academic Press, 1964.

75. *Comsol Multiphysics Reference Manual*, 2013, Comsol Inc.: Boston, MA. p. 1270.

76. Auld, B.A., *Acoustic Fields and Waves in Solids*. Malabar, FL: Robert E. Krieger Publishing Company, 1990.

77. Mechkour, H. *The Exact Expressions for the Roots of Rayleigh Wave Equation* in *Proceedings of The 2-nd International Colloquium of Mathematics in Engineering and Numerical Physics, Bucharest, Romania*, 2003.

78. Cox, B., *Acoustics for Ultrasound Imaging*, 2012, Univeristy College London, UK. p. 79.

79. Du, J., et al., *A Study of Love-Wave Acoustic Sensors.* Sensors and Actuators A: Physical, 1996. 56(3): p. 211-219.

80. Botkin, N. and V. Turova, *Mathematical Models of a Biosensor.* Applied Mathematical Modelling, 2004. 28(6): p. 573-589.

81. Prabhakara, S. and M. Deshpande, *The No-Slip Boundary Condition in Fluid Mechanics.* Resonance, 2004. 9(5): p. 61-71.

82. Christensen, R.M., *Theory of Viscoelasticity.* London, UK: Dover Publications, 2010.

83. Raimbault, V., D. Rebiere, and C. Dejous, *A Microfluidic Surface Acoustic Wave Sensor Platform: Application to High Viscosity Measurements.* Materials Science & Engineering C-Biomimetic and Supramolecular Systems, 2008. 28(5-6): p. 759-764.

84. Ferry, J.D., *Viscoelastic Properties of Polymers*. John Wiley & Sons, 1980.

85. Cheng, N.S., *Formula for the Viscosity of a Glycerol-Water Mixture.* Industrial & Engineering Chemistry Research, 2008. 47(9): p. 3285-3288.

86. Elvira-Segura, L., *Ultrasonic Velocity Measurement in Liquids at Low Frequencies (< 50 Khz) for Milliliter Samples.* IEEE Transactions on Ultrasonics Ferroelectrics and Frequency Control, 2001. 48(2): p. 632-637.

87. Slie, W.M., A.R. Donfor, and T.A. Litovitz, *Ultrasonic Shear and Longitudinal Measurements in Aqueous Glycerol.* Journal of Chemical Physics, 1966. 44(10): p. 3712-&.

88. Piccirelli, R. and T.A. Litovitz, *Ultrasonic Shear and Compressional Relaxation in Liquid Glycerol.* Journal of the Acoustical Society of America, 1957. 29(9): p. 1008-1020.

89. Martin, S., et al., *Characterization of Sh Acoustic Plate Mode Liquid Sensors.* Sensors and Actuators, 1989. 20(3): p. 253-268.

90. Ricco, A.J. and S.J. Martin, *Acoustic-Wave Viscosity Sensor.* Applied Physics Letters, 1987. 50(21): p. 1474-1476.

91. Martin, B.A., S.W. Wenzel, and R.M. White, *Viscosity and Density Sensing with Ultrasonic Plate Waves.* Sensors and Actuators A: Physical, 1989. 22(1): p. 704-708.

92. Nomura, T., A. Saitoh, and Y. Horikoshi, *Measurement of Acoustic Properties of Liquid Using Liquid Flow Sh-Saw Sensor System.* Sensors and Actuators B-Chemical, 2001. 76(1-3): p. 69-73.

93. Teston, F., et al., *Analysis of the Coupling between Shear Horizontal Plate Waves and Liquids: Application to the Measurement of the Shear Rigidity Modulus of Glycerol Solutions.* Journal of Applied Physics, 2000. 87(2): p. 689-694.

94. Link, M., et al., *Sensing Characteristics of High-Frequency Shear Mode Resonators in Glycerol Solutions.* Sensors and Actuators B: Chemical, 2007. 121(2): p. 372-378.

95. Wilkie-Chancellier, N., et al., *Lamb Wave Sensor for Viscous Fluids Characterization.* Sensors Journal, IEEE, 2009. 9(9): p. 1142-1147.

96. McHale, G., et al., *Surface Acoustic Wave Resonances in the Spreading of Viscous Fluids.* Physical Review B, 1999. 59(12): p. 8262-8270.

97. McHale, G., et al., *Acoustic Wave-Liquid Interactions.* Materials Science & Engineering C-Biomimetic and Supramolecular Systems, 2000. 12(1-2): p. 17-22.

98. McHale, G., et al., *Interaction of Surface Acoustic Waves with Viscous Liquids.* Faraday Discussions, 1997. 107: p. 15-26.

99. Newton, M.I., et al., *Surface Acoustic Wave-Liquid Drop Interactions.* Sensors and Actuators a-Physical, 1999. 76(1-3): p. 89-92.

100. Lim, C.T., E.H. Zhou, and S.T. Quek, *Mechanical Models for Living Cells - a Review.* Journal of Biomechanics, 2006. 39(2): p. 195-216.

101. Hochmuth, R.M., *Micropipette Aspiration of Living Cells.* Journal of Biomechanics, 2000. 33(1): p. 15-22.

102. Lindstrom, S. and H. Andersson-Svahn, *Overview of Single-Cell Analyses: Microdevices and Applications.* Lab on a Chip, 2010. 10(24): p. 3363-3372.

103. Drury, J.L. and M. Dembo, *Aspiration of Human Neutrophils: Effects of Shear Thinning and Cortical Dissipation.* Biophysical Journal, 2001. 81(6): p. 3166-3177.

104. Melzak, K.A., et al., *Why Size and Speed Matter: Frequency Dependence and the Mechanical Properties of Biomolecules.* Soft Matter, 2011. 7(2): p. 332-342.

105. Stamenovic, D., et al., *Rheological Behavior of Living Cells Is Timescale-Dependent.* Biophysical Journal, 2007. 93(8): p. L39-L41.

106. Strohm, E.M. and M.C. Kolios. *Measuring the Mechanical Properties of Cells Using Acoustic Microscopy* in *Engineering in Medicine and Biology Society, 2009. EMBC 2009. Annual International Conference of the IEEE*, 2009: IEEE.

107. Rosenblatt, N., et al., *Dynamics of Prestressed Semiflexible Polymer Chains as a Model of Cell Rheology.* Physical Review Letters, 2006. 97(16): p. 168101.

108. Schmidt, F.G., F. Ziemann, and E. Sackmann, *Shear Field Mapping in Actin Networks by Using Magnetic Tweezers.* European Biophysics Journal with Biophysics Letters, 1996. 24(5): p. 348-353.

109. Strohm, E.M., G.J. Czarnota, and M.C. Kolios, *Quantitative Measurements of Apoptotic Cell Properties Using Acoustic Microscopy.* IEEE Transactions on Ultrasonics Ferroelectrics and Frequency Control, 2010. 57(10): p. 2293-2304.

110. Ballato, A., *Piezoelectric Saw Device with a Corrugated Surface.* U.S. Patent No. 4,634,914., 1987.

111. Association, G.P., *Physical Properties of Glycerin and Its Solutions*. New York, 1963.

112. Haapalainen, M. and A. Makynen. *Measuring Electrical Properties of Microbeads by Dielectrophoretic Mobility* in *Instrumentation and Measurement Technology Conference (I2MTC), 2011 IEEE*, 2011: IEEE.

113. Ricco, A., S. Martin, and T. Zipperian, *Surface Acoustic Wave Gas Sensor Based on Film Conductivity Changes.* Sensors and Actuators, 1985. 8(4): p. 319-333.

114. Randles, A.B., M. Esashi, and S. Tanaka, *Etch Rate Dependence on Crystal Orientation of Lithium Niobate.* IEEE Transactions on Ultrasonics Ferroelectrics and Frequency Control, 2010. 57(11): p. 2372-2380.

115. Winnall, S. and S. Winderbaum, *Lithium Niobate Reactive Ion Etching*, 2000, DTIC Document.

116. Benchabane, S., et al., *Highly Selective Electroplated Nickel Mask for Lithium Niobate Dry Etching.* Journal of Applied Physics, 2009. 105(9).

117. Gajasinghe, R., et al., *Experimental Study of Pdms Bonding to Various Substrates for Monolithic Microfluidic Applications.* Journal of Micromechanics and Microengineering, 2014. 24(7): p. 075010.

118. Nordström, M., et al., *Rendering Su-8 Hydrophilic to Facilitate Use in Micro Channel Fabrication.* Journal of Micromechanics and Microengineering, 2004. 14(12): p. 1614.

119. Gregory, S., *Physical Properties of Glycerine*. Marcel Dekker: New York, 1991.

120. Yin, K.B., *The Mesenchymal-Like Phenotype of the Mda-Mb-231 Cell Line*. INTECH Open Access Publisher, 2011.

121. Holliday, D.L. and V. Speirs, *Choosing the Right Cell Line for Breast Cancer Research.* Breast Cancer Res, 2011. 13(4): p. 215.

122. Goodison, S., et al., *The Interrelationship between Drim Gene Expression and Cytogenetic and Phenotypic Characteristics in Human Breast Tumor Cell Lines.* BMC genomics, 2003. 4(1): p. 39.

123. Sesen, M., T. Alan, and A. Neild, *Microfluidic Plug Steering Using Surface Acoustic Waves.* Lab on a Chip, 2015. 15(14): p. 3030-3038.